SANDIA REPORT

SAND96–2215 • UC–706
Unlimited Release
Printed August 1996

Coherent Change Detection and Interferometric ISAR Measurements in The Folded Compact Range

Kurt W. Sorensen

Prepared by
Sandia National Laboratories
Albuquerque, New Mexico 87185 and Livermore, California 94550
for the United States Department of Energy
under Contract DE-AC04-94AL85000

Issued by Sandia National Laboratories, operated for the United States Department of Energy by Sandia Corporation.

Available to DOE and DOE contractors from
Office of Scientific and Technical Information
PO Box 62
Oak Ridge, TN 37831

Prices available from (615) 576-8401, FTS 626-8401

Available to the public from
National Technical Information Service
US Department of Commerce
5285 Port Royal Rd
Springfield, VA 22161

NTIS price codes
Printed copy: A05
Microfiche copy: A01

SAND96-2215
Unlimited Release
Printed August 1996

Distribution
Category UC-706

COHERENT CHANGE DETECTION AND INTERFEROMETRIC ISAR MEASUREMENTS IN THE FOLDED COMPACT RANGE

Kurt W. Sorensen
Radar/Antenna Department 2343
Sandia National Laboratories
Albuquerque, NM 87185-0533

Abstract

A folded compact range configuration has been developed at the Sandia National Laboratories' compact range antenna and radar-cross-section measurement facility as a means of performing indoor, environmentally-controlled, far-field simulations of synthetic aperture radar (SAR) measurements of distributed target samples (i.e., gravel, sand, etc.). The folded compact range configuration has previously been used to perform coherent-change-detection (CCD) measurements, which allow disturbances to distributed targets on the order of fractions of a wavelength to be detected. A previous report (SAND95-0389) described both the development of the folded compact range, as well as the initial set of coherent-change-detection measurements that were made with the system.

This report describes follow-on CCD measurements of other distributed target samples, and also investigates the sensitivity of the CCD measurement process to changes in the relative spatial location of the SAR sensor between observations of the target. Additionally, this report describes the theoretical and practical aspects of performing interferometric inverse-synthetic-aperture-radar (IFISAR) measurements in the folded compact range environment. In addition to the two-dimensional spatial resolution afforded by typical ISAR processing, IFISAR measurements provide resolution of the relative heights of targets with accuracies on the order of a wavelength. Several examples are given of digital height maps that have been generated from measurements performed at the folded compact range facility.

The CCD and IFISAR measurements have demonstrated not only the viability of the folded compact range concept in simulating SAR CCD and interferometric SAR (IFSAR) measurements, but also its usefulness as a tool in the research and development of SAR CCD and IFSAR image generation and measurement methodologies.

Acknowledgments

I would like to acknowledge Dave Zittel and John Littlejohn at the compact range measurement facility for their efforts and skill at implementing somewhat unusual measurement configurations, for timely data acquisitions, and in general for their enthusiastic support of this work, without all of which this project would not have been possible. I would also like to thank Doug Bickel for many useful discussions that greatly contributed to the successful implementation of the interferometric capability at the compact range, as well as to the processing of imagery. Finally, thanks also to Ben Johnson for his encouragement and support.

CONTENTS

Figures

Intentionally Left Blank

1. INTRODUCTION

A folded compact range configuration has been developed at the Sandia National Laboratories' compact range antenna and radar-cross-section measurement facility as a means of performing indoor, environmentally-controlled, far-field simulations of synthetic aperture radar (SAR) measurements of distributed target samples (i.e., gravel, sand, etc.). A photograph of the folded compact range measurement configuration is given in Appendix A (Figure A-1). In particular, the folded compact range configuration has been used to perform both highly sensitive coherent-change-detection (CCD) and interferometric inverse-synthetic-aperture-radar (IFISAR) measurements. The CCD measurements allow disturbances to distributed targets on the order of fractions of a wavelength to be detected, while the IFISAR measurements provide, in addition to the two-dimensional spatial resolution afforded by typical ISAR processing, resolution of the relative height of targets with accuracies on the order of a wavelength.

A previous report [1] has described the development of the folded compact range configuration, as well as the initial set of coherent-change-detection measurements that were made with the system. This report describes follow-on CCD measurements of other distributed target samples, and also investigates the sensitivity of the CCD measurement process to changes in the relative spatial location of the SAR sensor between observations of the target. Additionally, this report describes the theoretical and practical aspects of performing interferometric measurements in the folded compact range environment. Several examples are given of digital height maps that have been generated from measurements performed at the folded compact range facility.

The CCD and IFISAR measurements have been quite successful, and have demonstrated not only the viability of the folded compact range concept in simulating SAR CCD and interferometric SAR (IFSAR) measurements, but also its usefulness as a tool in the research and development of SAR CCD and IFSAR image generation and measurement methodologies.

2. COHERENT CHANGE DETECTION MEASUREMENTS

As described in [1], the formation of a coherent change detection (CCD) image first requires that a pair of two-dimensional, complex images be generated, following which the images are compared or correlated in some fashion to form the final CCD image. In the SNL folded compact range, complex images of the distributed target samples are created by performing wideband stepped-frequency measurements while rotating the target over an appropriate angular sector. The measured raw data is then calibrated, following which conventional signal processing is used to form focused, two-dimensional inverse synthetic aperture radar (ISAR) images of the backscattered return from the distributed target. This results in data which is equivalent to that which can be acquired with a circular spotlight-mode SAR [2]. The pair of images typically result from measuring first an "undisturbed" target sample, followed by a measurement of the same target sample, but which has been perturbed in some

manner. The objective of the comparison is thus to determine how the target has changed with time, or in other words, how it has temporally decorrelated.

Section 2.1 addresses the general issue of image decorrelation and illustrates the ability of the folded compact range measurement system to isolate particular decorrelation sources for independent investigation.

Section 2.2 addresses the issue of distributed target decorrelation given a fixed geometry; that is, the spatial location of the target relative to the radar sensor is held constant between target measurements, such that by far the most significant source of decorrelation appearing in the processed CCD images is due to the purposeful disturbing of the target sample. This allows the contributors to temporal decorrelation to be independently studied, and provides a means to compare the measured results with those presented in the previous report [1].

Section 2.3 then addresses the issue of sensitivity of the coherent change detection process to changes in the geometry of the measurement due to angular offset errors between observations of the target. In this section, spatial decorrelation is simulated by introducing varying degrees of angular offset into the elevation and azimuth axes of the positioner controller while keeping the distributed target sample itself undisturbed. During the course of this discussion, image decorrelation due to pixel misregistration is also treated, and is shown to be an integral factor in defining the overall correlation level of a pair of complex images.

2.1 Image Decorrelation

Fundamentally, decorrelation which occurs between a pair of two-dimensional radar cross section images is a consequence of any differences that may exist in the amplitude and phase values between the images. Thus, in the case of an airborne or spaceborne SAR platform collecting image data, decorrelation can arise not only from physical changes in the target area during the period of time between observations, but also from noise, calibration errors, variations in the viewing geometry due to alteration of the spatial location of the SAR platform between observations, etc. [3]. In more definitive terms, it has been shown [3], [4] that the total correlation (γ_{total}) between a pair of images is the product of the various correlation components, such that a reasonable expression for γ_{total} that includes the major decorrelation sources of interest (for the purposes of this study) can be written as

$$\gamma_{total} = \gamma_{thermal} \cdot \gamma_{temporal} \cdot \gamma_{spatial} \cdot \gamma_{registration} \,, \tag{1}$$

where

$\gamma_{thermal}$ = correlation due to thermal noise,

$\gamma_{temporal}$ = correlation due to movement of the target,

$\gamma_{spatial}$ = correlation due to imaging geometry, and

$\gamma_{registration}$ = correlation due to pixel misregistration.

The major advantage of using a compact range facility to perform coherent change detection measurements is the ability to control to a much larger extent the physical phenomena which influence decorrelation of a pair of complex SAR images, thus allowing the various decorrelation sources to be isolated and independently investigated. For example, the compact range measurement facility employs a precision motorized turntable and positioner controller to regulate the motion of the target in a tightly controlled and highly repeatable fashion, thus minimizing unintended spatial decorrelation effects. Further, the compact range is housed in a stable, environmentally-controlled anechoic chamber to reduce the effects of thermal noise and minimize unintentional disturbance of the target sample between measurements, such that the effects of various temporal decorrelation sources can be independently assessed.

The ability to isolate and independently study decorrelation sources is illustrated by considering $\gamma_{thermal}$. A simple equation describing the relationship of $\gamma_{thermal}$ to the overall signal-to-noise ratio of a measurement can be written as [4]

$$\gamma_{thermal} = \frac{1}{1 + SNR^{-1}} \tag{2}$$

(where SNR = signal-to-noise ratio), and provides a means of obtaining the equivalent signal-to-noise ratio of the folded compact range measurement system for any given target sample. That is, by sequentially forming two images of a target sample without perturbing the sample or altering the sensor geometry between the two measurements, as well as processing the images in precisely the same manner, the $\gamma_{temporal}$, $\gamma_{spatial}$, and $\gamma_{registration}$ correlation factors will all have a value of very nearly unity, such that $\gamma_{total} \cong \gamma_{thermal}$, and the measured correlation factor thus provides a measurement of the SNR for the measurement system. (It is assumed in this equation that the SNR for the pair of images is the same.)

Such an experiment has been carried out for small "pea" gravel, large crushed gravel, and fine-grained sand target samples, with the results being displayed in Table 1. The measured $\gamma_{thermal}$ correlation values shown in Table 1 are actually the average of the correlation values calculated at each image pixel for the 1.5' x 1.5' center region of the sample holder. Also shown in the table are the SNR values calculated for the samples using the measured $\gamma_{thermal}$ values and equation (2).

TABLE 1. Measured Signal-to-Noise Ratio of the Folded Compact Range Measurement System For Three Target Samples

Target Sample	$\gamma_{thermal}$	Calculated SNR
Small Gravel	0.9999	80.00 dB
Large Gravel	0.9997	70.45 dB
Masonry Sand	0.9900	39.91 dB

It can be determined from this exercise that the effective signal-to-noise ratios of the measurements in the folded compact range are very high, such that decorrelation in the measurements resulting from thermal noise is essentially negligible.

2.2 Temporal Decorrelation Experiments

Having verified the ability to minimize the contributions of thermal noise to image decorrelation in the compact range, it is then possible to study the effects of other contributors to decorrelation. The objective of this set of experiments is to investigate the effects of potential sources of temporal decorrelation ($\gamma_{temporal}$) on distributed target samples. The ultimate goal is that such experimentation will eventually result in the ability to associate remotely measured correlation values of various targets with particular geophysical or man-made disturbances to the target area. As described above, these experiments were carried out by measuring first an "undisturbed" target sample, followed by measurement of the same target sample, but which had been perturbed in some manner. The imaging geometry for the two measurements was kept constant. Decorrelation detection of the resulting complex image pair was performed using the maximum likelihood estimate of correlation, given by [3]

$$\gamma = \frac{\left| \sum_i \sum_j g_{ij}^* h_{ij} \right|}{\sqrt{\left| \sum_i \sum_j |g_{ij}|^2 \cdot \sum_i \sum_j |h_{ij}|^2 \right|}}, \tag{3}$$

where

g_{ij} = the first registered complex image for the i^{th} range index and the j^{th} azimuth index, and

h_{ij} = the second registered complex image for the i^{th} range index and the j^{th} azimuth index.

The summations are over the number of "looks" or pixel samples that are spatially averaged in range and azimuth, and are used to reduce the statistical variation in the final image [4]. A more explicit explanation of this algorithm is given in [5], [6].

The temporal decorrelation measurements reported here are actually a continuation of the coherent change detection (CCD) measurements described in the previous report [1], in which CCD images resulting from measurements of "pea gravel" (gravel composed of stones having diameters ranging from approximately 1/4 - 3/8 inches) were summarized. The CCD imagery presented in this report is of large crushed gravel (stones having dimensions of roughly 1.25" x 2") and "masonry" (fine-grained) sand. Photographs of the comparative size of pea gravel and crushed gravel (Figure A-2), and of the sample holder containing masonry sand (Figure B-1), are respectively shown in Appendices A and B.

In the course of performing the previous set of CCD measurements on pea gravel, a test plan was created which allowed several aspects of temporal decorrelation associated with CCD image formation to be investigated [1]. In order to maintain consistency between the previous and current reports, as well as to facilitate ease of comparison between measurements of differing distributed target types, the same test plan (with some slight revisions) has been used here.

2.2.1 *Test Plan for CCD Measurements*

The test plan for the CCD measurements of the large crushed gravel and masonry sand is given below. From the standpoint of detecting disturbances to the surface of the material under test, it should be noted that there was little substantive difference between measurements made with either a vertically-polarized or horizontally-polarized incident field. The CCD imagery displayed in Appendices A and B was all generated with a horizontally-polarized incident field.

Test Plan

Null Set Experiment

Intent is to determine the level of nominal backscattering from the distributed target sample.

(1) Measure the distributed target sample and create a two-dimensional image of the target sample without performing any decorrelation detection processing. (Figures A-3, B-2)

Decorrelation Detectability Experiments

Intent is to determine levels of discernible disturbance to the material surface.

(2) Walk across target sample
   a) Walk across the distributed target sample in a distinct pattern and retrace steps one time (that is, walk over same path two times). (Figures A-4, B-3)
   b) Walk across target sample in distinct pattern, but do not retrace steps. Space steps far enough apart that they can be individually resolved in the image. (Figures A-5 and B-4)

(3) Rake across target sample (single pass of rake across diameter of sample holder).
   a) Light raking--barely disturb surface (not visibly apparent in crushed gravel, small rake tine indentations visible in sand). (Figures A-6, B-5)
   b) Medium raking--overturn majority of material in raking path, but leave no rake tine marks (not visibly apparent in crushed gravel, back side of rake used in sand). (Figures A-7, B-6)
   c) Heavy raking (sand only)--Fully embed rake tines in target sample; leave visible indentations in the surface of the sample. (Figure B-7)

(4) Discrete target sample displacement
   a) For crushed gravel, within approximately 8 inch diameter circles in the sample holder, individually pick up the following number of rocks **without** replacing them: (i) 2 rocks, (ii) 5 rocks, (iii) 10 rocks, and (iv) 20 rocks. (Figure A-8)
   b) For sand, within approximately 6 inch diameter circles in the sample holder, remove the following volume of sand **without** replacing it: (i) 1 tablespoon, (ii) 2 tablespoons, (iii) 4 tablespoons, and (iv) 8 tablespoons. (Figure B-8)

Moisture Effects Experiment

Intent is to examine the effect of moisture in decorrelation of CCD images.

(5) Moisture test
   a) Make a set of tire tracks in the target sample approximately 24 inches apart. (Figures A-9 [gravel set #1], A-14 [gravel set #2], B-9 [sand])
   b) After performing the measurement described in (a), evenly sprinkle 4 gallons of water across the entire sample holder, and immediately re-measure (without re-measuring test background). (Figures A-10 [gravel set #1], A-15 [gravel set #2], B-10 [sand])
   c) While allowing the water to "completely" evaporate (until the surface of the material becomes visually dry), re-measure the material at periodic intervals. (Figures A-11,12,13 [gravel set #1], A-16,17,18 [gravel set #1], B-11,12,13 [sand])

2.2.2 *Discussion of Experimental Results*

This purpose of this section is to briefly discuss the outcome of each set of experiments, as well as to highlight some of the more interesting results and findings.

Null Set Experiment

The intent of this experiment was to determine the level of nominal backscattering from the distributed target samples. Using the scattered field from the center section (approximately 2 ft. x 2 ft.) of the sample holder, the mean backscattered signal level of the crushed gravel was measured to be -37 dBsm. The backscattered signal from the sand was similarly measured, and as expected was significantly lower, having a mean level of about -54 dBsm. Also of interest was the fact that in both cases the background clutter level outside of the sample holder area was in general less than -70 dBsm.

The lower level of backscattering from the sand relative to that from the crushed gravel corresponds with its lower reflectivity, indicating that a larger percentage of the incident field is propagating into the sand and being attenuated. For the purposes of this and follow-on experiments, it is of interest to estimate the value of the skin depth for dry sand. Skin depth is defined as the distance a wave must travel in a lossy medium to be attenuated to 36.8% of its value at the surface [7]. The relative complex permittivity of dry sandy soil at 10 GHz is [8]

$$\varepsilon_r = \varepsilon_r' - j\varepsilon_r'' = 2.53 - j0.0092 . \tag{4}$$

From [7] the skin depth (δ) for a "good dielectric" ($\left(\frac{\sigma}{\omega\varepsilon'}\right)^2 << 1$, which is true for the complex permittivity parameter specified above) is given by

$$\delta \cong \frac{2}{\sigma}\sqrt{\frac{\varepsilon}{\mu}}, \tag{5}$$

where σ can be determined from the imaginary part of the permittivity as $\sigma = \omega\varepsilon_r''\varepsilon_0$. Using this expression and the permittivity value defined above, the skin depth for sand at a frequency of 12.0 GHz can be estimated to be ~ 1.4 m.

A second item of interest that is immediately noticeable on the two-dimensional image of the backscattered return from the crushed gravel is the elliptical shape of the image, as compared with the circular shape of the sand image. This oval shape is believed to be due to complex interactions of the incident electromagnetic field in the "cavities" formed within the gravel. That is, the wavelength (2.5 cm at $f_0 = 12.0$ GHz) of the field incident upon the gravel is such that some of the energy is coupled into the cavities created by the random orientation of the crushed gravel. Reflection and diffraction from the irregular surfaces and edges of the gravel cause the geometrical ray path traversed by the field coupled into these "cavities" (and subsequently scattered back to the radar) to be substantially longer than direct scattering from the surface of the gravel. The longer path traversed by the energy coupled into the cavities (and the associated increased time delay) relative to that of the directly-scattered fields causes the indirectly-scattered returns to appear further downrange in the two-dimensional radar-cross-section image of the crushed gravel. This in turn causes the image to be elongated in the down-range direction, giving the image its characteristic oval shape.

The final point to note in these figures is that the bright returns seen in the bottom portion of each image, and which are particularly apparent in the sand image, are due to specular scattering from the sample holder itself. It will be observed in the CCD images that although these returns are relatively large, they remain well-correlated over time, and thus do not detract from the objective of identifying disturbances which have been made to the surface of the "target under test."

Decorrelation Detectability Experiments

The intent of this set of experiments was to determine the level of disturbances to the crushed gravel and sand surfaces that could be detected by the compact range CCD measurement system. Both walking and raking across the surfaces of these distributed targets were easily detectable. As noted in the previous report [1], the average levels of decorrelation displayed on the raked-sample CCD images were roughly the same, regardless of whether the surface was "lightly raked" or "heavily raked." The main discernible difference was the *width* of the disturbance displayed on the image (due to the larger amount of material being disturbed with the heavier raking).

The discrete target sample displacement images (Figures A-8, B-8) are very effective in indicating the high sensitivity of the radar system, as well as highlighting the ability of CCD images to indicate minor disturbances to a target sample surface. This is clearly demonstrated in these images by the fact that both the simple removal of two stones or one tablespoon of sand resulted in detectable changes.

These sets of "decorrelation detectability" images also reinforce the conclusions discussed above regarding indirect scattering of the electromagnetic field by the crushed gravel. As mentioned earlier, the formation of a CCD image is accomplished by generating a pair of two-dimensional, complex images before and after the target sample is perturbed, following which the maximum likelihood estimate of correlation is used to detect areas of decorrelation between the complex image pair. The crushed gravel CCD images show areas of decorrelation extending well beyond the local area in which the gravel was perturbed. However, in all cases the extended areas of decorrelation are confined to the region directly downrange of the perturbed gravel sample. This is most clearly shown in the "discrete footsteps" and "discrete rock removal" images. These images plainly demonstrate that the apparent scattering of the incident field from the gravel surface downrange of where the gravel is perturbed has changed between the original and "post-disturbance" images. This phenomenon can be explained by realizing that perturbation of the gravel results in alteration of the geometrical ray path traversed by the propagating field beyond the point of perturbation, due to its being reflected and diffracted differently from the reoriented surfaces and edges of the gravel. Thus, not only the field scattered from the localized area of perturbation, but also that from the region behind the area of perturbation has changed, resulting in decorrelation in the final CCD image.

Moisture Effects Experiment

The intent of this set of experiments was to examine the effect of moisture in the decorrelation of CCD images. The device used to create the tire tracks in the target samples is the same as was used in the original set of experiments [1]. As seen from the images, the application of moisture to the surface of the target samples initially resulted in essentially total decorrelation. The target samples were then allowed to dry over a period of three days without further perturbation, during which the target samples were periodically remeasured, and subsequent CCD images were formed. As the moisture evaporated, the original disturbance (tire tracks) of the surface again became apparent in the processed images.

It will be noted that two sets of moisture experiment images exist for the crushed gravel. The first set is for crushed gravel that was measured in its "as-delivered" state; that is, most of the crushed stones were covered with fine, powdery dust. In comparing the "pre-moisture" and final "dry" CCD images for this first set of moisture experiment images, it can be seen that in addition to the tire tracks, there is also a low level of residual decorrelation throughout the final "77-hour" image (Figure A-13). In contrast, the problem of residual decorrelation is not evident in the final "dry" image of the second set of crushed gravel moisture experiment images (Figure A-18). The difference between the two gravel samples is that prior to performing the second set of moisture experiments, the dust had been rinsed off of the gravel. These two sets of experiments therefore directly imply that the residual decorrelation seen in the first data set is due to the fact that the dust particles were rinsed off of the gravel during the application of the water, and that the measurement technique was sensitive enough to detect the difference in the target sample.

The moisture experiment images for the sand are similar to that of the gravel in the sense that as the sand dried, the tire tracks "reappeared" in the CCD images. However, after 71 hours of drying, the overall level of decorrelation in the sand CCD image remained relatively high. There are two probable reasons for this: (1) after 71 hours, the sand had dried only to a depth of approximately 5/8 inches, and remained moist below this point to a depth of greater than six inches. Due to the ability of the incident field to propagate into the dry sand, as well as the relatively high moisture content of the subsurface sand, the residual level of decorrelation in the final image is not surprising. (2) The fine sand particles are much more susceptible to movement during application of the water than are the much larger crushed gravel stones. It is therefore reasonable to assume that some of the sand material was dislodged from its original position during the experiment, and as demonstrated previously, this will have a measurable effect upon the correlation levels in the final CCD image.

2.3 Spatial Decorrelation in CCD Images

The objective of this set of experiments is to investigate the sensitivity of the coherent change detection measurement process to alterations in the "viewing" geometry, or in other words, changes in the relative spatial location of the SAR sensor between observations of the target. Decorrelation of a processed CCD image that can be attributed to imprecise relocation of the imaging sensor is typically referred to as spatial decorrelation. Spatial decorrelation is a major concern in actual operational scenarios, since it is extremely difficult to align repeat passes of a SAR platform over the same site to within a high degree of tolerance. Spatial decorrelation can easily be simulated in the compact range by introducing varying degrees of angular offset into the elevation and azimuth axes of the positioner controller, and can be isolated for study by keeping the distributed target sample itself undisturbed.

2.3.1 *Understanding Spatial Decorrelation*

Spatial decorrelation can be better understood by considering the phenomenon of "speckle." A distributed target (gravel, sand, etc.) can be modeled as a collection of randomly-oriented scatterers, and it is assumed that there are many such scatterers within each resolution cell of

the image. The total scattered field from the distributed target is the coherent sum of the backscattered return from each scatterer. If the target remains undisturbed between two observations which are separated in time, and is imaged from exactly the same coordinates, the resulting images will be identical in both amplitude and phase. However, if the observation geometry is altered, a different interference pattern will result for each resolution cell, changing the amplitude and phase of the resolution cell in the processed image, even though the resolution cell covers the same physical area. Thus, the process of imaging a distributed target can be termed to be deterministic, but spatially random [4], [9]. It is easily understood, then, that changes in the observation geometry between measurements will result in a loss of coherency in the final CCD image.

Spatial decorrelation of a CCD image is a function of both "baseline" decorrelation (decorrelation resulting from observing the target from two slightly different look angles), and "rotation" decorrelation (decorrelation due to observation of the target from different aspect angles). Stated mathematically,

$$\gamma_{spatial} = \gamma_{baseline} \cdot \gamma_{rotation} , \tag{6}$$

where

$\gamma_{spatial}$ = correlation coefficient due to imaging geometry,

$\gamma_{baseline}$ = correlation coefficient due to observation of target from differing look angles,

$\gamma_{rotation}$ = correlation coefficient due to observation of target from differing aspect angles,

and where the decorrelation function δ is given by [10]

$$\delta = 1 - \gamma . \tag{7}$$

2.3.2 *Correlation Model*

Several authors have presented models of spatial decorrelation [4], [10], [11]. In general, it is shown in these derivations that there is a Fourier transform relation between the correlation function and the radar system impulse response, and that this relationship can be used to determine the correlation as a function of variation in the spatial geometry of the radar sensor.

Summarizing the results in [4] and [11], the measured complex signal for a resolution cell in a final processed SAR image at position (x_0,y_0) can be represented as [11]

$$s_{x_0,y_0} = \iint f(x,y) e^{\left(-j\frac{4\pi r}{\lambda}\right)} W(x - x_0, y - y_0) dxdy + n , \tag{8}$$

where $f(x,y)$ represents the complex backscatter from the distributed target, λ is the radar wavelength, r is the distance from the radar to the center of the resolution cell, and n is the complex noise signal added to the radar signal by the receiver. $W(x,y)$ is the system impulse response, and is generally represented as a sinc function, such that

$$W(x,y) = \frac{\sin\left(\frac{\pi x}{\rho_x}\right)\sin\left(\frac{\pi y}{\rho_y}\right)}{\frac{\pi x}{\rho_x}\frac{\pi y}{\rho_y}}, \tag{9}$$

where ρ_y = c/2BW (c = speed of light; BW = system bandwidth) and ρ_x = L/2 (where L is the length of the synthetic aperture), and are respectively the maximum achievable range and azimuth image resolutions. Next, let s_1 represent the backscattered signal from a resolution cell for the initial image, let s_2 represent the signal from the same resolution cell after the incidence angle for the illuminating field has changed (due to displacement of the transmit antenna of the radar in either elevation or aspect angle), and assume that the resolution cells of the imaged scene consist of uniformly distributed and uncorrelated scattering targets. Evaluation of the normalized average cross-correlation ($\langle s_1 s_2^* \rangle$) of s_1 and s_2 then leads to expressions for $\gamma_{baseline}$ and $\gamma_{rotation}$ [4], [11]. These expressions have been recast into a form commensurate with the compact range measurement geometry, such that

$$\gamma_{baseline} = 1 - \frac{2\alpha\rho_y \sin\psi}{\lambda}, \tag{10}$$

where α and ψ are as shown in Figure 10, and

$$\gamma_{rotation} = 1 - \frac{2\Delta\phi\rho_x \cos\psi}{\lambda}, \tag{11}$$

(for a sinc(x) azimuth impulse response) where $\Delta\phi$ is the amount of rotation of the resolution cell between observations. The calculated $\gamma_{baseline}$ and $\gamma_{rotation}$ functions are plotted in Figure 1, where it may be seen that the spatial correlation decreases linearly as the difference in look angle (α) and aspect angle ($\Delta\phi$) increases between the two observations of the target area. These expressions are strictly true only for the case in which the surface being imaged is flat and has no tilt, and in which there is no misregistration error for the image pair [10].

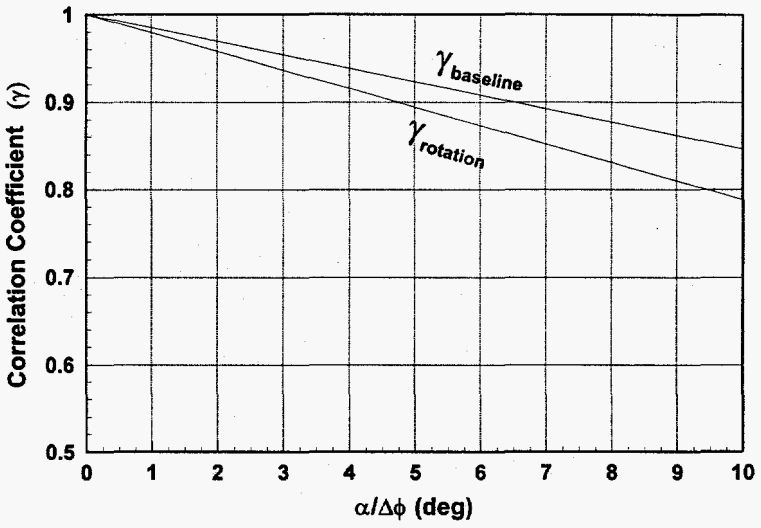

Figure 1. Spatial correlation factors $\gamma_{baseline}$ and $\gamma_{rotation}$ plotted respectively as functions of the look angle (α) and aspect angle ($\Delta\phi$).

2.3.3 *Comparison of Model and Experimental Results*

Measured data from the compact range has been compared with the correlation formulations given in (10) and (11); this data was generated by creating two-dimensional image pairs of "pea gravel" which had been raked smooth. The image pairs were obtained by forming an initial image of the gravel surface, and then forming subsequent images of the surface after incrementally offsetting the sample holder in either elevation (α) or azimuth ($\Delta\phi$), while keeping the other axis of motion constant. After registering an image pair (Section 2.3.5), the maximum likelihood estimate of correlation was then computed for the pair of images. A 2' x 2' center subsection of the resulting correlation image was used to compute an average correlation value for the image. The correlation results are plotted in Figures 2(a) and (b), along with the predicted correlation values derived from (10) and (11). Although the measured values of $\gamma_{rotation}$ agree more closely with the predicted results than do the measured values of $\gamma_{baseline}$, it is readily seen that the measured and predicted values diverge rapidly from each other beyond offset angles greater than about 0.5° for the $\gamma_{baseline}$ data, and 1° for the $\gamma_{rotation}$ data. These figures therefore indicate that there are unmodeled sources of decorrelation associated with the measured correlation values.

In analyzing these curves, there are two major concerns regarding the applicability of the theoretically-predicted correlation functions to the measured data which need to be explored. One of these issues is that the predictions assume a circular Gaussian statistical model for the scatterers in a resolution cell [10], or in other words, that the type of speckle pattern observed is "Gaussian speckle." The second issue is that (10) and (11) assume no decorrelation due to image misregistration.

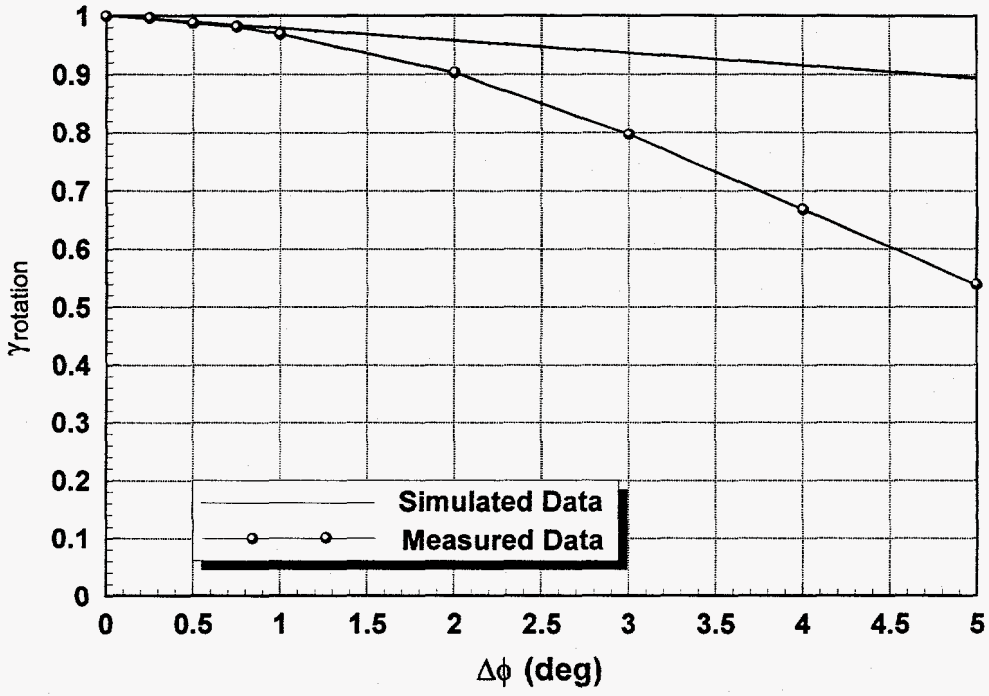

Figure 2(a). Comparison of measured and predicted values of $\gamma_{rotation}$ as a function of aspect angle ($\Delta\phi$).

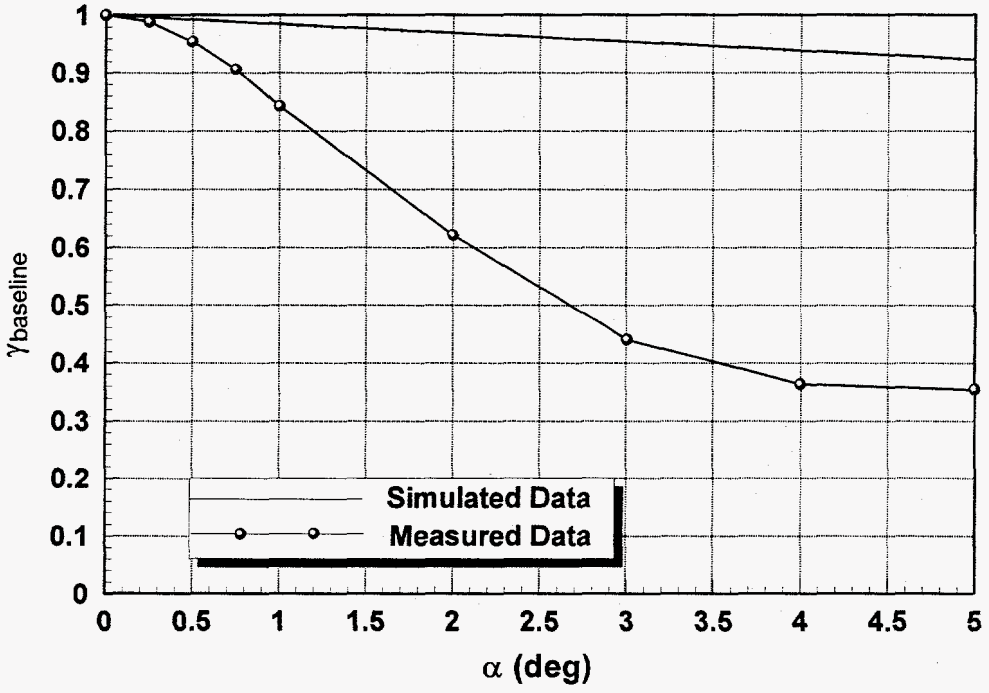

Figure 2(b). Comparison of measured and predicted values of $\gamma_{baseline}$ as a function of look angle (α).

In a Gaussian statistical model, it is assumed that the resolution cell is comprised of a large number N of independent scatterers and that the surface roughness (σ_h) does not influence the statistics of the speckle pattern (that is, $\sigma_h > \lambda$) [12]. In contrast, the ISAR measurements performed at the compact range measurement facility utilized very wide bandwidth (typically 8.0 GHz) stepped frequency waveforms with a center frequency of 12.0 GHz ($\lambda \approx 1$ inch) and large aspect angle rotational extents in order to achieve unwindowed resolution cell sizes of approximately 0.74" x 0.74". In the case of measurements of small pea gravel, in which the average diameter of an individual piece of gravel is roughly 0.25 inches (~ λ/4), this results in an unwindowed resolution cell encompassing only about 8 or 9 individual scattering centers. The interference patterns resulting from such a resolution cell are referred to as "small-N" speckle [12], and will typically have non-Gaussian statistics for the measured complex amplitude of its backscattered return. It has been shown, in fact [13], that as the spatial resolution approaches one wavelength, that "surface speckle" disappears, although "volume speckle" is still present. The question arises, then, as to how well the correlation functions predicted by (10) and (11) can be expected to fit the measured non-Gaussian data.

2.3.4 *Numerical Simulation of Scattering from a Resolution Cell Having Dimensions on the Order of a Wavelength*

In order to address the question of how well the correlation functions (10) and (11) may be expected to fit "small-N" speckle data, a numerical simulation was performed to calculate the decorrelation associated with rotation of a resolution cell composed of a small number of scatterers, and the results were compared with the correlation function given by (11). This was accomplished by simulating an ISAR measurement of nine discrete point scatterers located within a resolution cell and spaced as shown in Figure 3(b). The data was processed in such a manner as to form images of the target area with unwindowed resolution cell sizes having dimensions of ~ 0.8λ x 0.8λ. Details of the simulation process are given in Appendix C. An initial image of the unrotated point scatterers was formed, and then the position of each scatterer was adjusted so as to simulate rotation of the entire cell in aspect by an amount $\Delta\phi$, as indicated in Figure 3(a), after which a second image of the point scatterers was computed. Following formation of this pair of two-dimensional complex images, the maximum likelihood estimate of correlation ($\gamma_{rotation}$) of the two images was computed, and the average value of $\gamma_{rotation}$ for the resolution cell (the resolution cell being composed of several pixels) containing the point scatterers was then calculated. This process was repeated several times in order to obtain the value of $\gamma_{rotation}$ as a function of rotation of the resolution cell ($\Delta\phi$). The values determined from this simulation are plotted in Figure 4, along with $\gamma_{rotation}$ calculated using (11), with $\rho_x = 0.8\lambda$, and $\psi = 0$ (point scatterers are assumed to be rotated in the plane of the incident field).

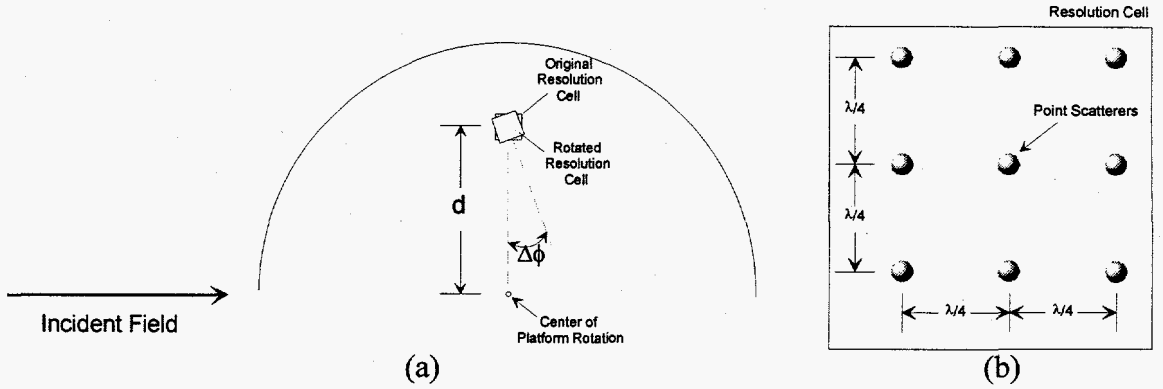

Figure 3. Simulated ISAR measurement of nine discrete point scatterers located within a resolution cell having dimensions of ~ 0.8λ x 0.8λ. (a) Simulated rotation of the resolution cell; (b) location of point scatterers within the resolution cell.

It is seen from the curves in Figure 4 that the simulation results in substantially higher correlation values versus aspect angle rotation for a small number of scatterers than that predicted by the Gaussian statistical model. This is in agreement with [13], who indicated that speckle becomes correlated for large changes in the angle of the incident field as image resolution is increased. The simulation therefore indicates that at the very least, the $\gamma_{baseline}$ and $\gamma_{rotation}$ correlation values predicted by (10) and (11) should be conservative with respect to the correlation values that would be expected to be measured at the compact range measurement facility.

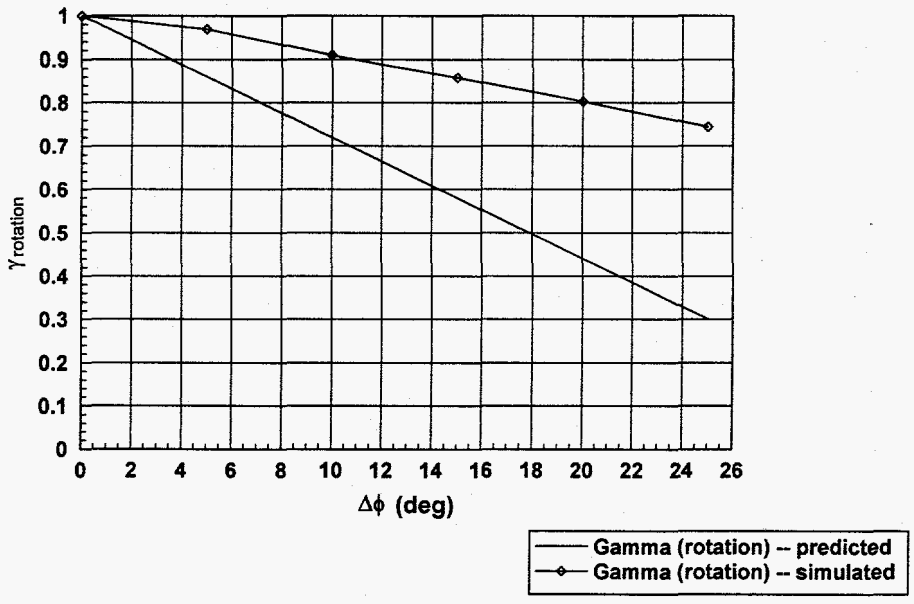

Figure 4. Values of $\gamma_{rotation}$ (computed as a function of aspect angle ($\Delta\phi$)) derived from ISAR simulation, plotted together with values of $\gamma_{rotation}$ predicted by Equation (11).

2.3.5 *Image Misregistration*

The second item of concern regarding the application of the theoretically-predicted correlation functions given by (10) and (11) to predict image pair decorrelation of the data measured at the compact range measurement facility--i.e., that these predictions assume no decorrelation due to image pixel misregistration--must now be addressed. Similar to spatial decorrelation, resolution cell misregistration is an artifact of variation in the geometry of the radar relative to the target between observations, and consists of the fact that the two images created during the two "passes" are not exact overlays of the same physical area. That is, in general there is some amount of offset in range and azimuth between the resolution cells of a pair of images used to form a CCD image. Furthermore, since the incidence angle of the impinging electromagnetic wave onto the target is different for the two images, the images will have different ground resolution cell sizes in the down-range direction. Thus, the resolution cells consist of different sets of scatterers, such that the sum of their scattered fields, or the interference patterns resulting from the scatterers within the resolution cells, are different. This of course leads to degeneracy in the coherency of the CCD image, and is called "registration decorrelation." It can therefore be seen that in the most general case, one of the images must be scaled, translated, and rotated before application of the CCD algorithm in order to obtain a true measure of the spatial decorrelation.

In assessing how registration of the complex images generated from measured ISAR data of distributed targets could best be accomplished, some guidance was found in the literature, where a multiplicity of approaches have been used to properly "re-register" pairs of images on a subpixel basis. Li and Goldstein used a technique in which the correlation coefficient was calculated between two images for various discrete pixel offsets in range and azimuth, following which an interpolation algorithm was applied to the data to determine the fractional offset resulting in the maximum correlation value. This procedure was estimated to register images to within ~ 0.05 pixels [11]. In another approach, image offsets were determined to within ~ 0.1 pixels [14] by extracting subgrids from each image, assessing the SNR of an interferometric image created using the two sub-images, choosing a new subgrid from the second image, and repeating the procedure to find the offsets in range and cross-range which resulted in the maximum SNR. Again, exact offsets were found by performing an interpolation of the data. A third technique [15] was to interpolate the second image on a subpixel basis, form an interferometric image using the subsampled image, determine the average fluctuation of the phase in the resulting image (the fluctuation being defined as the summation of the phase difference between all adjacent pixels in an image), again interpolate the second image and calculate the phase fluctuation, adjust the registration parameters according to the change in the fluctuation value, and repeat the process until the fluctuation value is minimized. After determining the optimal range and cross-range pixel offsets, the second image is then interpolated in the range direction with varying scaling factors to again minimize the average phase fluctuation value. This method was reportedly also able to register two images to an accuracy of 0.1 pixels.

Although a methodology similar to that of Li and Goldstein was manually employed to register the compact range-generated image pairs with some success, it was found to be most

efficient (and certainly most convenient) to use image registration algorithms and FORTRAN programs developed by P. H. Eichel, et. al., to register pairs of image data. These algorithms are discussed in detail in [16] and so will be only briefly summarized here. Essentially, the registration of pairs of images are accomplished in three steps. In the first step, tie points (or "control points") are generated for the image pair. This basically involves making measurements of the local displacement vector from one image to the other in many places throughout the image. The computation of the tie points is itself a two-step process. The images are first detected and downsampled, and a few patches of the image are used to calculate an approximate "affine" transformation warping function [16]. Next this affine transform is used to compute the position of image patches in one image that approximately correspond with patches in the second image, and tie points are then calculated using the full-resolution complex images. The second step of the registration process is to utilize the accurate set of tie points that have been obtained to calculate a polynomial warping function which maps a two-dimensional location in one image to the corresponding location in the second image. This warping function is determined by linear regression. The third step in the process is to resample the second image using a bilinear interpolator (in accordance with the warping function previously determined) such that it precisely overlays the first image.

Two examples of correlation images formed from unregistered image pairs clearly illustrate the need for image registration. As a first example, when a pair of images are offset by some azimuth angle, it is to be expected that scatterers on the outer periphery of the sample holder would become misregistered more quickly than those near the center of rotation, simply due to the fact that they travel farther per angular offset. (The intercepted arc length s for a sector of a circle having a radius r and subtending an angle θ is given by $s = r\theta$; hence, a larger distance from the center results in a larger arc length.) This is particularly well-exemplified in Figure 5, which is the image created by calculating the maximum likelihood estimate of correlation for two unregistered images of pea-gravel having angles of incidence offset from each other in azimuth by 0.75°. This correlation image shows the image pair to be well-correlated at the center, and to become progressively less-correlated as a function of displacement from the center, resulting in an interesting "eyeball" pattern. Similarly, misregistration occurs, as has been stated, when offsetting the elevation axis of the sample-holder positioner because the images have slightly different "ground" pixel sizes due to the difference in look angle, as well as differing range pixel offsets. It is therefore to be expected that the level of decorrelation will vary as a function of the slant range in the correlation image, and such is indeed the case, as seen in the pre-registration correlation image shown in Figure 6, created from two unregistered complex images of smooth pea-gravel having angles of incidence offset in elevation by 0.5°.

As was noted, the correlation data values plotted in Figures 2(a) and 2(b) were in fact derived from image pairs which, prior to calculation of the maximum likelihood estimate of correlation, had been registered using the Eichel algorithm. This algorithm was found to be quite effective in improving the level of correlation of the images. The improvement afforded by the registration algorithm was understandably small for image pairs having small offset angles which were well-correlated ($\gamma > 0.9$) prior to application of the algorithm.

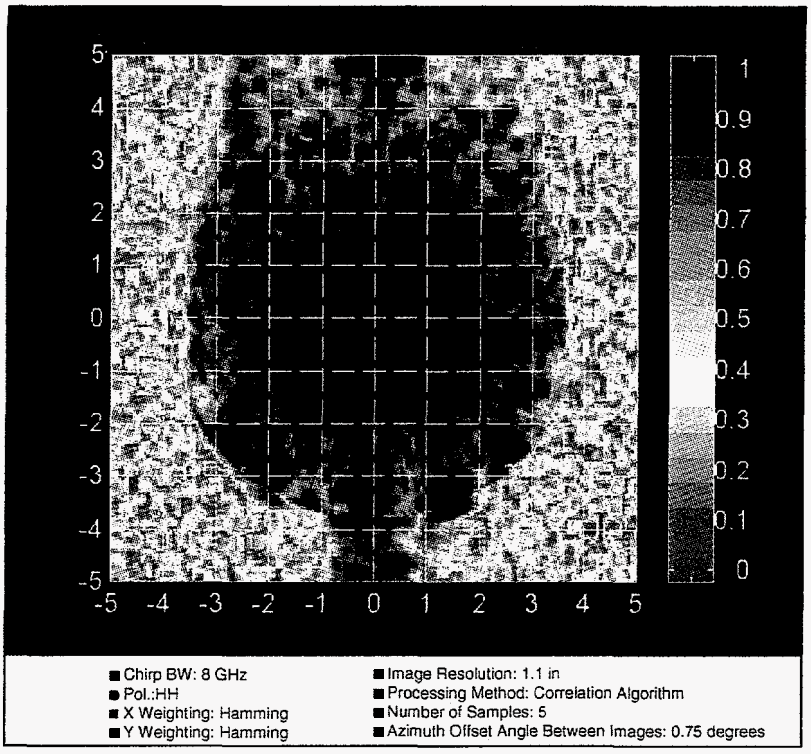

Figure 5. Pre-registration correlation image resulting from two azimuthally-offset measurements of smoothed pea-gravel; angular offset difference is 0.75°.

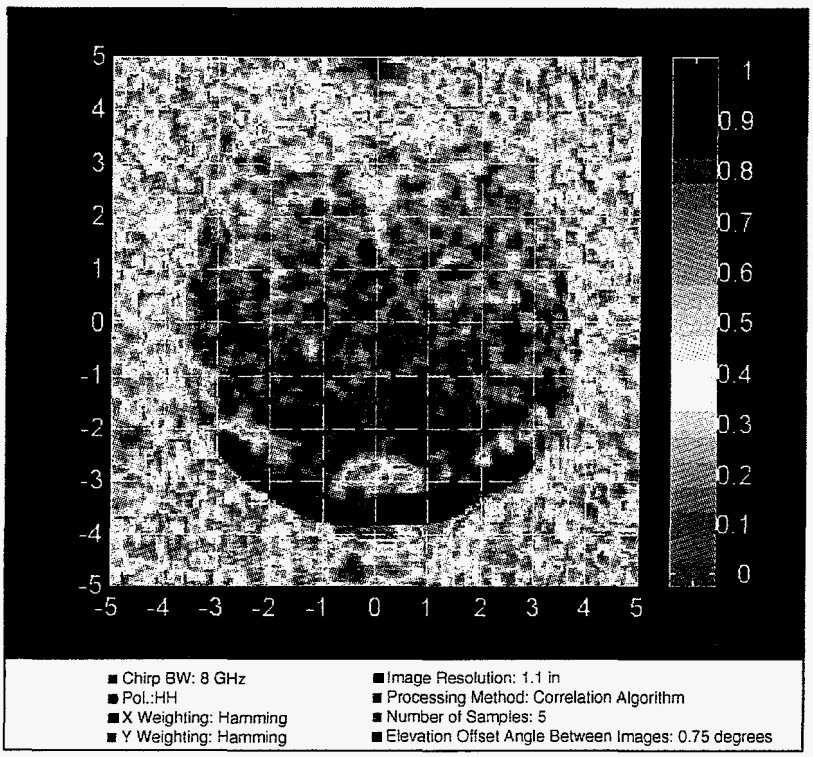

Figure 6. Pre-registration correlation image resulting from measurements of smoothed pea-gravel from two different look angles; angular offset difference is 0.5°.

However, for image pairs having larger offset angles, for which pre-registration correlation values ranged from about 0.35 to 0.9 ($\gamma < 0.35$ indicates nearly total decorrelation of the image pair, at which point the algorithm was generally ineffective), application of the registration algorithm improved the correlation of the images by an average of 42%. Despite the effectiveness of the registration algorithm, the fact that the curves are widely divergent indicates that there is a residual source of misregistration.

A particular problem with image pairs created by offsetting either the azimuth or elevation axis of the sample holder in the compact range is the fact that polar reformatting is used to produce focused images of the distributed target samples. This problem is exacerbated by the fact that the signal processing software used to form the images assumes that the sample holder platform is rotated in the plane of the incident field, which in essence means that although the down-range resolution of a stepped-frequency ISAR image is in actuality given by

$$\Delta r_d = \frac{c}{2n\Delta f_s \cos\psi}, \tag{12}$$

the $\cos\psi$ factor in the denominator has been neglected by the system software. The misregistration problems caused by polar reformatting can be understood by very briefly reviewing the underlying principles of ISAR image formation.

2.3.6 *Polar Reformatting*

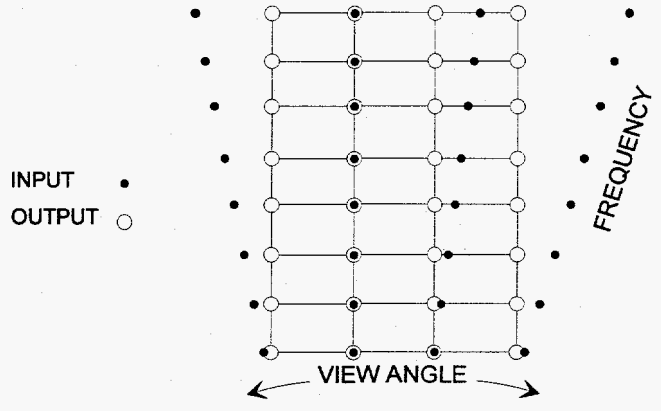

Figure 7. Resampling of measured data into a rectangular format in two-dimensional frequency space (from [17]).

In an ISAR measurement, data samples of a target's backscattered response are collected over the stepped-frequency bandwidth of the radar at uniformly-spaced discrete rotational-angle positions, and as such, are referred to as being polar formatted [17]. Typically, a two-dimensional Fourier transform is used to transform the measured data into the image domain.

However, polar-formatted data is non-uniformly spaced in the spatial frequency domain, such that Fourier transform processing of the polar-formatted data results in unfocused, or blurred, images. The severity of the problem is intensified as the percentage bandwidth of the waveform increases, and very high resolution often results in significant scatterer migration through the range-resolution cells [17]. One method of overcoming this problem is to resample the measured data into a rectangular format in two-dimensional frequency space as shown in Figure 7 [17], after which Fourier transform processing can be used to produce a focused image.

While this methodology works well for producing focused images at a given look angle, reformatting two images formed from different look angles will result in the two sets of data not being resampled onto precisely the same grid, especially since the assumptions of the rotation plane of the measurement are incorrect. Further, since sampled, polar-formatted data points tend to deviate more from a rectangular format with increasing distance from the center of rotation (as depicted in Figure 7), such that a higher degree of resampling is required to properly focus the image, there will be increasingly large discrepancies between image pairs both as a function of radius, and for images generated from azimuthally-offset measurements as the offset angle is increased. Thus, while two individual images may themselves be focused, polar reformatting unfortunately creates additional sources of misregistration in the final CCD image.

It was shown in [11] that for large signal-to-noise ratios (SNR >> 1), pixel misregistration can be factored into the relationship for baseline decorrelation as

$$\gamma_{baseline} = \gamma_{baseline_0} \cdot \mathrm{sinc}\left(\frac{\pi \Delta y}{\rho_y}\right), \tag{13}$$

where $\gamma_{baseline_0}$ is the baseline correlation factor with no image misregistration as given in (10), and Δy is the down-range pixel misregistration offset due to the difference in look angle between the two measurements. (A similar expression can be given for $\gamma_{rotation}$.) Using this relationship, along with the measured and predicted baseline correlation values, the effective pixel offset (Δy) can be calculated which would result in the difference seen in the curves plotted in Figure 2(b). These values (in terms of fractions of a resolution cell) are given in Table 2 below.

TABLE 2. Calculated Effective Pixel Offsets for Data Points Plotted in Figure 2(b)

α (degrees)	$\gamma_{baseline}$ (predicted)	$\gamma_{baseline}$ (measured)	Δy
0.25	0.996	0.988	0.07
0.50	0.992	0.954	0.16
0.75	0.988	0.910	0.23
1.0	0.985	0.842	0.30
2.0	0.969	0.621	0.50
3.0	0.954	0.440	0.63
4.0	0.938	0.363	0.69
5.0	0.923	0.354	0.69

2.3.7 *Summary*

The objective of these measurements and analysis has been to investigate the sensitivity of the coherent change detection measurement process to alterations in the "viewing" geometry, or in other words, changes in the relative spatial location of the SAR sensor between observations of the target. In an effort to accomplish this objective, formulations have been given which describe image correlation as a function of variation of angular offset in the elevation and azimuth observation planes of the radar sensor between observations. These expressions assume a Gaussian statistical model for the scatterers in a resolution cell, and as such were shown to be conservative estimates with respect to the correlation values that would be expected to be measured as the resolution cell size approaches a wavelength.

Measured correlation data was compared with the theoretical predictions, and was found to be widely divergent from the theory for angular offsets greater than about 1.0°. The lack of agreement between theory and measurement is felt to largely be attributable to unmodeled sources of misregistration decorrelation associated with polar reformatting of the compact range data. The polar reformatting problem is a consequence of the fact that two images formed from data measured at different look angles will not be resampled onto precisely the same grid during signal processing and application of a focusing algorithm to the data. Two images thus formed will be well-correlated if the image registration mismatch is substantially less than the image resolution; however, as the resolution is increased, the mismatch tolerance is decreased. Thus, the problem is analogous to an optical "depth of focus," in which the depth of focus becomes small for high resolution images [13].

Complex imagery received from the compact range is currently accepted as a "product," having been calibrated and processed by the measurement system software. Correlation processing is then performed offsite of the measurement facility. It is felt, however, that the misregistration problem can be addressed by applying polar reformatting to the measured data following, as opposed to prior to, registration of the complex images, and that this will substantially improve the offset-angle correlation of the images.

3. INTERFEROMETRIC MEASUREMENT METHODOLOGY AT THE FOLDED COMPACT RANGE MEASUREMENT FACILITY

Synthetic aperture radars have long been used to form two-dimensional images of terrain, etc., in which the down-range and cross-range resolutions of images are dictated respectively by the bandwidth of the radar and the length of the synthesized antenna aperture. A more recent innovation has led to the ability to resolve the third dimension, or height, of these digitally-created images, and is typically referred to as "interferometric synthetic aperture radar" (commonly referred to as either INSAR or IFSAR in the literature [3], [10], [11], [16]). IFSAR techniques for the purpose of obtaining high resolution digital elevation maps have been investigated and successfully demonstrated by several researchers, a few of which are referenced here [3], [4], [9], [10], [11], [16]. The basic operating principle of an IFSAR is fundamentally the same as that of a direction-finding radar (sometimes referred to as "phase-comparison monopulse" radar [18]), being that a radar interferometer may be formed by spatially separating two antennas. Backscattered signals are coherently measured at both antennas, and because of the slight difference in imaging geometry between the two antennas, a small phase difference will exist in the images created by the signals that are received and processed. The magnitude of the phase difference is dependent upon the height of the object or terrain being imaged. Due to the fact that the phase difference is measured relative to the wavelength of the transmitted/received waveform, the height measurements can be accurate on the order of the radar wavelength.

The extent of the spatial separation of the antennas is typically referred to as the "baseline," and is one of the major factors influencing the fidelity of the interferometric system. Two approaches for implementing an IFSAR system are generally discussed in the literature [4], [9], [19], [20], [21], [22], and in principle differ mainly in the manner in which the baseline is formed. In one case, the baseline is created by two physical, spatially-separated antennas. This approach is typically used, for example, in an airborne implementation in which the antennas can be mounted sufficiently far apart to create an acceptable baseline. One of the antennas is used to transmit the electromagnetic field, after which both antennas simultaneously intercept backscattered signals from a given target. A further adaptation of this approach, in which the radar system is operated in a multiplexed mode (in which a signal is transmitted and received by one antenna, and then transmitted and received by the other antenna) has been demonstrated on the SNL Twin Otter-based IFSAR experimental platform [3].

The second approach is to create a "synthetic baseline" by utilizing a single antenna and forming the baseline by correlating the measured backscattered returns from a given target area from repeat passes of the radar platform over the same site. This method is typically used in spaceborne implementations in which the spacecraft has a nearly repeat ground-track orbit [4], [9], [11], [23], [24], although it has also been successfully implemented on airborne platforms [25], [26], [27]. Implicit in this "repeat-pass" approach is the necessity of the target area remaining unchanged between observations. In fact, a primary determinant in accurately assessing the phase difference in an interferometric image is the correlation properties (or "scene coherency" [11]) of the backscattered return. As will be shown, lack of

correlation between the backscattered returns for two different observations leads to an increase in the standard deviation of measured phase difference values, ultimately resulting in uncertainty in the height measurements. Hence, this technique could not be used, for example, to measure ocean surfaces.

The utility of using a compact range to quantify the deleterious effects of image decorrelation on digital height mapping accuracy thus becomes readily apparent. This, then, is the impetus behind developing a method whereby the SNL folded compact range configuration could be utilized to simulate repeat pass interferometric measurements. The objective of this segment of the report is therefore to describe both the theoretical and practical aspects of performing interferometric measurements in the folded compact range environment, and to provide examples of digital height maps of targets measured in the compact range.

Section 3.1 provides a brief overview of how relative height measurements are obtained with a conventional two-pass interferometric measurement system. Section 3.2 then describes how analogous measurements can be made in the folded compact range environment, and further shows that the equation for height resulting from the compact range geometry is precisely equivalent to the relative height term generated by the conventional two-pass IFSAR measurement system. Section 3.3 discusses the effect of image correlation on digital height map fidelity, and finally, Section 3.4 provides several examples of interferometric images generated in the folded compact range.

3.1 Two-Pass IFSAR Measurements

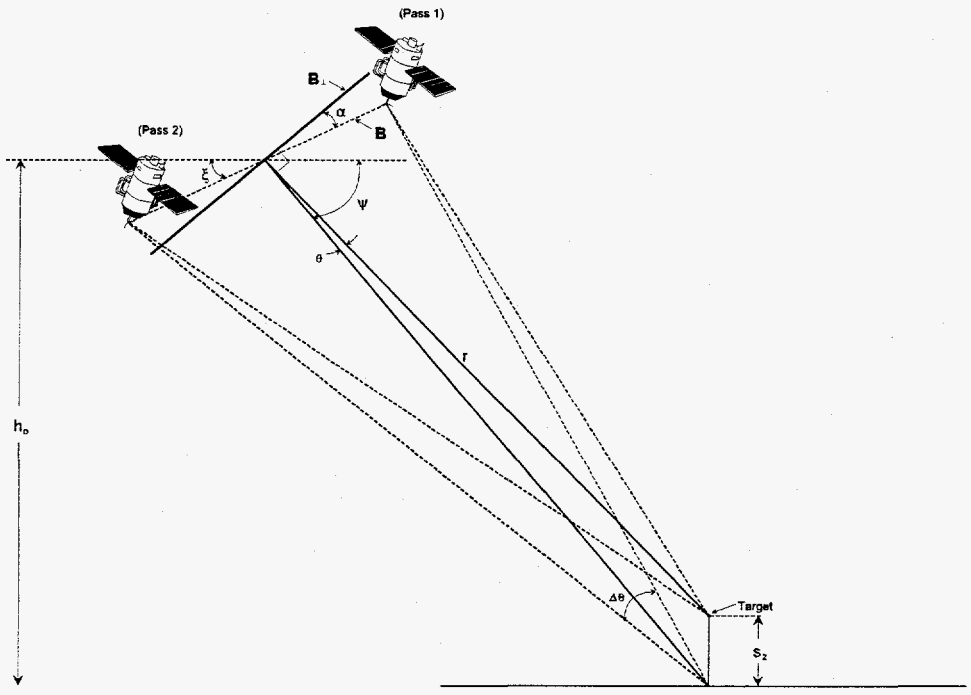

Figure 8. Diagram of two-pass IFSAR measurement system.

A depiction of a two-pass interferometric measurement system is shown in Figure 8. It is of importance to note that the theory formulated here is applicable to any interferometric system employing a radar platform having a single antenna, and which synthesizes a baseline by correlating backscattered signals from a given target area from repeat passes over the same site. As previously described, and as shown in the diagram, the baseline (B) is the physical separation distance between the two spatial locations of the antenna during subsequent passes of the radar platform over the target scene.

From the geometry given in Figure 8, the baseline (B) can be projected onto a line ($B_\perp$) perpendicular to a line joining the scene center and the baseline by the relationship

$$B_\perp = B\cos\alpha = B\sin(\xi+\psi). \tag{14}$$

Further, it can also be seen from the geometry that

$$h_0 - s_z = r\sin(\psi-\theta), \tag{15}$$

where

$$r\sin(\psi-\theta) = r\sin\psi\cos\theta - r\cos\psi\sin\theta. \tag{16}$$

A diagram showing the observational geometry in greater detail is shown in Figure 9.

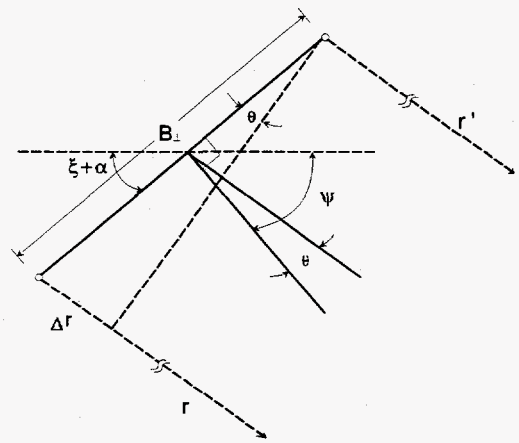

Figure 9. Observation geometry of IFSAR measurement system.

The interferometric phase that will be measured at any given point can be accurately modeled as the wavenumber multiplied by twice the differential propagation path length between the target and the two antennas (since the system is a two-pass interferometer); that is,

$$\phi = 2k(r-r') = 2k\Delta r, \tag{17}$$

where ϕ is the measured phase difference between the two passes.

From Figure 9, it is clear that

$$\phi = \frac{4\pi}{\lambda} B_{\perp} \sin\theta; \tag{18}$$

substituting this relationship into (15) gives,

$$h_0 - s_z = r\sin\psi\cos\theta - \frac{r\lambda\phi}{4\pi B_{\perp}}\cos\psi\,. \tag{19}$$

The first term in (19) can be interpreted as a linear phase term which results in a constant rate of phase change versus range across the image. This linear phase change can be subtracted from the interferometric image, resulting in

$$s_z = \frac{r\lambda\phi}{4\pi B_{\perp}}\cos\psi\,, \tag{20}$$

which thus provides a means of determining relative target heights in the interferometric image.

3.2 Folded Compact Range Interferometric Measurements

The fundamental operating principle of an IFSAR measurement system is that the differential phase which allows the height of a target to be resolved results from imaging the target from spatially diverse geometries. In a conventional IFSAR system, this is accomplished by imaging a given target area from slightly offset repeat passes over the same site, as was shown in Section 3.1. It was postulated, however, that the spatial diversity necessary to create an interferometric image in the compact range could equivalently be obtained by offsetting the elevation axis of the sample holder between measurements of the target. That is, a two-pass IFSAR measurement system could be synthesized by forming two images of a target sample, each of which is oriented at a slightly different look angle relative to the planar reflector during the ISAR imaging process. The two images could then be correlated to extract the differential phase information, from which the effective height of the target sample may then be calculated.

To clarify this concept, a two-dimensional diagram of the planar reflector and distributed target sample holder in the folded compact range geometry is shown in Figure 10. For this analysis, the coordinate system axes are located at the center of the planar secondary range reflector, as shown. Also, a flat phase front normal to the direction of propagation is assumed.

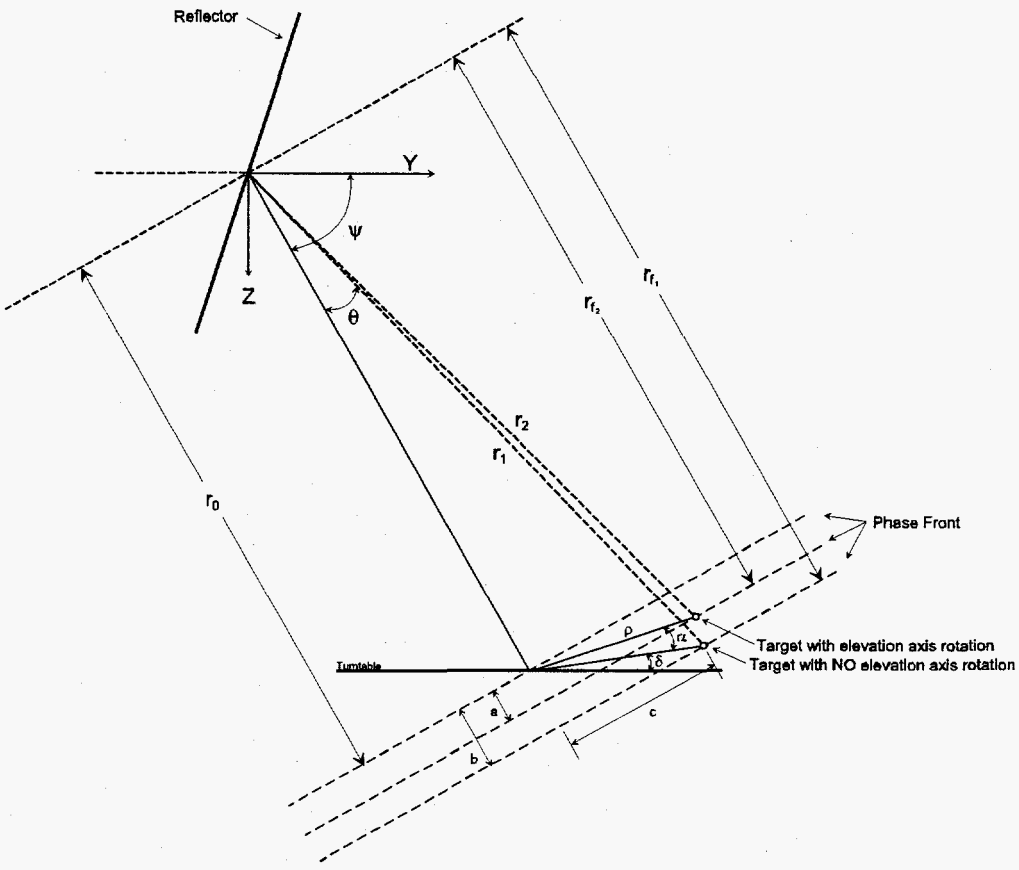

Figure 10. Diagram of folded compact range interferometric measurement geometry.

Referring to Figure 10, the phase difference between the scattered return from a point scatterer located at two different ranges from the origin, r_1 and r_2 (resulting from rotation of the elevation axis of the sample holder), is given by

$$\phi = \frac{4\pi}{\lambda}\left(r_{f_1} - r_{f_2}\right). \tag{21}$$

From the geometry of the diagram it can be seen that

$$r_{f_1} = r_0 + b = r_0 + \rho\cos\left(\psi + \delta\right) \tag{22}$$

$$r_{f_2} = r_0 + a = r_0 + \rho\cos\left(\psi + \delta + \alpha\right), \tag{23}$$

where α is the tilt of the elevation axis of the sample holder turntable between "passes." Therefore,

$$\begin{aligned} \Delta r_f &= r_{f_1} - r_{f_2} \\ &= \rho\left[\cos\left(\psi + \delta\right) - \cos\left(\psi + \delta + \alpha\right)\right] \end{aligned} \tag{24}$$

Assuming that α is small, Δr_f can be approximated as

$$\Delta r_f \approx \rho\alpha \sin(\psi + \delta). \tag{25}$$

It can also be seen from Figure 10 that the cross-boresight distance (c) to the target is given by

$$c = \rho \sin(\psi + \delta) \tag{26}$$

and

$$c = r_1 \sin\theta, \tag{27}$$

such that

$$r_1 \sin\theta \approx \frac{\Delta r_f}{\alpha}. \tag{28}$$

Similarly, the distance to the target along the boresight direction is found to be

$$r_1 \cos\theta = \sqrt{r_1^2 - (r_1 \sin\theta)^2} \approx \sqrt{r_1^2 - \left(\frac{\Delta r_f}{\alpha}\right)^2}. \tag{29}$$

The height of the target can now be found relative to the coordinate axes centered on the planar reflector as

$$\begin{aligned} z_t &= r_1 \sin(\psi - \theta) \\ &= \sin\psi \sqrt{r_1^2 - \left(\frac{\Delta r_f}{\alpha}\right)^2} - \frac{\Delta r_f}{\alpha}\cos\psi \end{aligned} \tag{30}$$

As in the case of a true two-pass interferometric system, the first term in z_t is the linear phase taper across the scene. This linear phase change can be subtracted from the interferometric image, resulting in a measurement of the relative height of objects in the interferometric image. Assuming that this has been done, substituting (30) into (21) then gives the following result for the relative height of the target:

$$h_t = \frac{\lambda\phi}{4\pi\alpha}\cos\psi. \tag{31}$$

This equation for h_t is precisely equivalent to that previously derived for s_z (20), the relative height term for a conventional two-pass interferometric system. This can be shown by referring to Figure 11, a simplified version of Figure 10.

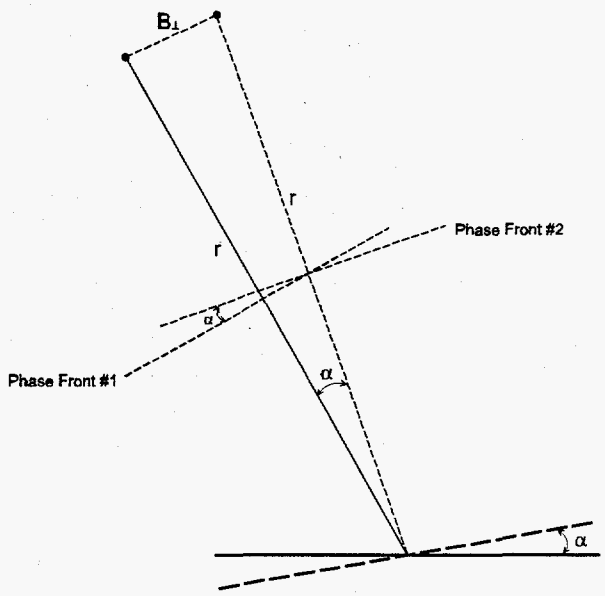

Figure 11. Simplified diagram of folded compact range interferometric measurement geometry.

Again reiterating the assumption that the electric field incident upon the turntable is a uniform plane wave, it can be seen from Figure 11 that at the center of rotation, the action of tilting the elevation axis of the turntable by an amount α is equivalent to illuminating the turntable from a source that is at a position equidistant in range, but at an angle of α relative to the original position. The radial distance $B_\perp$ between the two apparent source positions can be calculated from simple geometry to be

$$B_\perp = 2r\sin\left(\frac{\alpha}{2}\right); \tag{32}$$

if α is small, then

$$B_\perp \approx r\alpha\,. \tag{33}$$

Substituting $\alpha \approx B_\perp / r$ into the expression for h_t gives the result that

$$h_t = \frac{\lambda\phi}{4\pi\alpha}\cos\psi = \frac{r\lambda\phi}{4\pi B_\perp}\cos\psi\,, \tag{34}$$

which is identical to the expression for s_z (20). Therefore, tilting the elevation axis of the turntable has in essence created a synthetic baseline that is perpendicular to the look direction and that has a spatial extent of $r\alpha$.

3.3 The Effect of Correlation on Digital Height Map Fidelity

A primary determinant in accurately assessing the phase difference (ϕ) in an interferometric image is the correlation properties of the backscattered return. As will subsequently be shown, a lack of correlation, or "decorrelation," between the backscattered returns for two different observations leads to an increase in the standard deviation of measured phase difference values, ultimately resulting in uncertainty in the height measurements. As discussed in Section 2.1, the main factors contributing to decorrelation in general, and hence also to phase error, are signal-to-noise ratios ($\gamma_{thermal}$), physical changes in the target during the period of time between observations ($\gamma_{temporal}$), the number of looks used to reduce fading noise (speckle), alterations in the viewing geometry due to changes in the spatial location of the sensor between observations ($\gamma_{spatial}$), and resolution cell misregistration ($\gamma_{registration}$) [4], [11]. It was further shown that the total correlation (γ_{total}) between two observations is the product of these various correlation components.

Differentiation of the relative height equation derived for the folded compact range configuration (31) with respect to ϕ will (to first order) allow the error in the height measurement to be determined as a function of the uncertainty in the measured differential phase [4], [9], [10], [11]. This is understood by performing the differentiation

$$\frac{\partial h_t}{\partial \phi} = \frac{\lambda}{4\pi\alpha}\cos\psi \ , \tag{35}$$

and noting that $\frac{\partial h_t}{\partial \phi} \approx \frac{\sigma_{h_t}}{\sigma_\phi}$, where σ_{h_t} and σ_ϕ are respectively the standard deviations in height and phase, such that

$$\sigma_{h_t} = \frac{\lambda\cos\psi}{4\pi\alpha}\sigma_\phi \ . \tag{36}$$

This height error estimate assumes that no errors are added by the radar signal processor and that there is no decorrelation due to temporal effects [9], and is therefore a lower bound of the expected statistical error.

The expected phase standard deviation can be calculated as a function of the total correlation (γ_{total}) and the "number of looks" (N_L), where N_L refers to the number of pixels in the complex interferometric image that are spatially averaged in order to reduce the statistical variation (or noise) resulting from speckle. This phase noise has been determined by numerical simulation [3] and is plotted in Figure 12 for two, four, and eight looks. Figure 12 and equation (36) can thus be used in conjunction to estimate the expected height error for a given level of image correlation (γ_{total}).

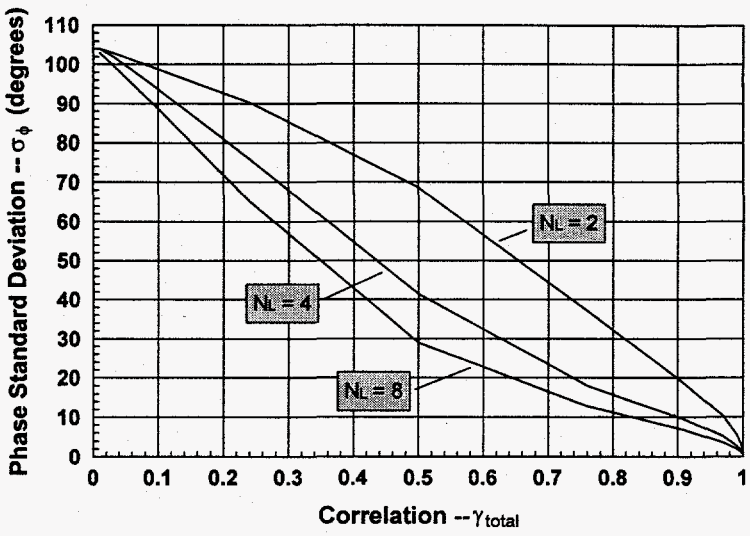

Figure 12. Uncertainty in interferometric phase estimation plotted as a function of correlation between two images for two, four, and eight looks.

It is clearly evident from Figure 12 that increasing the number of looks significantly reduces the phase noise. As the number of looks are increased, the phase standard deviation asymptotically approaches the Cramer-Rao bound, which is given by [10]

$$\sigma_{\phi_{Cramer-Rao}} = \frac{1}{\sqrt{2N_L}} \frac{\sqrt{\left(1-\gamma_{total}^2\right)}}{\gamma_{total}} \quad . \tag{37}$$

It may be inferred from the expression for σ_{h_t} (36) that height measurement sensitivity is increased by increasing the elevation offset angle α between the interferometric image pair (or in other words, by increasing the size of the synthetic baseline $B_\perp$). Conversely, the baseline correlation ($\gamma_{baseline}$) — and hence also γ_{total} — decreases as α is increased, resulting in an associated increase in the phase standard deviation σ_ϕ, as demonstrated in Figure 12. The implication is therefore that α must be carefully chosen to balance these two competing factors, such that there is sufficient phase sensitivity to height, but also a minimal introduction of phase error.

It is instructive to assume typical radar parameters, and use (36) and (37) to estimate the minimum height error that may be expected as a function of γ_{total}. This has been done for $\lambda = 0.025$ m, $\psi = 36°$, $N_L = 5$, and for three values of α; the results are plotted in Figure 13. This plot is enlightening, in that it not only indicates the minimum height errors which may be expected for the set of measurement parameters that have nominally been used in the folded compact range, but also clearly demonstrates the advantage of using the largest possible value of α.

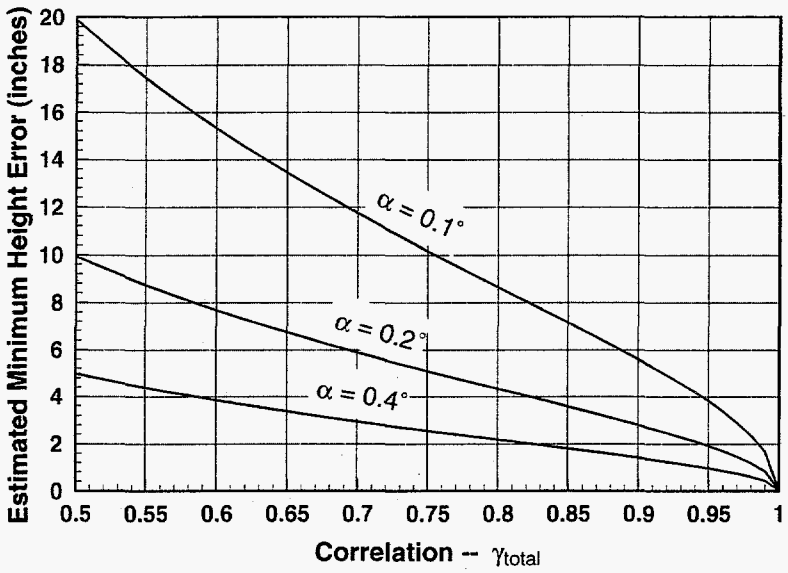

Figure 13. Estimated minimum height errors expected as a function of correlation between two images for the measurement parameters $\lambda = 0.025$ m, $\psi = 36°$, $N_L = 5$, and for three values of elevation offset angle (α).

3.4 Interferometric Measurement Results

Having derived an expression by which the relative height of objects may be determined, as well as having specified the parameters which define interferometric image quality, it is now possible to form and correctly interpret three-dimensional ISAR images of target samples positioned on the distributed target sample holder.

3.4.1 *Stacked Trihedral Interferometric Measurement*

The first set of results to be shown is an interferometric measurement of two trihedrals which are arranged in a vertical stack configuration (spaced apart from one another by low-density polystyrene blocks), having a vertical separation distance of approximately 3 feet. In this experiment, the bottom trihedral acts as a phase reference, such that the final interferometric image is expected to show the height differential between the two trihedrals. Trihedrals were chosen for this experiment due to the fact that their backscatter pattern has a broad main lobe in both the azimuth and elevation planes [28]; therefore, the backscattered returns can be expected to remain well-correlated over small changes in look angle resulting from variation of the elevation axis of the sample holder. A second reason for displaying these results is that, despite the fact that a trihedral is a simple canonical object, the stacked trihedral interferometric image highlights several of the complexities associated with forming digital height maps from SAR measurements.

In order to fully understand the final interferometric image, it is important to first view the two-dimensional ISAR image of the stacked trihedrals and the pre-registration correlation image shown respectively in Figures 14(a) and (b). The correlation image was created in

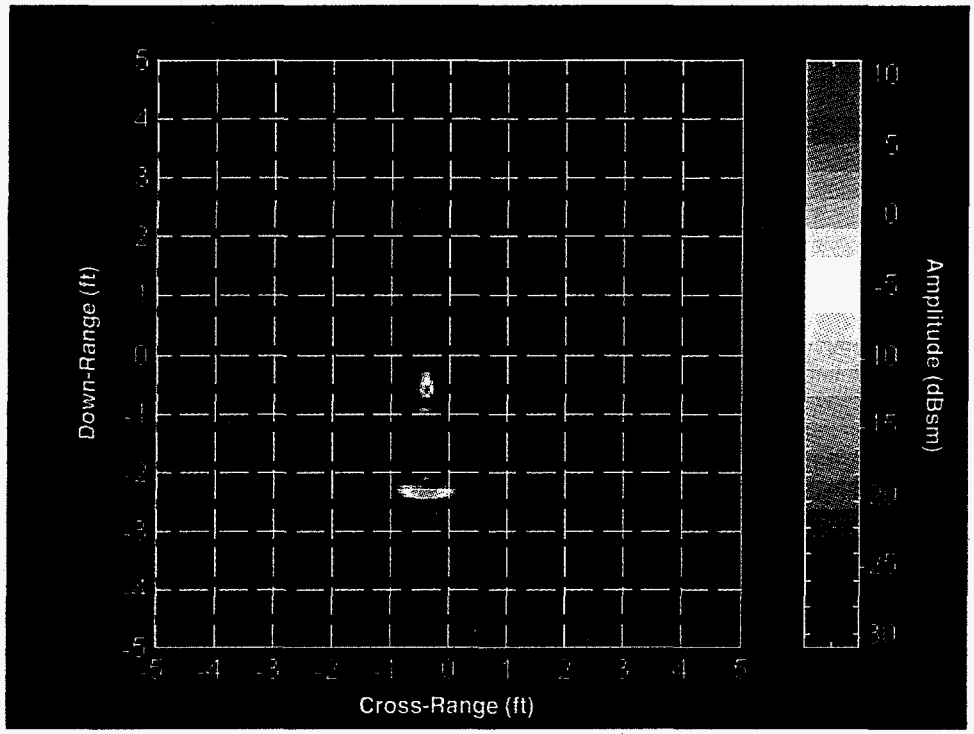

Figure 14(a). Two-dimensional ISAR image of stacked trihedrals.

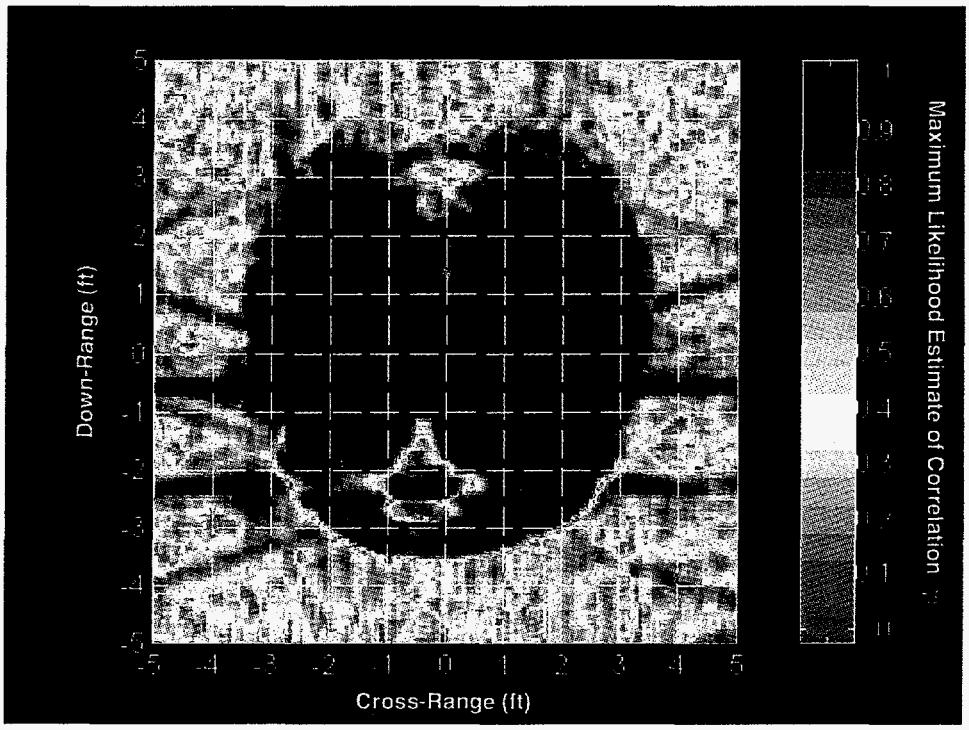

Figure 14(b). Pre-registration correlation image of stacked trihedrals for image pair having an elevation offset angle of $\alpha = 0.2°$.

precisely the same manner as described in Section 2.2, using the maximum likelihood estimate of correlation (3). The image pair used to form the correlation image resulted from (1) a measurement of the stacked trihedrals with the elevation axis of the sample holder set at its nominal 0° offset position, and (2) a second measurement of the stacked trihedrals, but with the elevation axis offset 0.2° from the first measurement position.

Several items of interest are visible in these images. Figure 14(a) reveals a "depth of focus" problem, in that the algorithm used in the ISAR image formation software has spread the backscattered return from the top trihedral in the azimuth dimension as compared with the properly focused return from the lower trihedral (located at the calibration position of the measurement configuration). The correlation image in Figure 14(b) indicates that the returns from the lower trihedral in the interferometric image pair are highly correlated. The backscattered returns from the top trihedral are also well-correlated within the defocused main lobe; however, the near-in sidelobes of the trihedral backscatter pattern are not well-correlated, causing a "halo" of decorrelation around the main lobe. Interestingly, the sidelobes appear to become correlated farther out from the main lobe, as evidenced by the "streaks" of correlation emanating from the central portion of the image. Finally, at the +3 foot down-range position on the correlation image is an area of decorrelation that is a result of this section of the sample holder being shadowed from the incident electromagnetic field by the top trihedral. Because the signal-to-noise ratio of the backscattered return is low in this section of the image due to a lack of incident signal, it appears as essentially a totally decorrelated area on the correlation image. Accordingly, this area of decorrelation in the image is very similar in shape to the top trihedral correlated backscatter pattern.

The interferometric images shown in Figures 15(a) and (b) have been generated by again applying the maximum likelihood estimate of correlation (3) to the stacked trihedral image pair (for which the differential elevation axis offset angle was $\alpha = 0.2°$), but using the detected phase information to form the interferometric image, as opposed to the magnitude information which was used to form the correlation image. As noted previously, a linear phase taper initially exists across the image that must be subtracted out in order to calculate the relative heights of objects in the image. Equation (31) is then used to determine the final height measurements.

Figure 15(a) is a digital height map of the stacked trihedrals, while Figure 15(b) is a rendered three-dimensional interferometric image. As expected, the digital height map displays the height differential between the two trihedrals. Based on an average correlation value of $\gamma_{total_{avg}} \cong 0.97$ for the main lobe of the correlated backscatter return, and using Figure 13, the minimum estimated height error for the stacked trihedral measurement is $\sigma_{h_i} = 1.4$ inches. Using an average of the displayed height values from the center portion of the trihedral main lobe return in the digital height map from Figure 15(a), the measured value of the stacked trihedral height differential is 3.4 feet, a difference of 13% from the expected value. It is evident, however, that the decorrelation caused by the trihedral sidelobes in the backscatter pattern adds additional uncertainty to the measurement which largely accounts for the decrease in the expected accuracy. The noise caused by these sidelobes is particularly

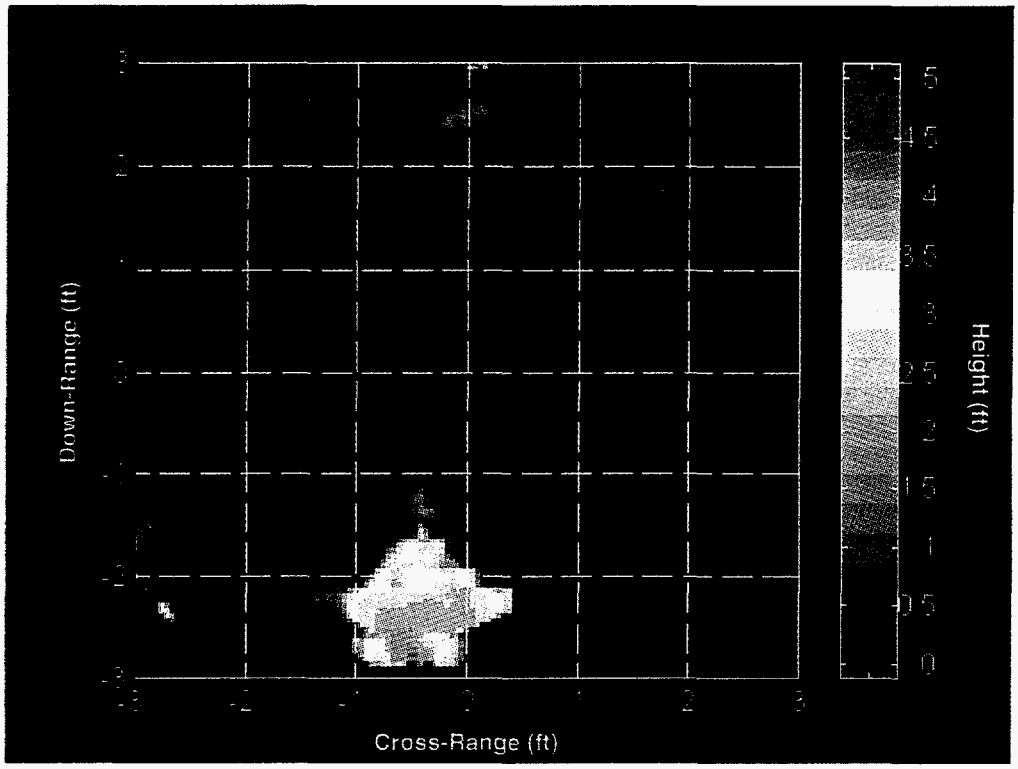

Figure 15(a). Digital height map of stacked trihedrals.

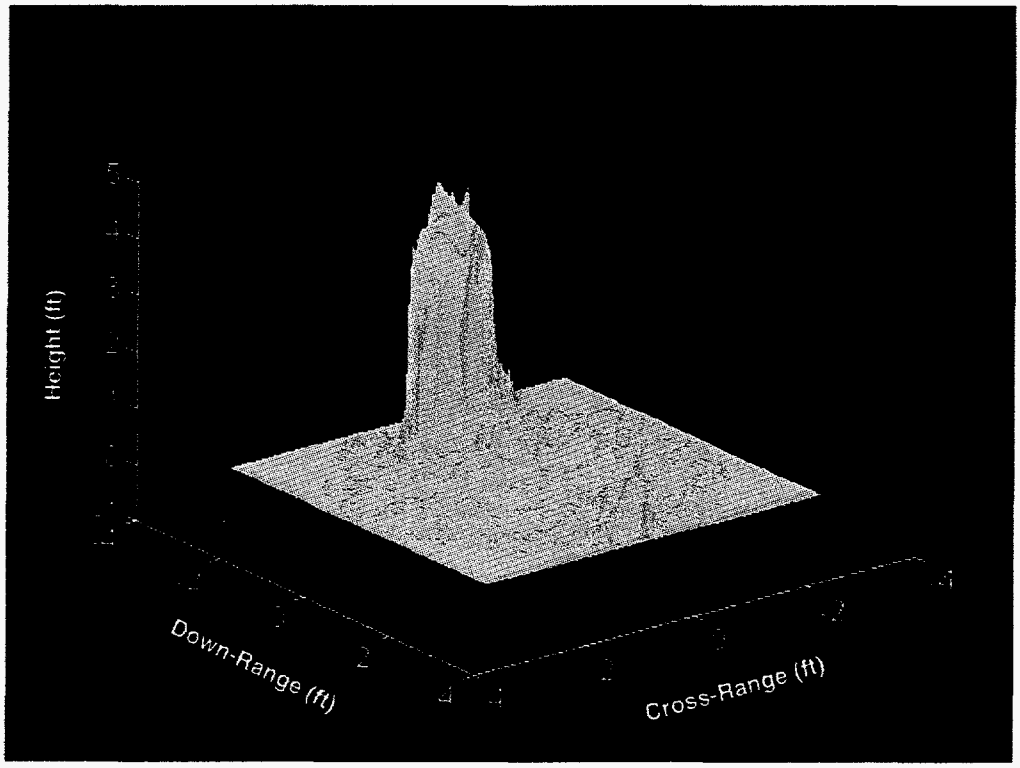

Figure 15(b). Rendered 3-dimensional image of stacked trihedrals.

evident in the rendered image, showing up as noise spikes around the periphery of the main lobe. Also of interest in the rendered image is the small noise peak at the +3 foot down-range position resulting from decorrelation due to shadowing, as explained above.

3.4.2 *Large Crushed Gravel Mesa Interferometric Measurement*

The second set of results to be displayed is an interferometric measurement of a "mesa" with an integrated "canyon," created from large crushed gravel. These results are intended to illustrate the limitations of the method, the high dependency of the accuracy of a digital height map on the degree of correlation of an interferometric image pair, and the advantage of synthesizing as large a baseline as possible (i.e., using the largest possible value for the elevation offset angle (α)).

Photographs of the crushed gravel mesa and canyon are shown in Figure 16(a) and (b). As seen in these photographs, the physical layout of the measurement sample is that the crushed gravel in the forward half of the sample holder is raked level with the edge of the sample holder; the gravel in the rear half of the sample holder is stacked in the shape of a gently sloping mesa, varying in height (relative to the level of the gravel in the forward half of the sample holder) from roughly 9 inches at the midsection of the sample holder, to ~ 7 inches at the back of the sample holder (farthest from the planar reflector). The transition region between the top of the mesa and the lower front section of gravel had a slope of approximately 68°. The "canyon" can be seen extending through the mesa from front to back, and had a depth of ~ 6 inches.

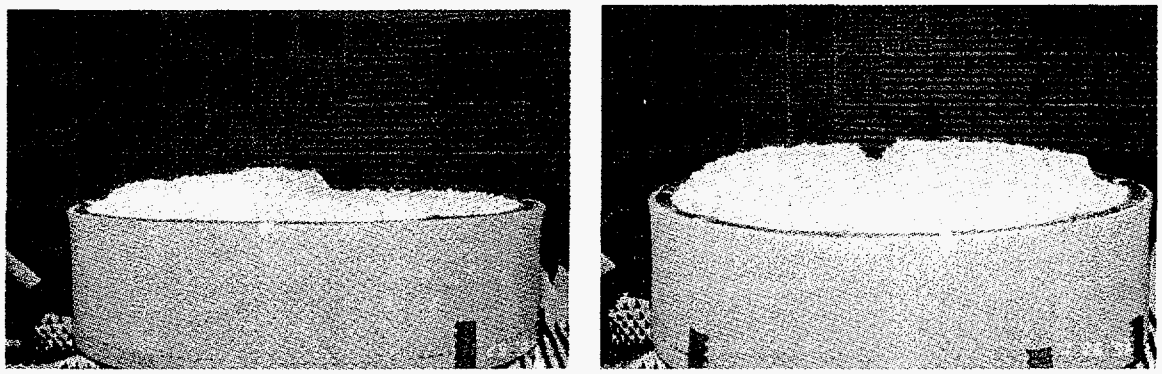

(a) (b)

Figure 16. Photographs of crushed gravel "mesa" and "canyon": (a) side view; (b) front view.

Again, in order to better understand the final digital height map, it is worthwhile to first view the pre-registration correlation image (Figure 17) of the gravel mesa and canyon. This image has been generated by correlating the pair of two-dimensional ISAR images resulting from (1) measurement of the mesa with the elevation axis of the sample holder set at its nominal 0° offset position, and (2) a second measurement of the mesa, but with the elevation axis offset 0.1° from the first measurement position.

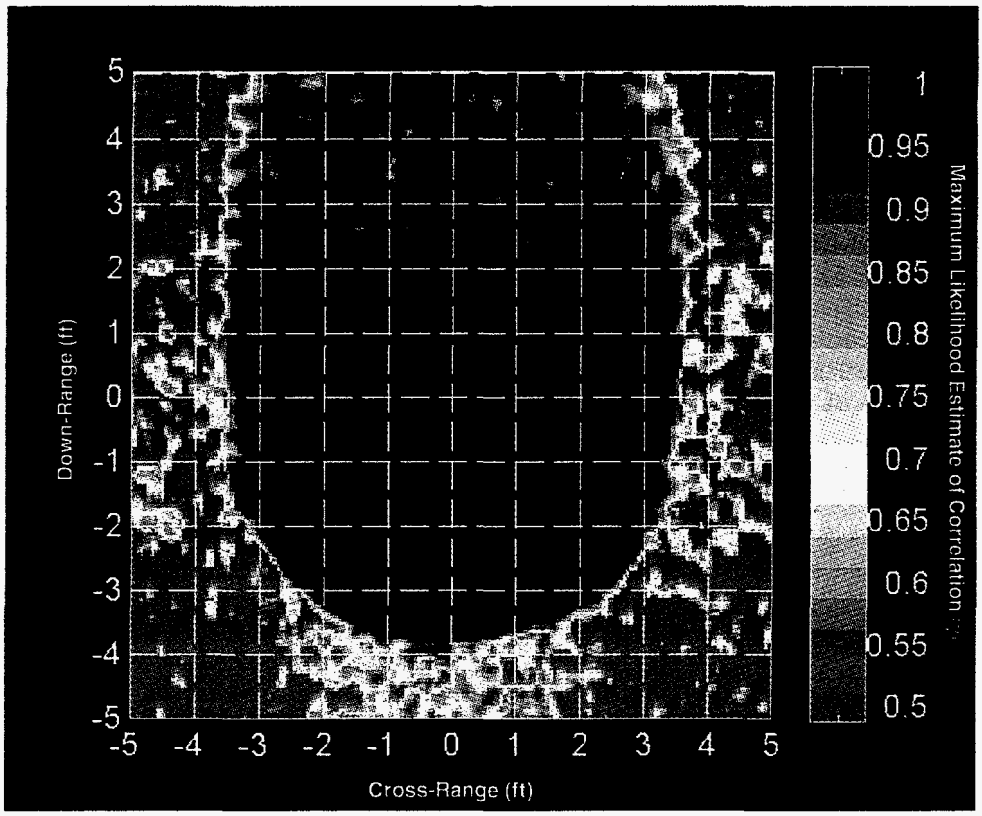

Figure 17. Pre-registration correlation image of crushed gravel "mesa" and "canyon" for image pair having an elevation offset angle of $\alpha = 0.1°$.

The CCD images of large crushed gravel displayed and discussed in Appendix A and Section 2 indicated that the phenomenon of "volumetric" scattering occurs from the gravel samples. That is, the wavelength of the field incident upon the gravel is such that some of the energy is coupled into the cavities created by the random orientation of the crushed gravel. Reflection and diffraction from the irregular surfaces and edges of the gravel cause the geometrical ray path traversed by the field coupled into these "cavities," and subsequently scattered back to the radar, to be substantially longer than direct scattering from the gravel. Thus, any slight reorientation of either the gravel sample or the direction of the incident field between measurements of the sample would cause a differential ray path to be traversed by the field coupled into the gravel "cavities." It is to be expected, then, that offsetting the elevation axis of the sample holder even slightly in order to form an interferometric image pair will result in detectable decorrelation in the final correlation image.

Such is in fact the case, as demonstrated by Figure 17. The decorrelation in the mesa and canyon areas of the gravel is clearly evident; somewhat surprising is the significantly higher level of correlation in the lower section of gravel. Based on an average correlation value of $\gamma_{total_{avg}} \cong 0.94$ for the mesa area, and using Figure 13, the minimum estimated height error for a digital height map of the crushed gravel mesa using this data is $\sigma_{h_t} = 4.2$ inches. Of significance is the observation that if this same average correlation value could have been achieved with an elevation axis offset angle of $\alpha = 0.2°$, the height error could have been cut

in half. Given the fact that $\sigma_{h_i} = 4.2$" is approximately 50% of the actual height of the sample, however, it is reasonable to assume that the caliber of the resulting digital height map will be suspect.

Figure 18(a) is the digital height map of the gravel mesa which has been generated using this data; Figure 18(b) is a rendered three-dimensional interferometric image of the mesa. As expected, the relatively high level of phase noise has produced a height map of dubious quality. Nevertheless, it is worthwhile to note that despite the high level of noise, the overall topography of the measurement sample is recognizably replicated in the rendered image, including the "canyon" and the transition between the mesa and the lower section of gravel. Perhaps of more interest is the fact that the noise spikes in the lower section of gravel have significantly lower amplitude levels than those in the mesa section of gravel, or in other words, the average height noise is less. This is of course a consequence of the higher level of correlation between the interferometric image pair for the lower section of gravel.

These results are meaningful, then, in that they clearly demonstrate that the accuracy of a digital height map is highly dependent on the degree of correlation of an interferometric image pair and the size of the interferometric "baseline" (elevation offset angle (α)). They further illustrate a limitation of using interferometry to create digital height maps--that is, surfaces exhibiting significant levels of volumetric scattering are not good candidates for achieving highly accurate digital height maps. This may be an impediment, for instance, in using high frequency radars for creating terrain maps of densely foliated regions.

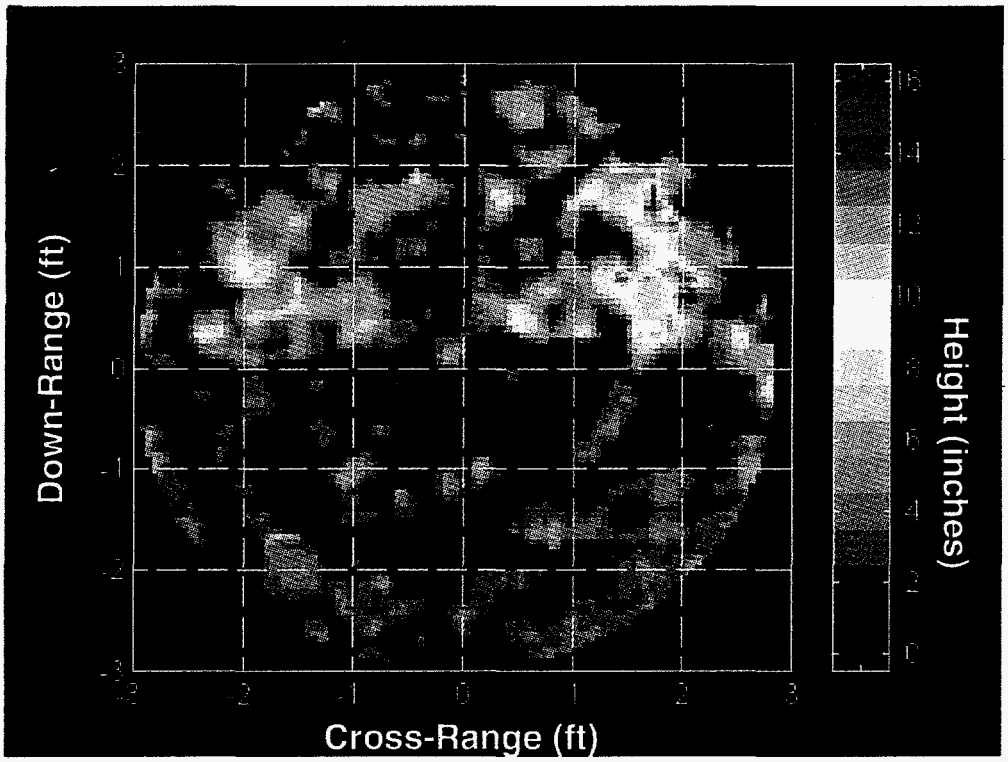

Figure 18(a). Digital height map of crushed gravel "mesa" and "canyon."

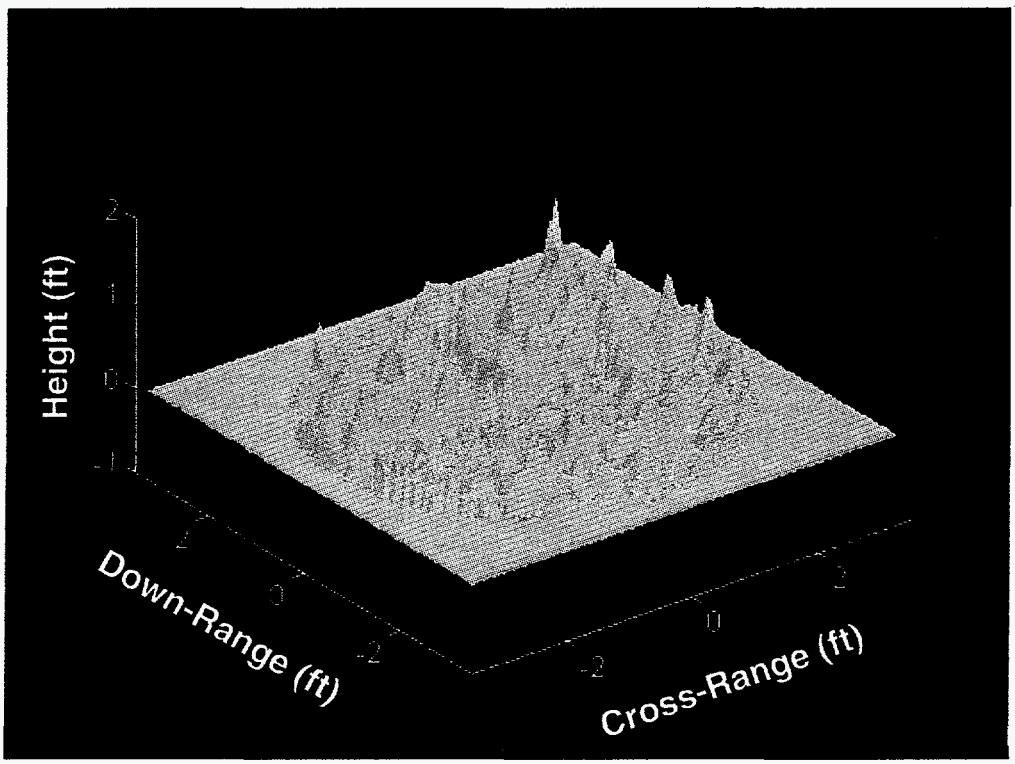

Figure 18(b). Rendered 3-dimensional image of crushed gravel "mesa" and "canyon."

3.4.3 *Sand Berm Interferometric Measurement*

The final set of results to be shown is an interferometric measurement of a sand berm created from moistened, fine-grained masonry sand. The berm was approximately 14 inches high and 12 inches wide, and spanned nearly the entire diameter of the sample holder (minus ~ 1.25' of clearance from the edge of the sample holder on either end of the berm). The berm was oriented to lie parallel to the compact range axis, and was truncated rather abruptly on all sides, except for the top leading edge (closest to the planar reflector), which had a slope of roughly 45°. Photographs of the berm are displayed in Figures 19(a) and (b). The objective here is simply to demonstrate the level of quality in digital height mapping results that can currently be obtained in the compact range for realistic distributed targets.

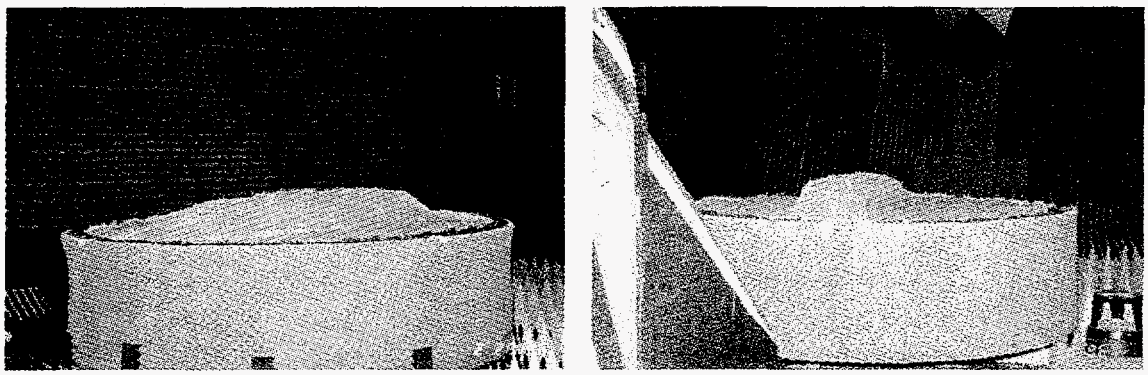

(a) (b)

Figure 19. Photographs of sand berm: (a) front view; (b) rear view.

The digital height map of the sand berm was generated by correlating the pair of two-dimensional ISAR images resulting from (1) measurement of the sand berm with the elevation axis of the sample holder set at its nominal 0° offset position, and (2) measurement of the sand berm with the elevation axis offset 0.1° from the first measurement position. An elevation axis offset angle of $\alpha = 0.1°$ was chosen to minimize the baseline decorrelation factor. The veracity of this choice was validated by measuring the average correlation coefficient for the pre-registration images. Over the center 2' x 2' section of the pre-registration correlation image, the mean correlation value was determined to be $\gamma_{total_{avg}} \cong 0.98$, demonstrating that in fact all contributors to decorrelation have been minimized to a large degree. Subsequently utilizing Figure 13, the minimum estimated height error for a digital height map of the sand berm using this data can thus be determined to be $\sigma_{h_t} \cong 2.4$ inches.

The digital height map and rendered three-dimensional interferometric image of the sand berm are displayed in Figures 20(a) and (b). The height map of Figure 20(a) shows that in the central portion of the sand berm, the average measured height is indeed approximately 14 inches, although the estimated 17% phase noise causes localized peaks and valleys, ranging in height in this area from about 12" to 17", with one small noise spike reaching as high as +20". The phase noise is better visualized in the rendered image of Figure 20(b), where its overall effect on image quality is readily apparent.

+20". The phase noise is better visualized in the rendered image of Figure 20(b), where its overall effect on image quality is readily apparent.

3.4.4 Summary

The three sets of interferometric measurements displayed in this section have clearly demonstrated the ability to form three-dimensional images of targets using the folded compact range. The interferometric baseline necessary to create these images was synthesized by offsetting the elevation axis of the sample holder between measurements of the target, thus simulating a "two-pass" IFSAR measurement scenario.

The level of phase noise in the digital height maps, although small in absolute terms, was significant in relation to the actual height of the targets, and principally resulted from the necessity of using a small value of angular offset (i.e., a small baseline) to minimize the associated spatial decorrelation. As described earlier, greater than expected decorrelation is present in the correlation imagery due to processing artifacts, (e.g., polar reformatting of the data by the system software prior to registration of the complex images). It is felt, however, that correction of this deficiency in the image processing software will alleviate this problem, leading to the ability to utilize larger synthesized baselines, and ultimately resulting in reduced phase noise and greater height sensitivity in the interferometric images.

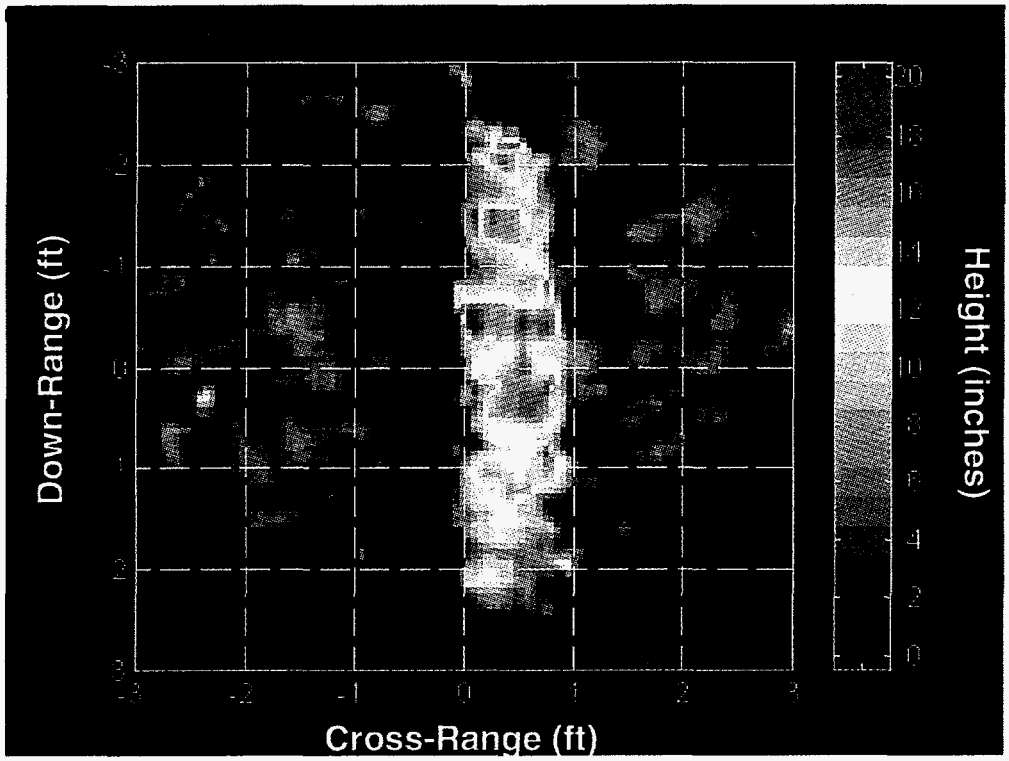

Figure 20(a). Digital height map of sand berm.

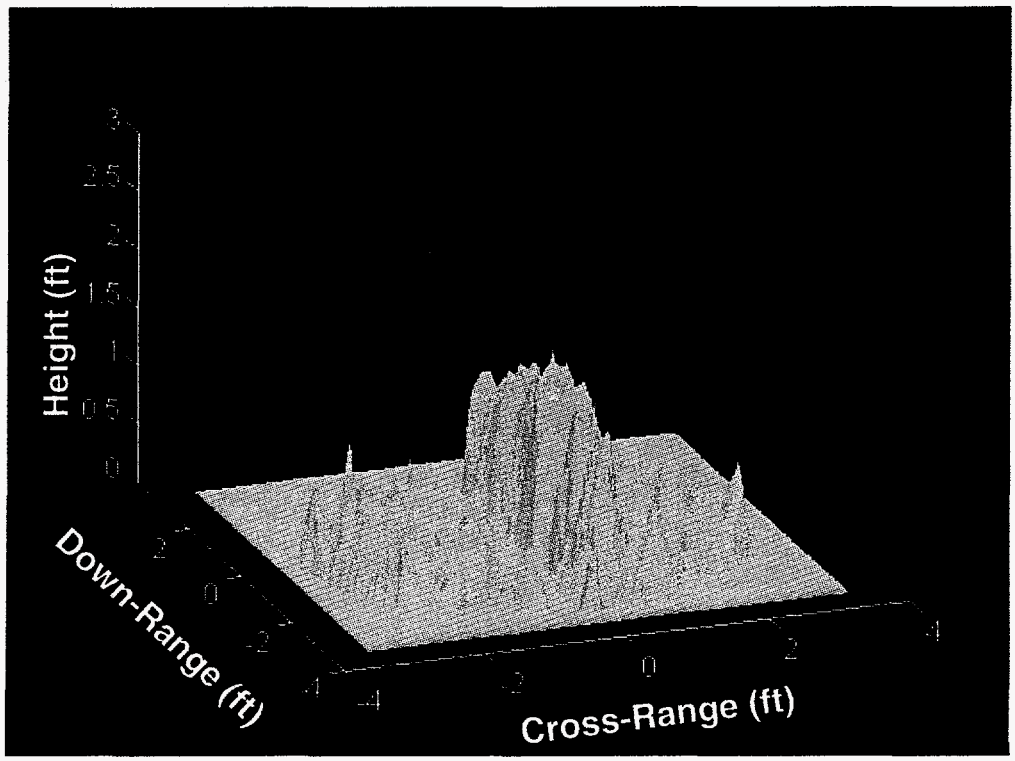

Figure 20(b). Rendered 3-dimensional image of sand berm.

4. EXTENDED USES OF THE FOLDED COMPACT RANGE

The measurements which have been made thus far in the folded compact range have essentially replicated (although with nearly an order of magnitude increase in resolution capabilities in most instances) the abilities of currently fielded interferometric SAR measurement systems, such as the airborne and spaceborne platforms referenced earlier. The folded compact range measurement system does, however (as has been discussed), possess the unique advantage in relation to these fielded systems of being able to control, study, and assess the environmental variables contributing to IFSAR and CCD image quality.

It should also be recognized that the folded compact range is now in a position to be utilized as a measurement tool to explore additional research areas beyond those in which fielded SAR measurement systems have typically been employed. As an example, the IFISAR capability of the folded compact range would serve as an ideal testbed for demonstrating the potential usefulness of an interferometric radar in detecting possible activity at an observation site when coherent change detection might be unusable, due to nearly complete temporal decorrelation of a set of pre- and post-disturbance image pairs (due to heavy activity at the area, environmental factors, etc.).

As a second example of its potential utility, the folded compact range could be used to perform "multi-baseline" interferometric experiments. The use of a single baseline (elevation axis offset angle) to create an image pair from which interferometric (and hence, height) information can be extracted was discussed and demonstrated in detail in the previous section. However, the parameters of the measurement setup and data collection algorithm could easily be extended to image the target sample over a multiplicity of offset angles (or multiple baselines). This would allow a true 3-dimensional image of the target scene to be created by essentially processing the data with a 3-d Fourier transform.

A final example of a potential additional use of the folded compact range is the current interest in the imaging of buried targets, and in particular, shallowly buried mines [29]. Again, due to its tightly controlled environment, the folded compact range is an ideal testbed for investigating the use of electromagnetic fields, and particularly, an "ultra-wideband" SAR, as a means of remotely detecting and imaging subsurface targets. In order to support this postulation, a preliminary image of a cylindrical pipe buried in dry sand has been made using the folded compact range measurement configuration.

A few of the pertinent measurement parameters were as follows:

- swept frequency waveform bandwidth: 8 GHz;
- center frequency: 12 GHz;
- polarization (tx/rx): horizontal;
- cylinder diameter: 0.75 inches;
- cylinder length: 54.4 inches;
- cylinder burial depth in sand: ~ 5 inches.

Perhaps the most notable radar parameter given above is the relatively high center frequency at which the imaging was conducted (12 GHz). As was shown in Section 2.2.2, the skin depth for dry sand at this frequency is approximately 1.4 m; thus, despite the relatively high frequency, a significant portion of the incident field should reach the cylinder (buried at a depth of 5 inches), and scattering from the cylinder should be detectable. Photographs of the target sample holder before and after burial of the pipe are shown in Figures 21(a) and (b).

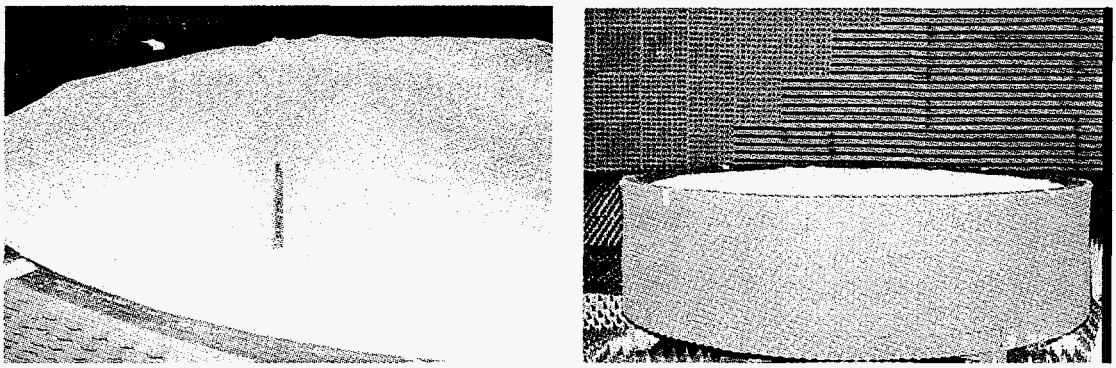

(a) (b)

Figure 21. Photographs of buried cylindrical pipe in dry sand: (a) burial depth is five inches; (b) view of sample holder containing buried pipe.

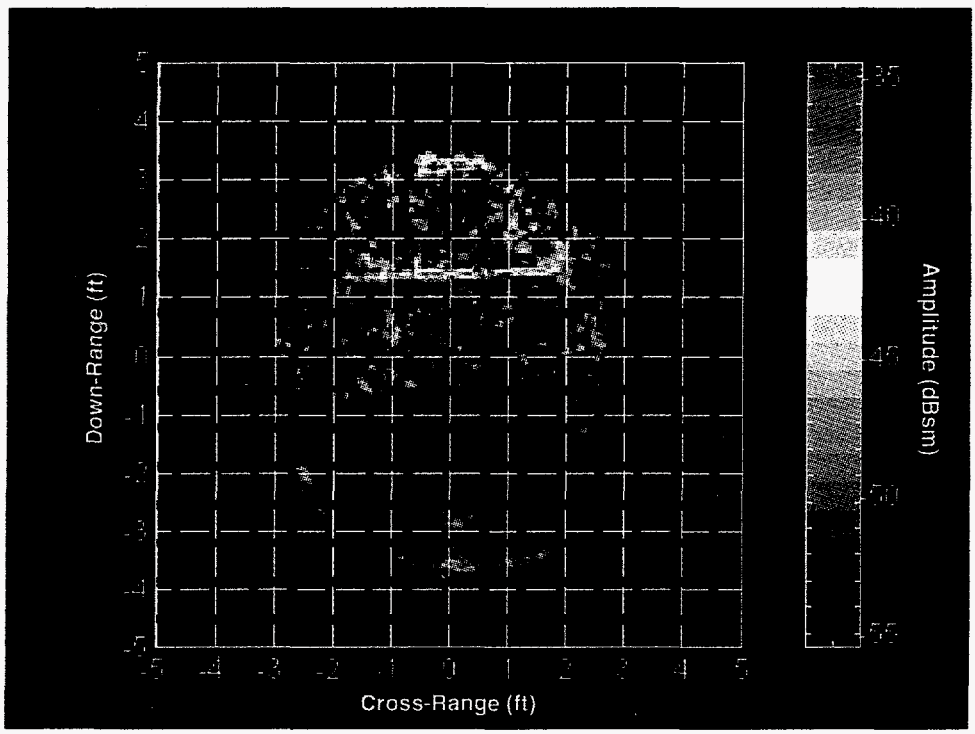

Figure 22. Two-dimensional ISAR image of sand with buried cylinder.

A two-dimensional image of the backscattered return from the sand with the embedded cylinder is shown in Figure 22. The outline of the buried cylinder is clearly visible between the +1- and +2-foot down-range grid marks in this ISAR image, although it is obscured to some degree by scattering from the surface of the sand.

While this measurement has arguably been conducted using perhaps the most "benign" soil conditions imaginable, it does indicate that imaging of shallowly buried targets can successfully be accomplished for certain soil conditions even at relatively high frequencies, and more importantly, that the folded compact range is well-suited for performing experimental investigations of this nature.

5. CONCLUSION

This report is a sequel to a previous report [1] which described both the development of the SNL folded compact range, and an initial set of coherent-change-detection measurements that were made with the system. This report has described follow-on CCD measurements of other distributed target samples, and additionally has characterized the theoretical and practical aspects of performing interferometric inverse-synthetic-aperture-radar (IFISAR) measurements in the folded compact range environment.

The CCD measurements performed in the folded compact range are highly sensitive, permitting perturbations to distributed targets on the order of fractions of a wavelength to be detected. The IFISAR measurements, in addition to the two-dimensional spatial resolution afforded by typical ISAR processing, provide resolution of the relative heights of targets with accuracies that can approach a wavelength. Several examples were given of digital height maps that have been generated from measurements performed at the folded compact range facility.

It is well-noted that there currently exist numerous fielded, operational SAR systems having the capability to perform both coherent change detection (CCD) and interferometric (IFSAR) measurements. However, the folded compact range is unique in relation to these systems in its ability to control to a much greater extent the physical phenomena contributing to the decorrelation of a pair of complex SAR images. The folded compact range is thus an extremely useful tool in isolating and independently investigating the various decorrelation sources which ultimately affect the final CCD or interferometric image quality.

This concept was illustrated in this report by the ability to quantitatively investigate the sensitivity of the CCD measurement process to alterations in the orientation geometry during data collection (that is, changes in the relative spatial location of the SAR sensor between observations of the target), while keeping the distributed target sample and measurement environment undisturbed. The utility of using the folded compact range to quantify the deleterious effects of decorrelation on digital height mapping accuracy also became readily apparent.

In conclusion, the folded compact range CCD and IFISAR measurements have been quite successful, and have demonstrated not only the viability of the folded compact range concept in simulating SAR CCD and interferometric SAR (IFSAR) measurements, but also its usefulness as a tool in the research and development of SAR CCD and IFSAR image generation and measurement methodologies.

REFERENCES

[1] K. W. Sorensen, *Folded Compact Range Development and Coherent Change Detection Measurement Project*, SNL Report, SAND95-0389, March 1995.

[2] D. L. Mensa, *High Resolution Radar Cross-Section Imaging*, Artech House, Norwood, MA, 1991.

[3] D. L. Bickel and W. H. Hensley, *Design, Theory, and Applications of Interferometric Synthetic Aperture Radar for Topographic Mapping*, SNL Report, SAND96-1092, May 1996.

[4] H. A. Zebker and J. Villasenor, "Decorrelation in Interferometric Radar Echoes," *IEEE Transactions on Geoscience and Remote Sensing*, vol. 30, no. 5, Sept. 1992, pp. 950-959.

[5] J. P. Burg, et. al., "Estimation of Structured Covariance Matrices," *Proceedings of the IEEE*, vol. 70, no. 9, September 1982, pp. 963-974.

[6] P. H. Eichel, et. al., "Interferometric Processing of Coherent Spotlight Mode SAR Images," *Proceedings of the Interferometric SAR Technology and Applications Symposium*, April 13-14, 1993, Ft. Belvoir, VA, pp. 253-274.

[7] C. A. Balanis, *Advanced Engineering Electromagnetics*, John Wiley & Sons, Inc., New York, 1989.

[8] R. F. Harrington, *Time-Harmonic Electromagnetic Fields*, McGraw-Hill Book Company, New York, 1961.

[9] H. A. Zebker, et. al., "Accuracy of Topographic Maps Derived from ERS-1 Interferometric Radar," *IEEE Transactions on Geoscience and Remote Sensing*, vol. 32, no. 4, July 1994, pp. 823-836.

[10] E. Rodriguez and J. M. Martin, "Theory and Design of Interferometric Synthetic Aperture Radars," *IEE Proceedings-F*, vol. 139, no.2, April 1992 pp. 147-159.

[11] F. K. Li and R. M. Goldstein, "Studies of Multibaseline Spaceborne Interferometric Synthetic Aperture Radars," *IEEE Transactions on Geoscience and Remote Sensing*, vol. 28, no. 1, Jan. 1990, pp. 88-97.

[12] J. C. Dainty, ed., *Laser Speckle and Related Phenomena*, Springer-Verlag, Berlin, 1984.

[13] L. M. H. Ulander and P. O. Frolind, "Ultra-Wideband and Low-Frequency SAR Interferometry," IGARSS '96 Conference Proceedings, Lincoln, Nebraska, May 27-31, 1996.

[14] A. K. Gabriel and R. M. Goldstein, "Crossed Orbit Interferometry: Theory and Experimental Results From SIR-B," *International Journal of Remote Sensing*, vol. 9, no. 5, 1988, pp. 857-872.

[15] Q. Lin, et. al., "New Approaches in Interferometric SAR Data Processing," *IEEE Transactions on Geoscience and Remote Sensing*, vol. 30, no. 3, May 1992 pp. 560-567.

[16] P. H. Eichel, et. al., *Spotlight SAR Interferometry for Terrain Elevation Mapping and Interferometric Change Detection,* SNL Report, SAND93-2072, Feb. 1996.

[17] D. R. Wehner, *High Resolution Radar*, Artech House, Norwood, MA, 1987.

[18] M. I. Skolnik, *Introduction to Radar Systems*, 2nd Edition, McGraw-Hill Book Company, New York, 1980.

[19] L. C. Graham, "Synthetic Interferometer Radar for Topographic Mapping," *Proceedings of the IEEE*, vol. 62, no. 6, June, 1974, pp. 763-768.

[20] H. A. Zebker and R. M. Goldstein, "Topographic Mapping From Interferometric Synthetic Aperture Radar Observations," *Journal of Geophysical Research*, vol. 91, no. B5, April 1986, pp. 4993-4999.

[21] J. O. Hagberg and L. M. H. Ulander, "On the Optimization of Interferometric SAR for Topographic Mapping," *IEEE Transactions on Geoscience and Remote Sensing*, vol. 31, no. 1, Jan. 1993, pp. 560-567.

[22] S. N. Madsen, et. al., "Topographic Mapping Using Radar Interferometry: Processing Techniques", *IEEE Transactions on Geoscience and Remote Sensing*, vol. 31, no. 1, Jan. 1993, pp. 246-256.

[23] R. M. Goldstein, et. al., "Satellite Radar Interferometry: Two-Dimensional Phase Unwrapping," *Radio Science*, vol. 23, no. 4, July-August 1988, pp. 713-720.

[24] E. J. M. Rignot and J. J. van Zyl, "Change Detection Techniques for ERS-1 SAR Data," *IEEE Transactions on Geoscience and Remote Sensing*, vol. 31, no. 4, July 1993, pp. 896-906.

[25] A. L. Gray, and P. J. Farris-Manning, "Repeat-Pass Interferometry with Airborne Synthetic Aperture Radar," *IEEE Transactions on Geoscience and Remote Sensing*, vol. 31, no. 1, Jan. 1993, pp. 180-191.

[26] J. D. O'Brien, "Atmospheric Effects on Repeat-Pass SAR Interferometry," *SPIE*, vol. 2471, pp. 316-323.

[27] N. L. VandenBerg and D. R. Sheen, "The P-3 Ultra-Wideband SAR: Two-Pass Interferometry," AMEREM '96 Conference Abstracts, May 27-31, 1996, p. 36.

[28] N. C. Currie, ed., *Radar Reflectivity Measurement: Techniques & Applications*, Artech House, Norwood, MA, 1989.

[29] AMEREM '96 International Conference on "The World of Electromagnetics," held in Albuquerque, NM, May 27-31, 1996.

APPENDIX A

Coherent Change Detection Images of Large Crushed Gravel

Intentionally Left Blank

SNL Folded Compact Range

Figure A-1

Comparative Sizes of Crushed Gravel and Pea Gravel

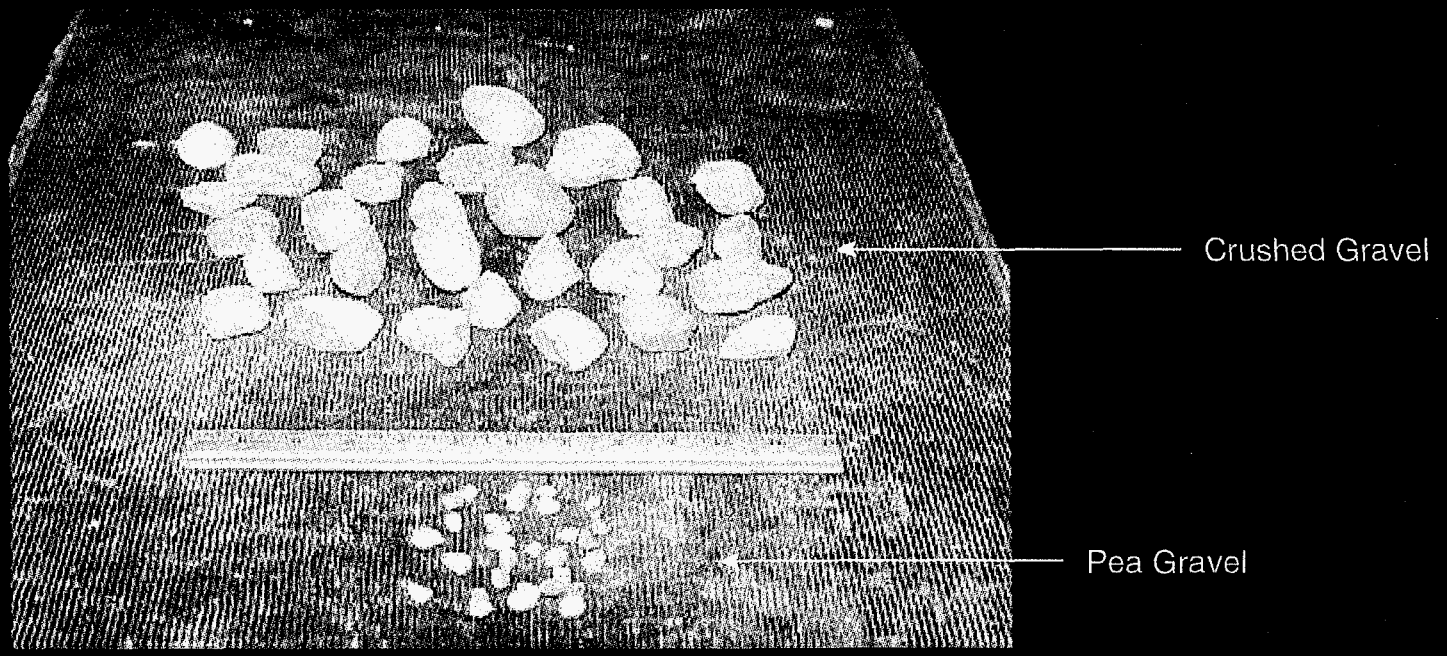

Figure A-2

2-D ISAR Image of Large Crushed Gravel (Null Set)

Azimuth Rotation

- File: WE3H
- Chirp BW: 8 GHz
- Center Freq.: 12 GHz
- Pol.:HH
- X Weighting: Hamming
- Y Weighting: Hamming
- Image Resolution: 1.1 in.
- Processing Method: None

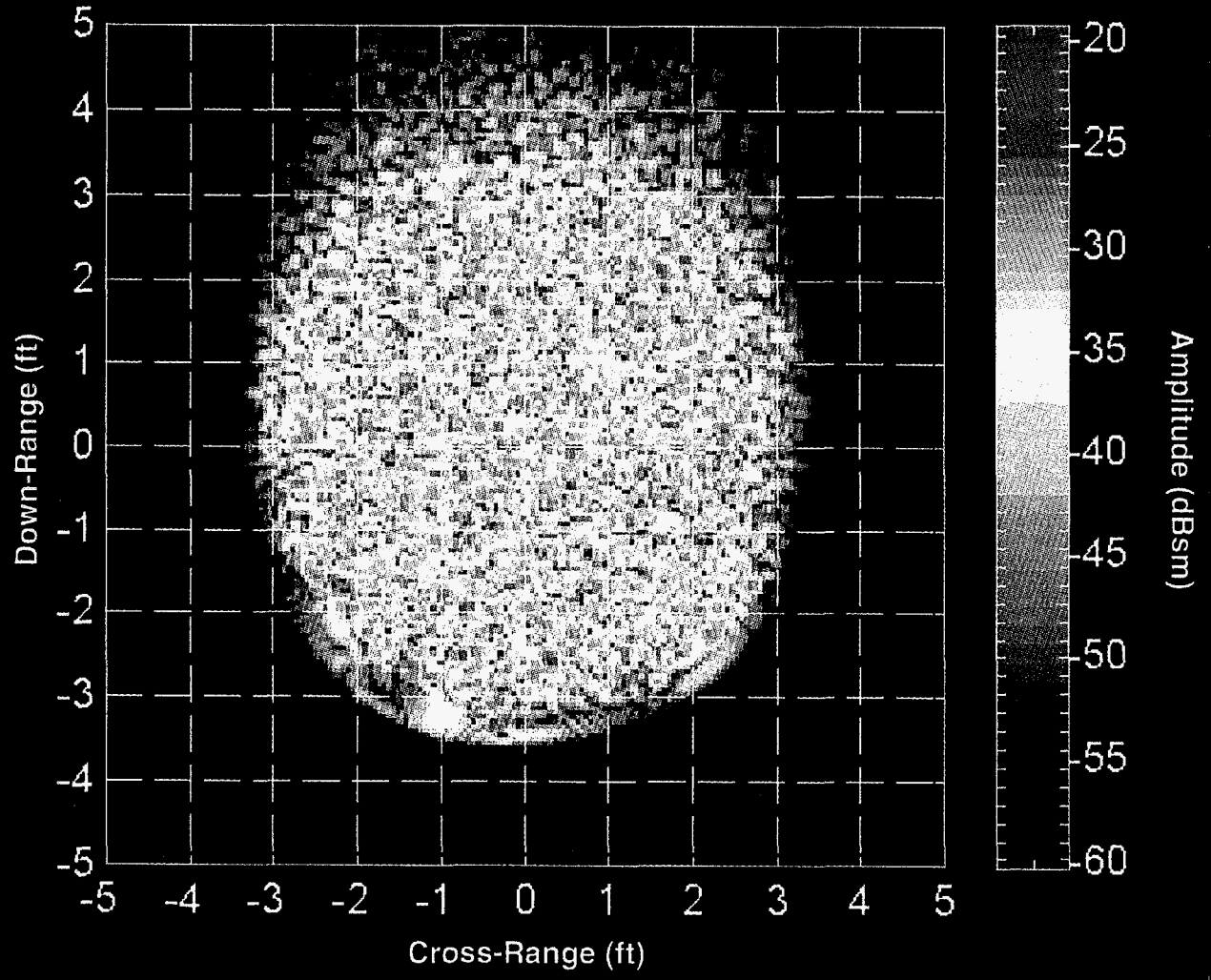

Figure A-3

Retraced Footsteps

(Large Gravel)

Azimuth Rotation

- File: WE3H
- Chirp BW: 8 GHz
- Center Freq.: 12 GHz
- Pol.:HH
- X Weighting: Hamming
- Y Weighting: Hamming
- Image Resolution: 1.1 in.
- Processing Method: Correlation Algorithm
- Number of Samples: 5

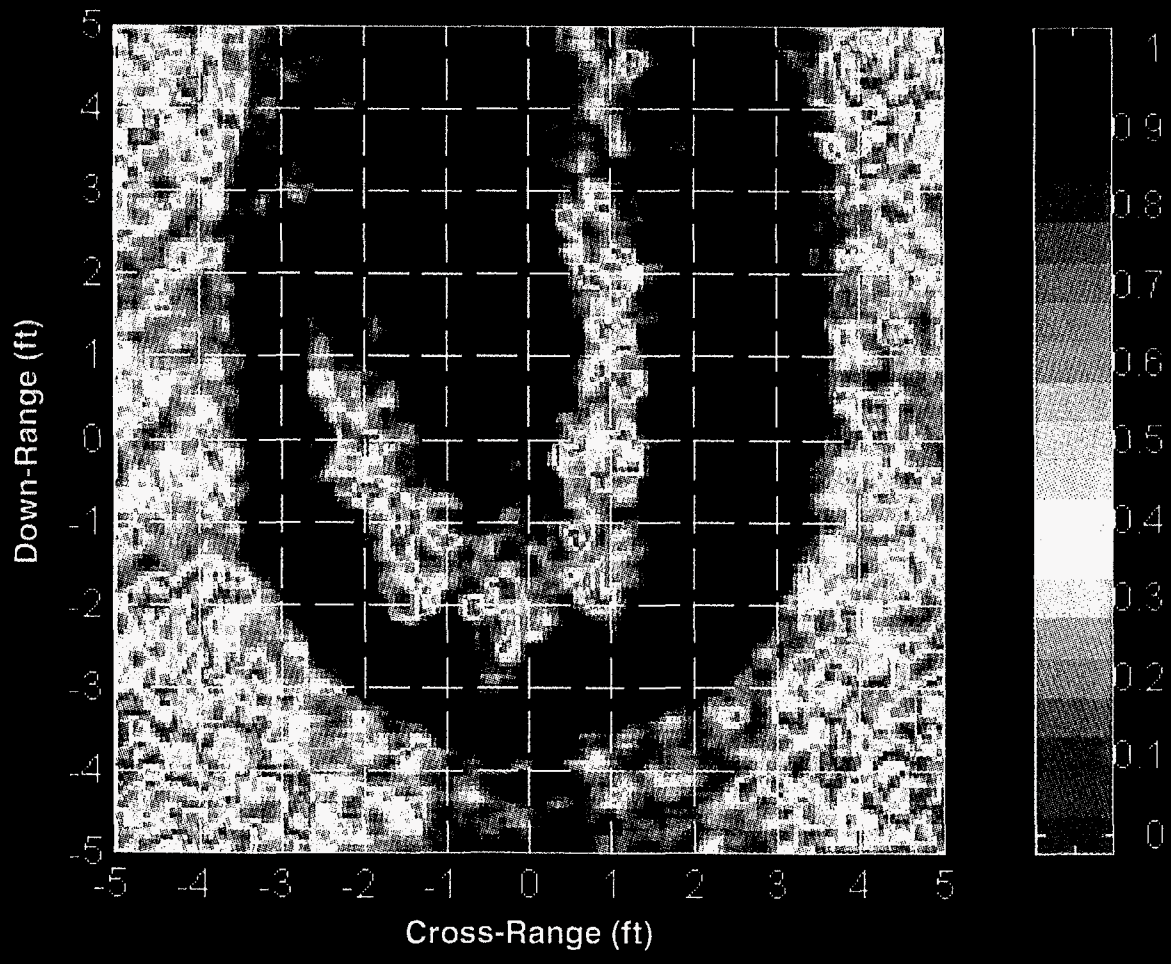

Figure A-4

Discrete Footsteps

(Large Gravel)

Azimuth Rotation

- File: WE2H
- Chirp BW: 8 GHz
- Center Freq.: 12 GHz
- Pol.:HH
- X Weighting: Hamming
- Y Weighting: Hamming
- Image Resolution: 1.1 in.
- Processing Method: Correlation Algorithm
- Number of Samples: 5

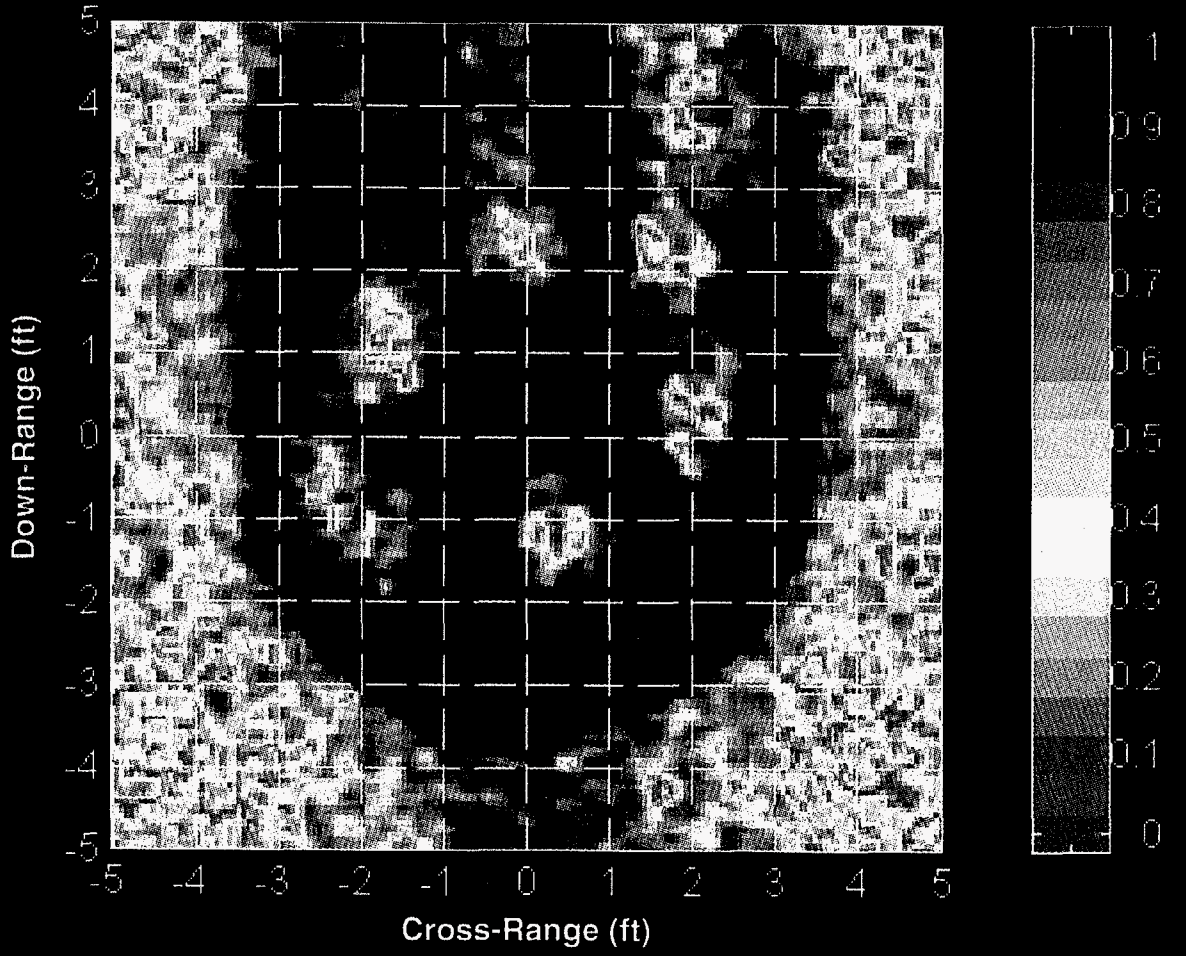

Figure A-5

Light Raking
(Large Gravel)

Azimuth Rotation

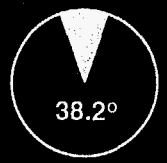

- File: RK1H
- Chirp BW: 8 GHz
- Center Freq.: 12 GHz
- Pol.:HH
- X Weighting: Hamming
- Y Weighting: Hamming
- Image Resolution: 1.1 in.
- Processing Method: Correlation Algorithm
- Number of Samples: 5

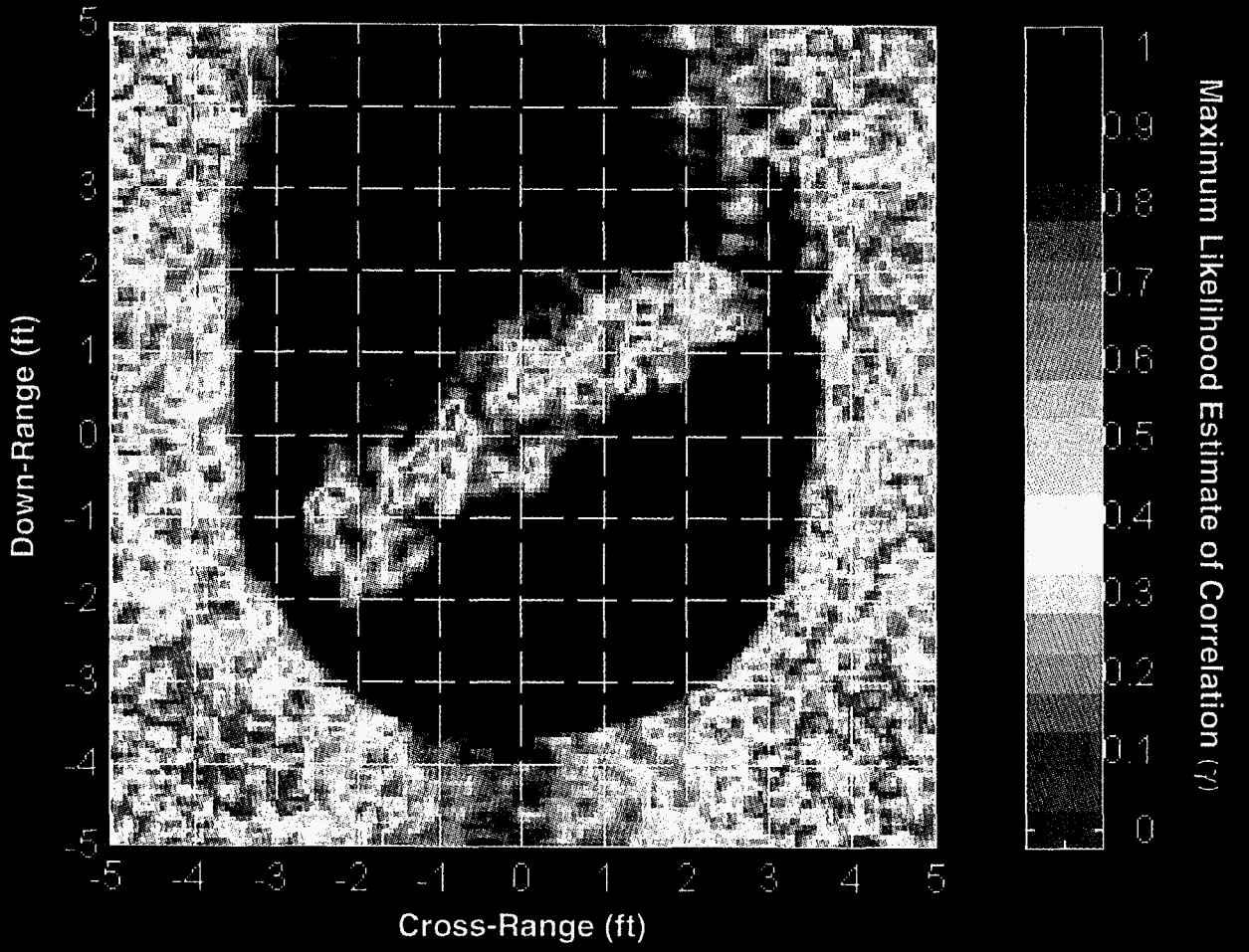

Figure A-6

Medium Raking
(Large Gravel)

Azimuth Rotation

- File: RK2H
- Chirp BW: 8 GHz
- Center Freq.: 12 GHz
- Pol.:HH
- X Weighting: Hamming
- Y Weighting: Hamming
- Image Resolution: 1.1 in.
- Processing Method: Correlation Algorithm
- Number of Samples: 5

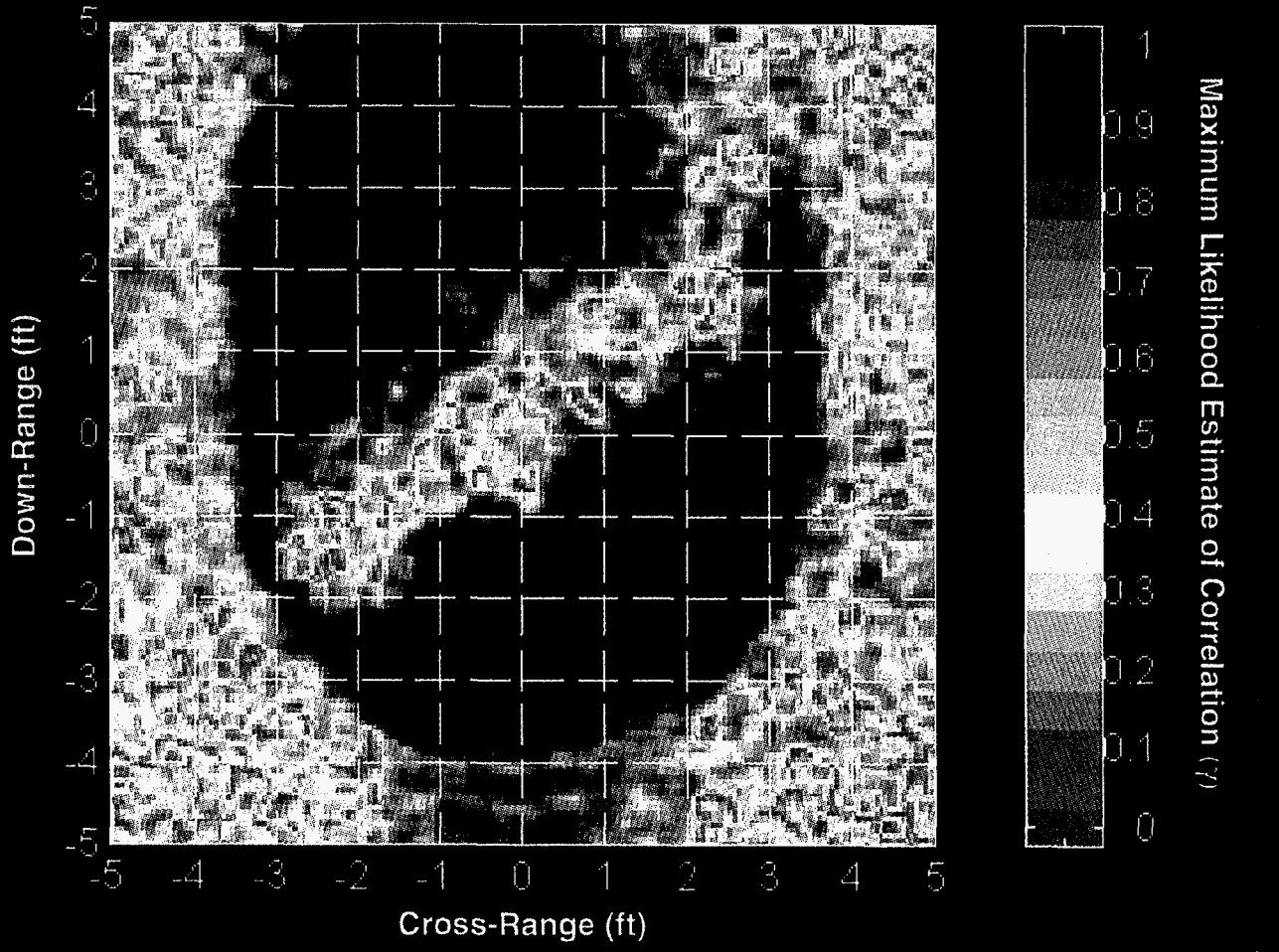

Figure A-7

Discrete Rock Removal
(Large Gravel)

Azimuth Rotation

- File: PL8H
- Chirp BW: 8 GHz
- Center Freq.: 12 GHz
- Pol.:HH
- X Weighting: Hamming
- Y Weighting: Hamming
- Image Resolution: 1.1 in.
- Processing Method: Correlation Algorithm
- Number of Samples: 5

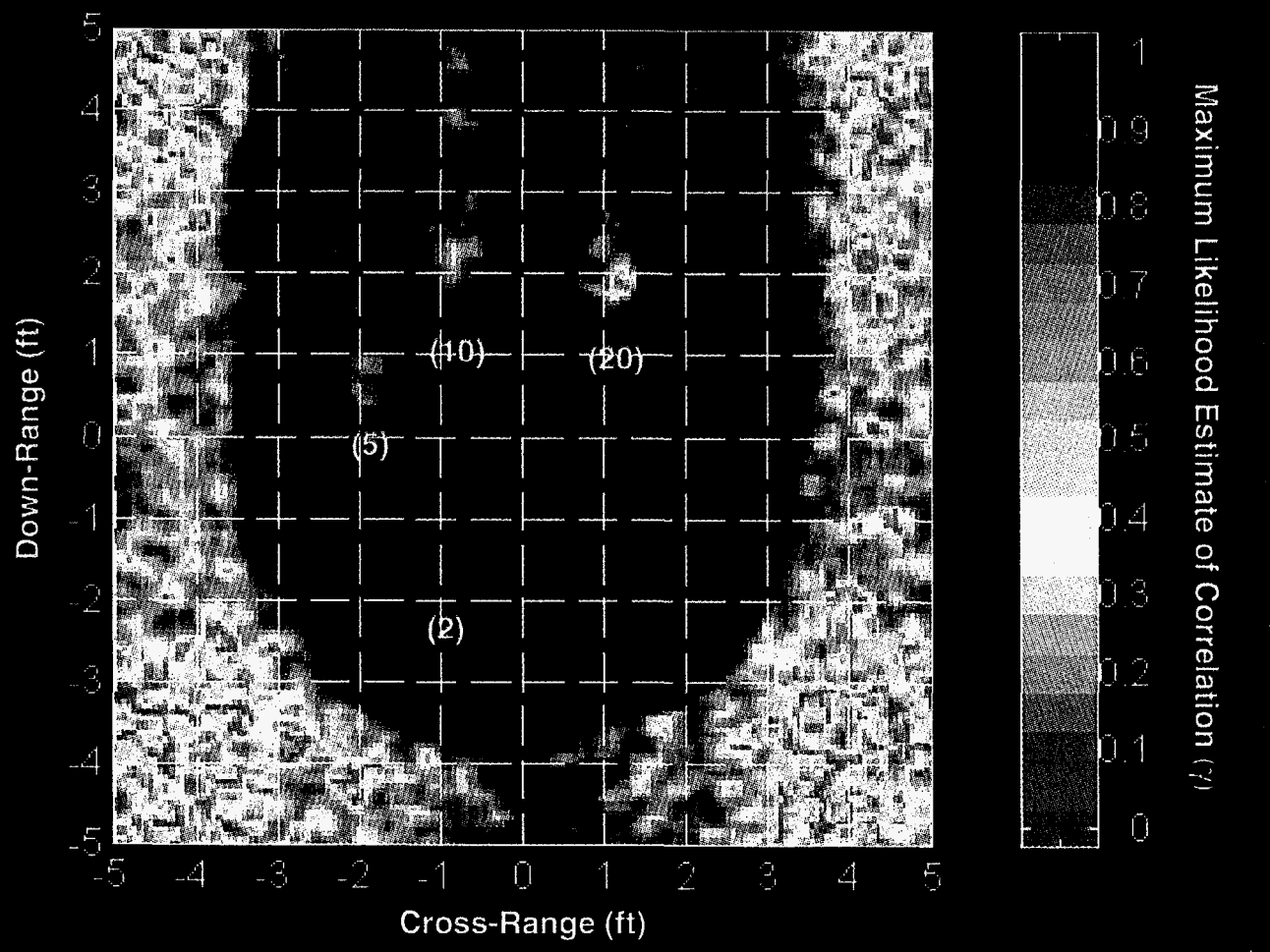

Figure A-8

Tire Tracks

(Large Dusty Gravel)

Azimuth Rotation

- File: WT1H
- Chirp BW: 8 GHz
- Center Freq.: 12 GHz
- Pol.:HH
- X Weighting: Hamming
- Y Weighting: Hamming
- Image Resolution: 1.1 in.
- Processing Method: Correlation Algorithm
- Number of Samples: 5

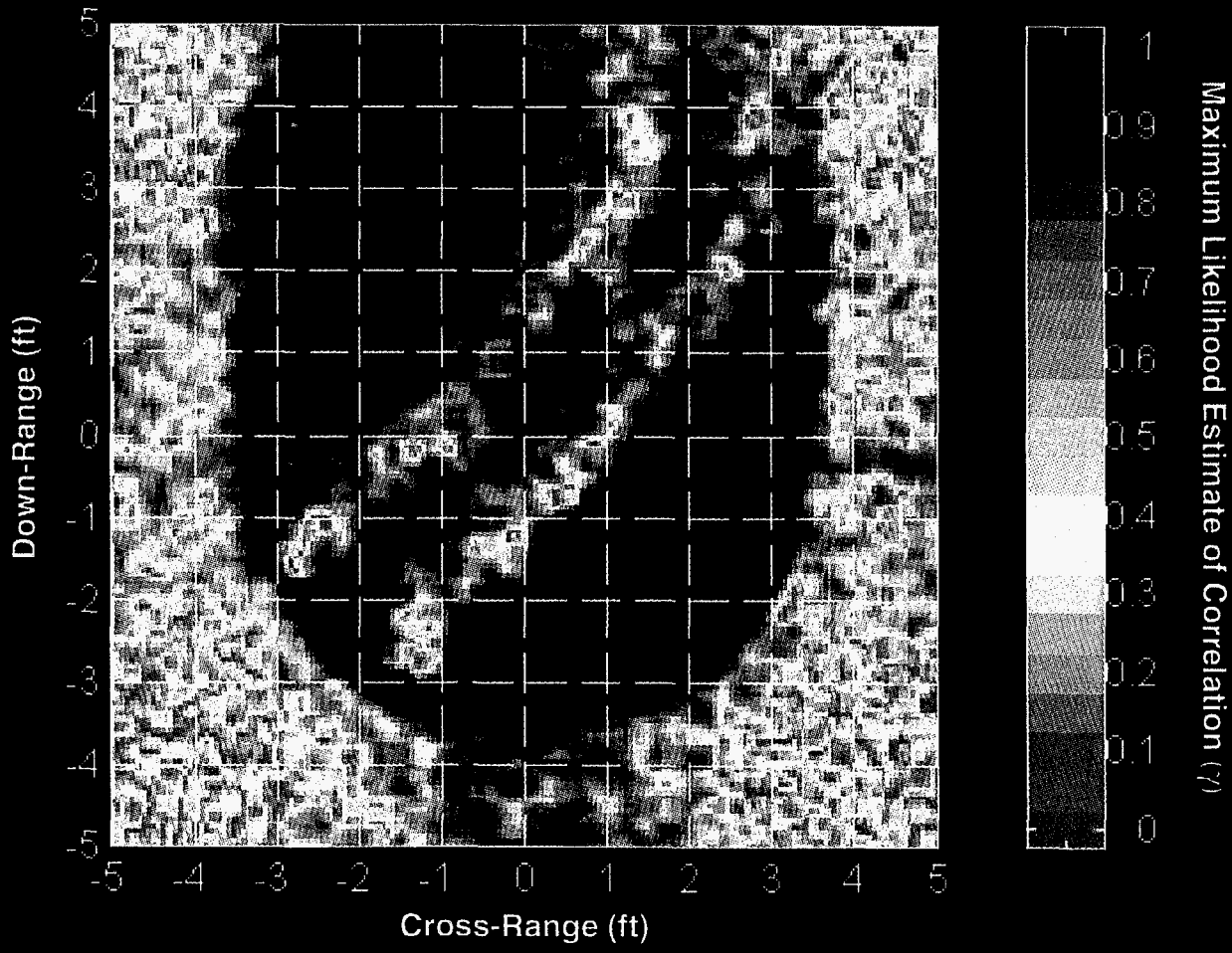

Figure A-9

Tire Tracks

--Wet (t=0 hrs)

(Large Dusty Gravel)

Azimuth Rotation

- File: WT2H
- Chirp BW: 8 GHz
- Center Freq.: 12 GHz
- Pol.:HH
- X Weighting: Hamming
- Y Weighting: Hamming
- Image Resolution: 1.1 in.
- Processing Method: Correlation Algorithm
- Number of Samples: 5

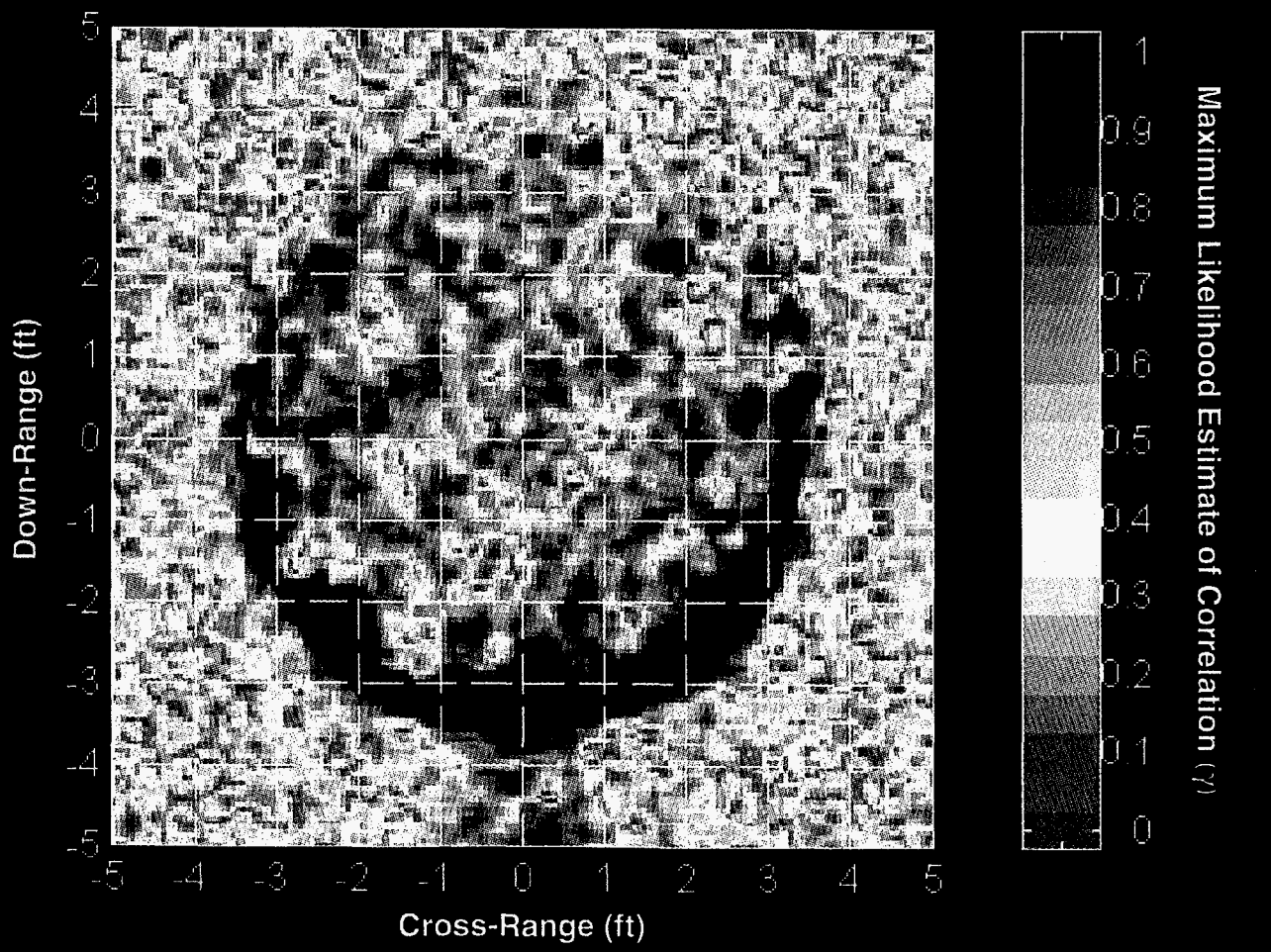

Figure A-10

Tire Tracks

--Wet (t=24 hrs)

(Large Dusty Gravel)

Azimuth Rotation

- File: WT4H
- Chirp BW: 8 GHz
- Center Freq.: 12 GHz
- Pol.:HH
- X Weighting: Hamming
- Y Weighting: Hamming
- Image Resolution: 1.1 in.
- Processing Method: Correlation Algorithm
- Number of Samples: 5

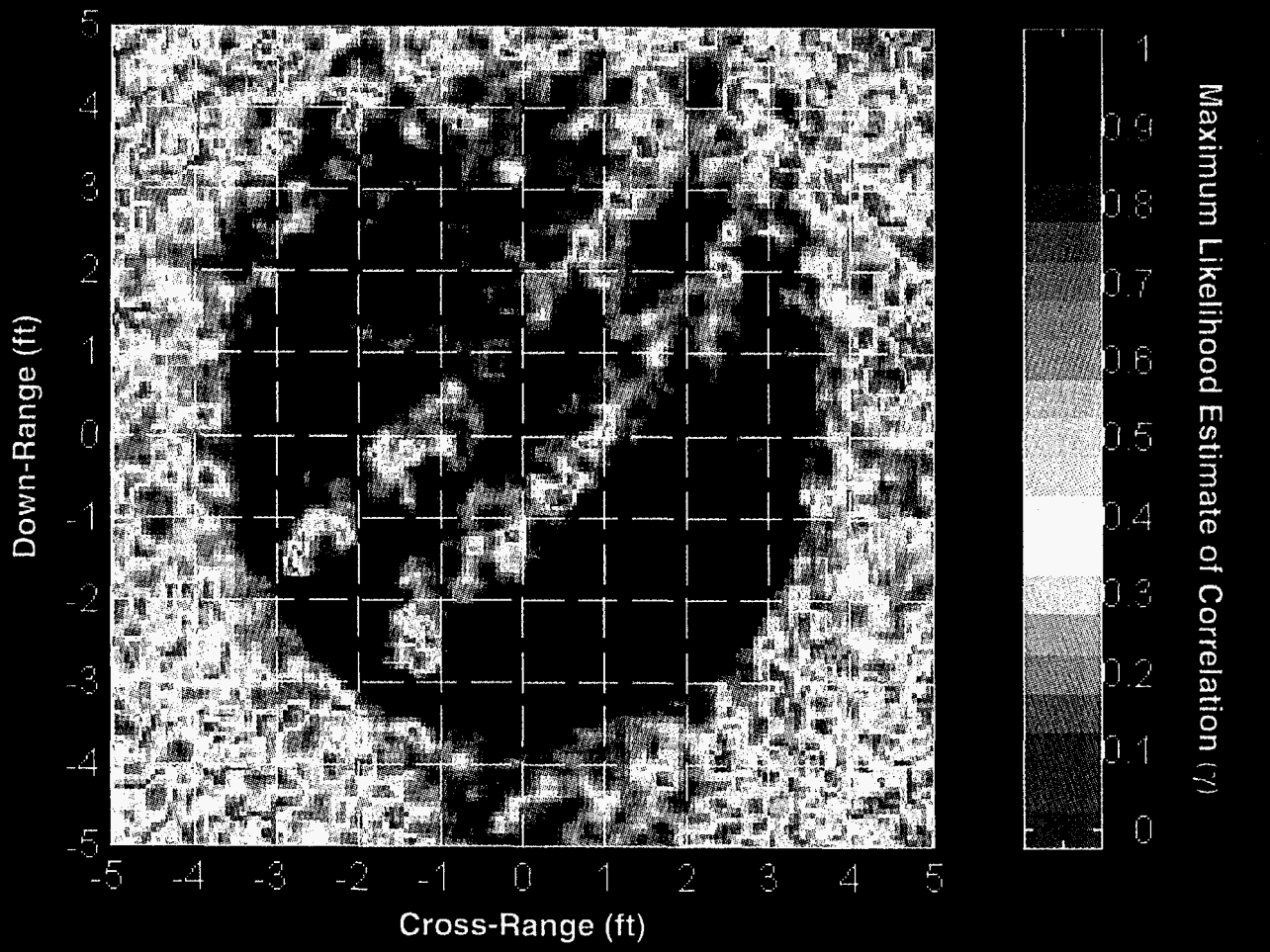

Figure A-11

Tire Tracks

--Wet (t=46 hrs)

(Large Dusty Gravel)

Azimuth Rotation

- File: WT6H
- Chirp BW: 8 GHz
- Center Freq.: 12 GHz
- Pol.:HH
- X Weighting: Hamming
- Y Weighting: Hamming
- Image Resolution: 1.1 in.
- Processing Method: Correlation Algorithm
- Number of Samples: 5

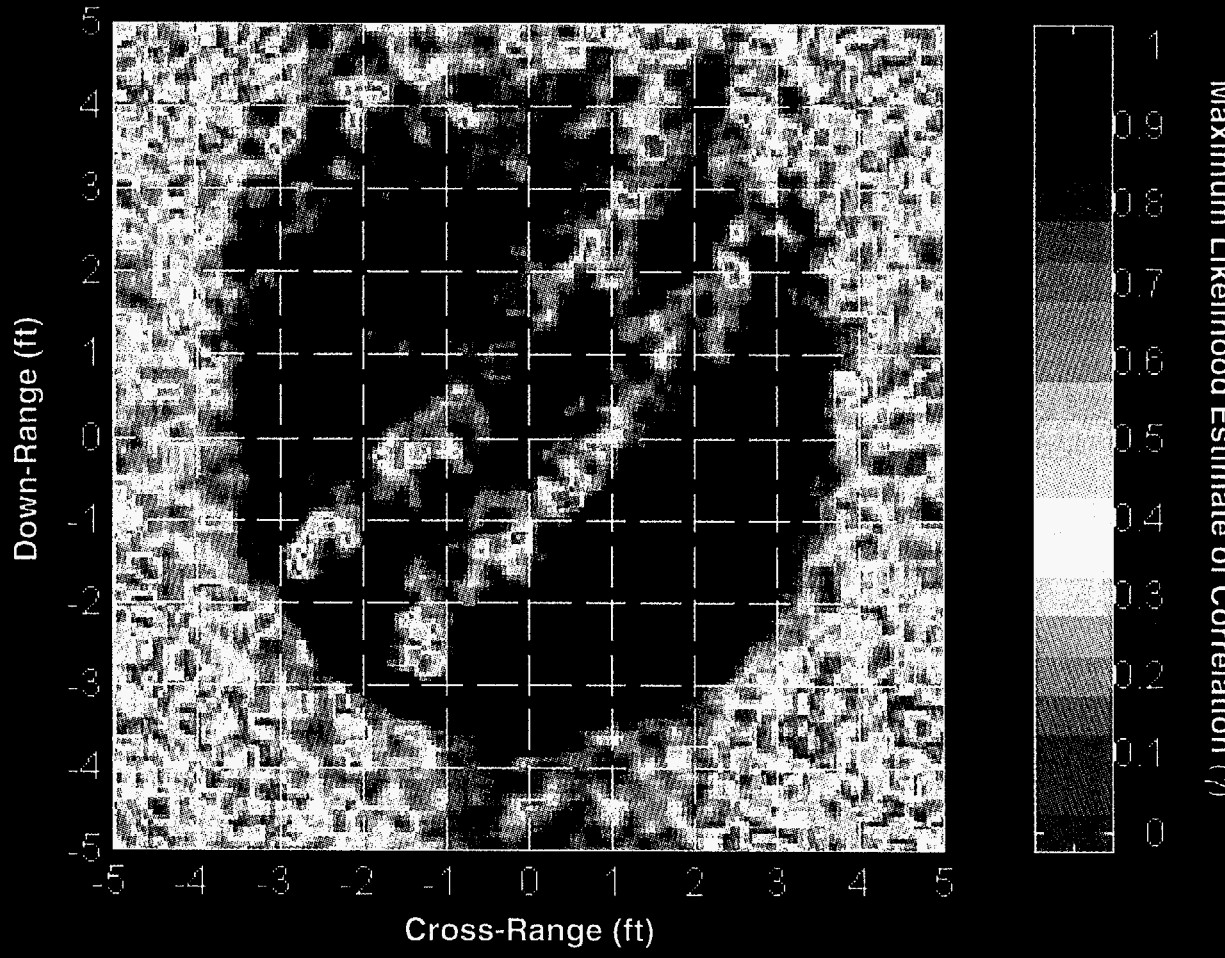

Figure A-12

Tire Tracks

--Wet (t=77 hrs)

(Large Dusty Gravel)

Azimuth Rotation

- File: WT9H
- Chirp BW: 8 GHz
- Center Freq.: 12 GHz
- Pol.:HH
- X Weighting: Hamming
- Y Weighting: Hamming
- Image Resolution: 1.1 in.
- Processing Method: Correlation Algorithm
- Number of Samples: 5

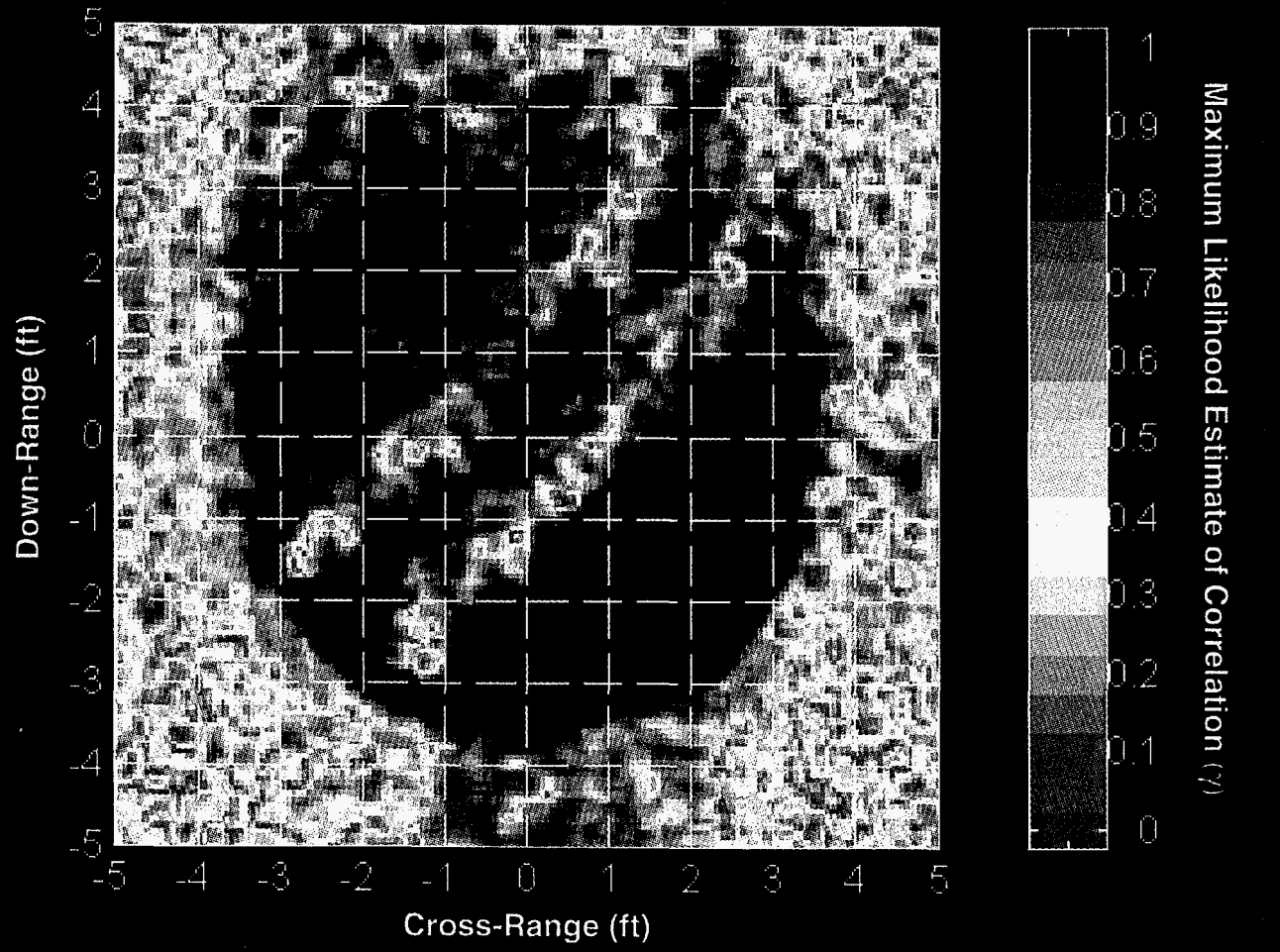

Figure A-13

Tire Tracks

(Large Rinsed Gravel)

Azimuth Rotation

- File: WTAH
- Chirp BW: 8 GHz
- Center Freq.: 12 GHz
- Pol.:HH
- X Weighting: Hamming
- Y Weighting: Hamming
- Image Resolution: 1.1 in.
- Processing Method: Correlation Algorithm
- Number of Samples: 5

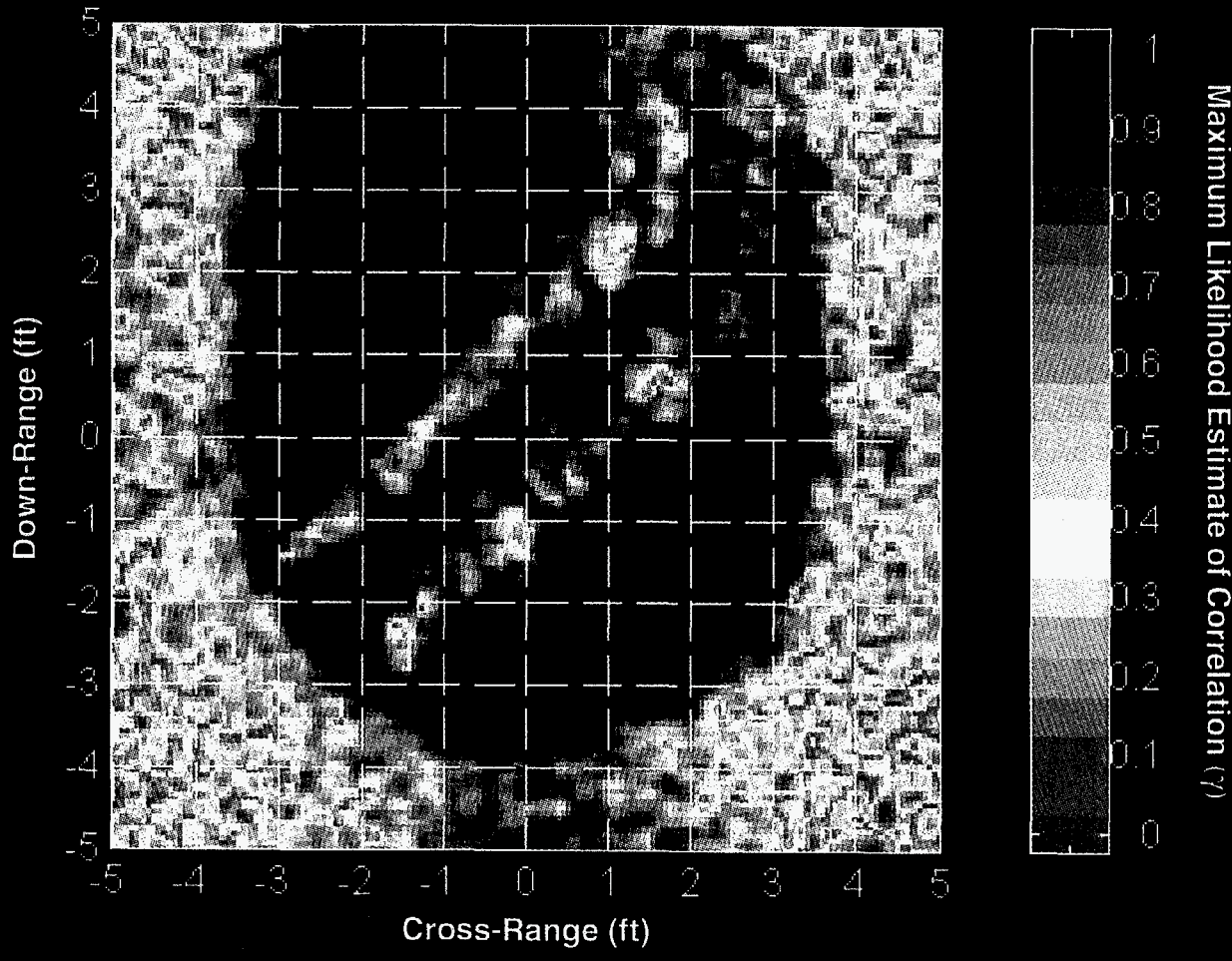

Figure A-14

Tire Tracks

--Wet (t=0 hrs)

(Large Rinsed Gravel)

Azimuth Rotation

- File: WTBH
- Chirp BW: 8 GHz
- Center Freq.: 12 GHz
- Pol.:HH
- X Weighting: Hamming
- Y Weighting: Hamming
- Image Resolution: 1.1 in.
- Processing Method: Correlation Algorithm
- Number of Samples: 5

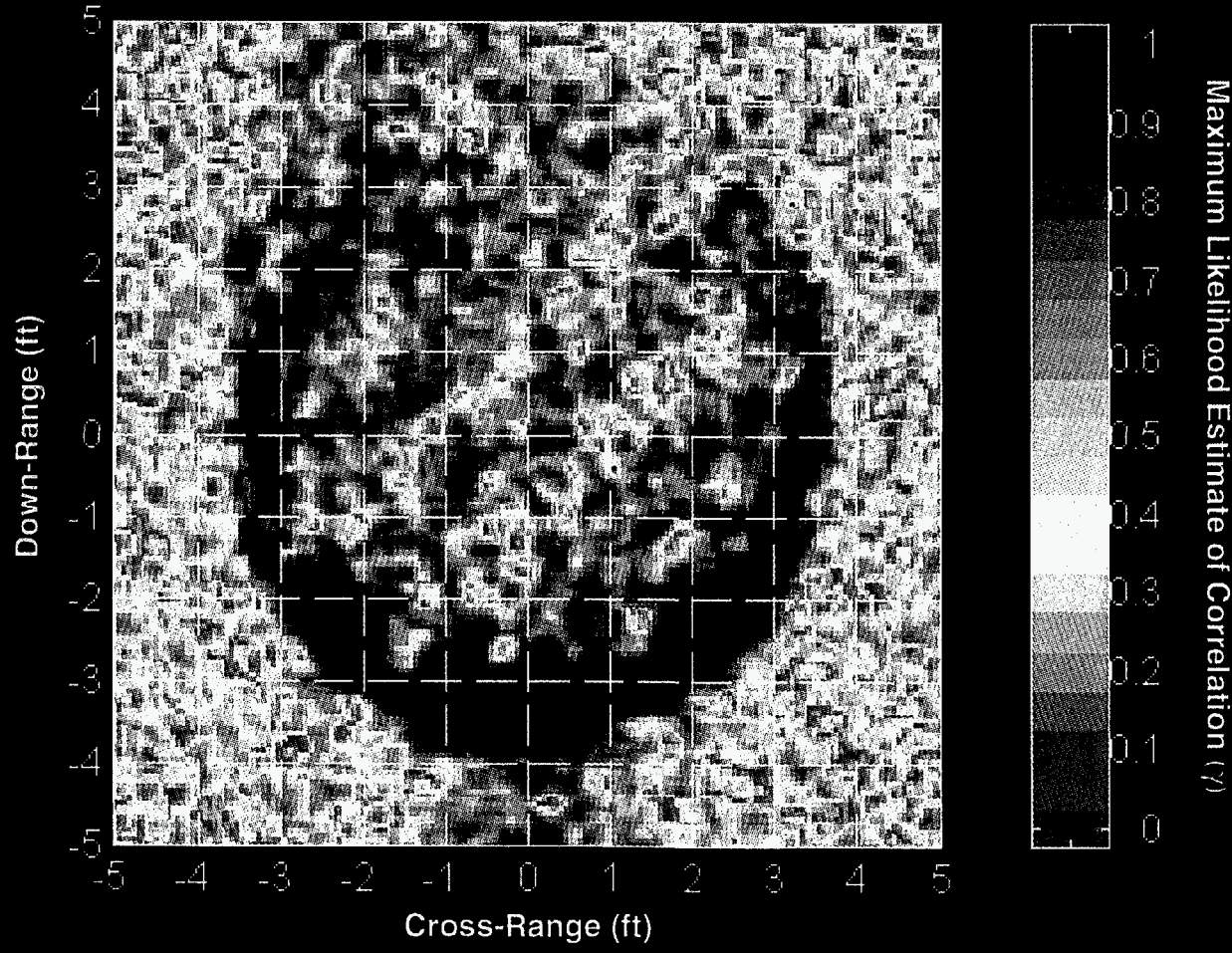

Figure A-15

Tire Tracks

--Wet (t=24 hrs)

(Large Rinsed Gravel)

Azimuth Rotation

- File: WTDH
- Chirp BW: 8 GHz
- Center Freq.: 12 GHz
- Pol.:HH
- X Weighting: Hamming
- Y Weighting: Hamming
- Image Resolution: 1.1 in.
- Processing Method: Correlation Algorithm
- Number of Samples: 5

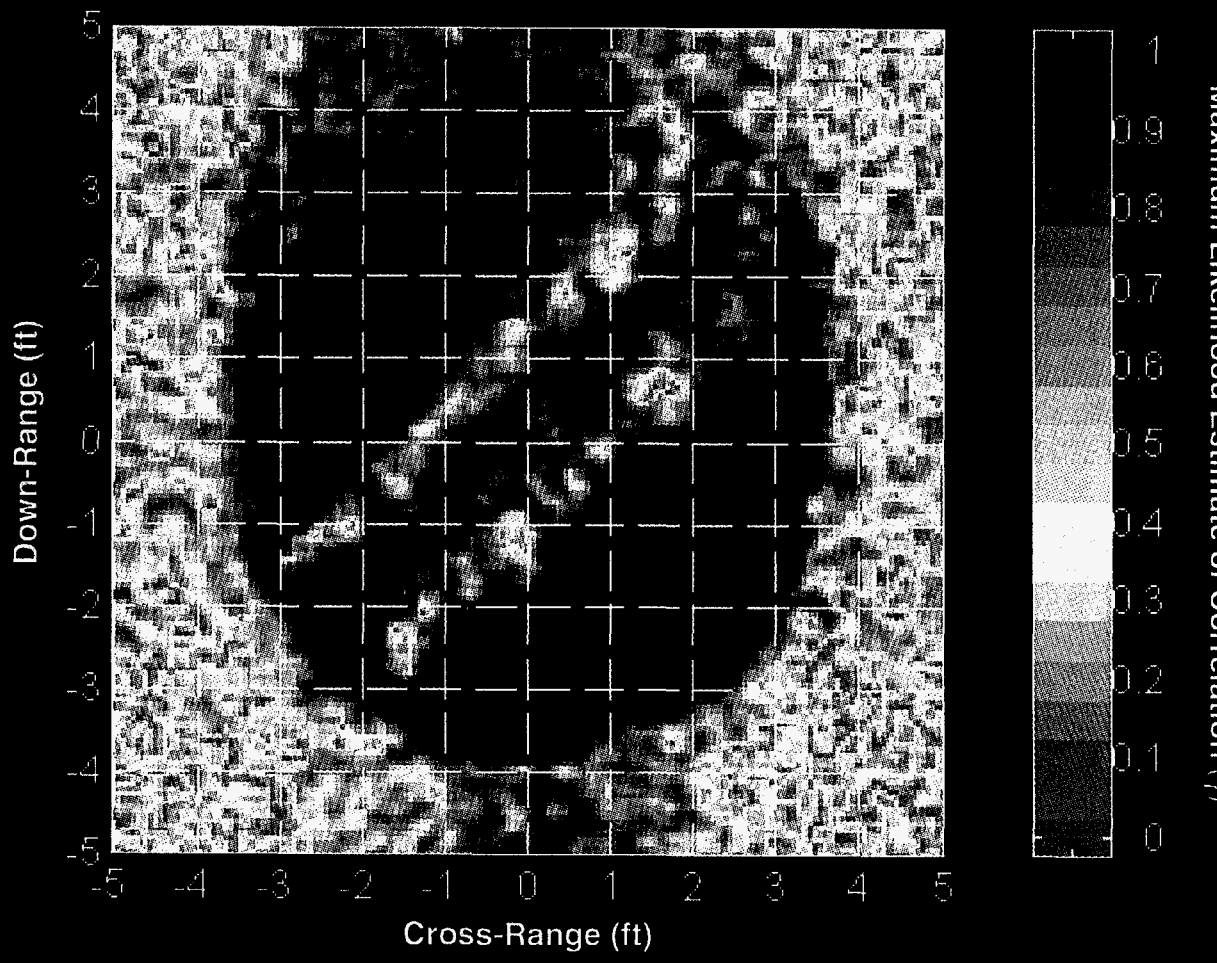

Figure A-16

Tire Tracks

--Wet (t=43 hrs)

(Large Rinsed Gravel)

Azimuth Rotation

- File: WTGH
- Chirp BW: 8 GHz
- Center Freq.: 12 GHz
- Pol.:HH
- X Weighting: Hamming
- Y Weighting: Hamming
- Image Resolution: 1.1 in.
- Processing Method: Correlation Algorithm
- Number of Samples: 5

Figure A-17

Tire Tracks

--Wet (t=66 hrs)

(Large Rinsed Gravel)

Azimuth Rotation

- File: WTIH
- Chirp BW: 8 GHz
- Center Freq.: 12 GHz
- Pol.:HH
- X Weighting: Hamming
- Y Weighting: Hamming
- Image Resolution: 1.1 in.
- Processing Method: Correlation Algorithm
- Number of Samples: 5

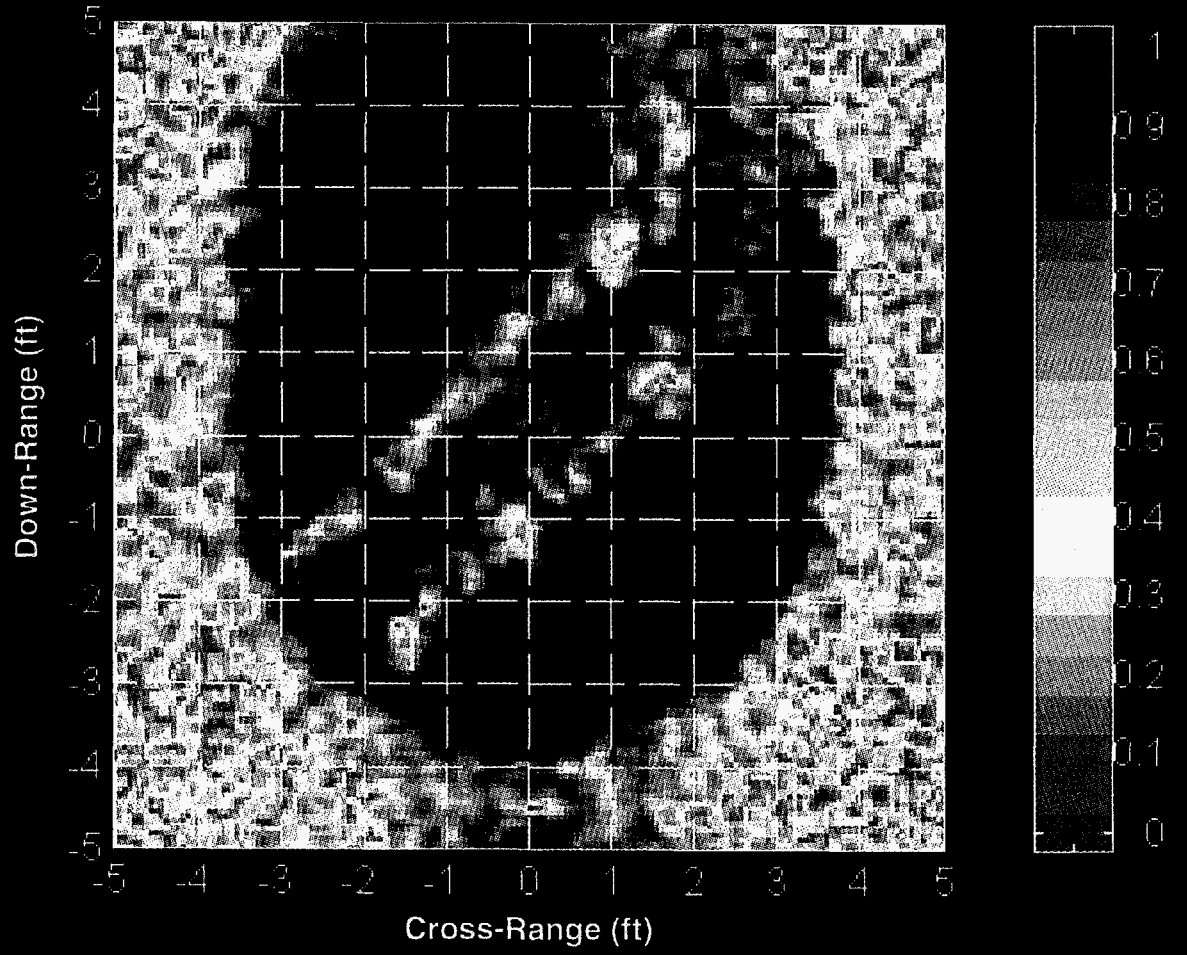

Figure A-18

APPENDIX B

Coherent Change Detection Images of Masonry Sand

Intentionally Left Blank

Masonry Sand in Sample Holder

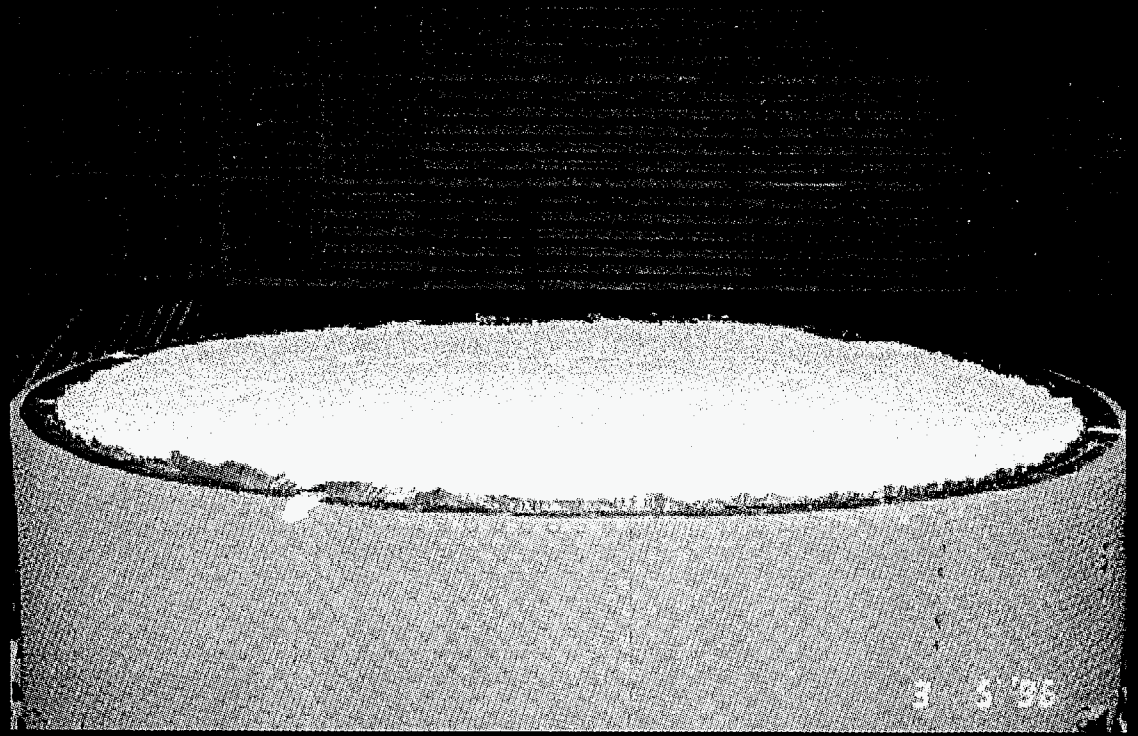

Figure B-1

2-D ISAR Image of Sand (Null Set)

Azimuth Rotation

- File: WK1H
- Chirp BW: 8 GHz
- Center Freq.: 12 GHz
- Pol.:HH
- X Weighting: Hamming
- Y Weighting: Hamming
- Image Resolution: 1.1 in.
- Processing Method: None

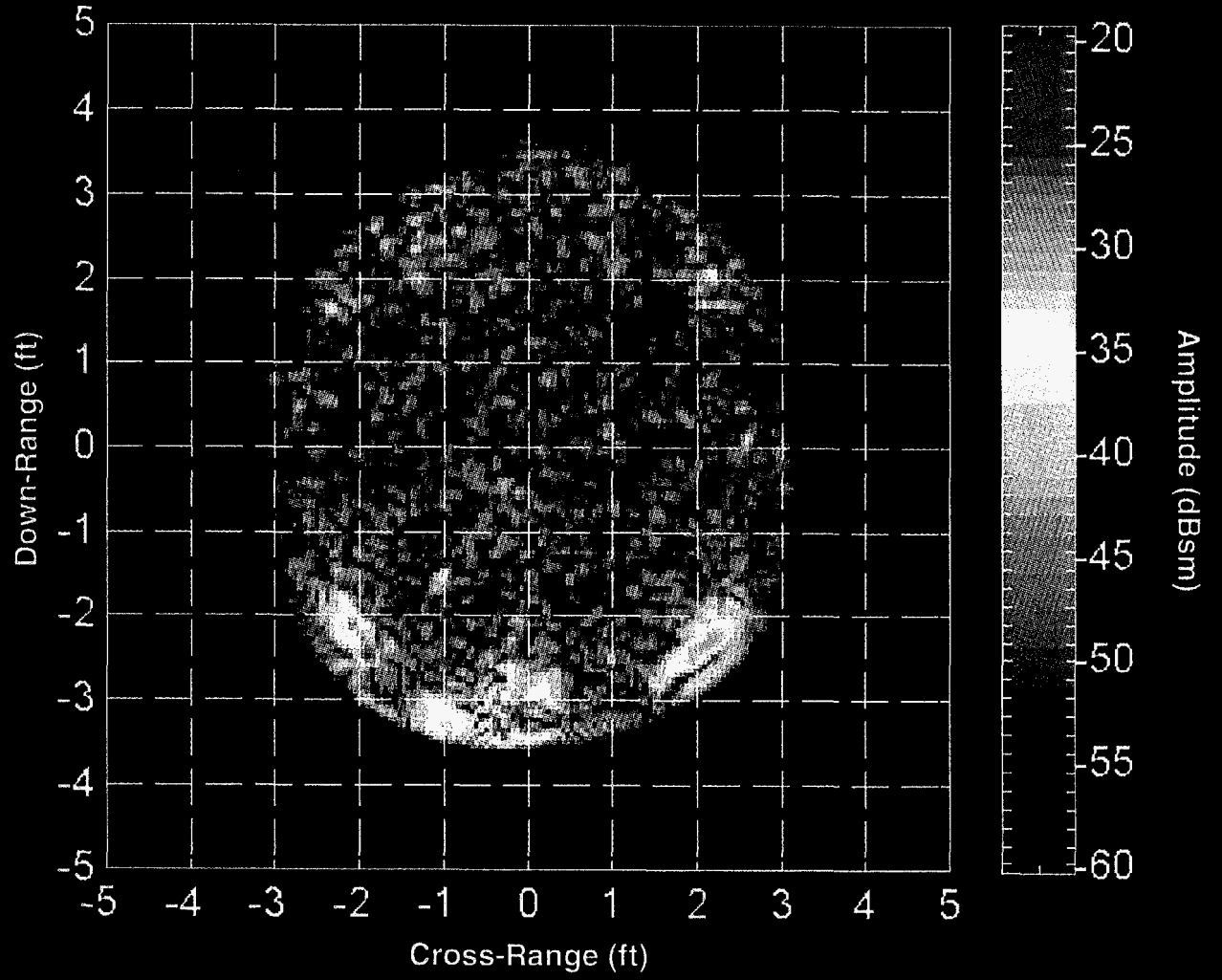

Figure B-2

Retraced Footsteps

(Sand)

Azimuth Rotation

- File: WK1H
- Chirp BW: 8 GHz
- Center Freq.: 12 GHz
- Pol.:HH
- X Weighting: Hamming
- Y Weighting: Hamming
- Image Resolution: 1.1 in.
- Processing Method: Correlation Algorithm
- Number of Samples: 5

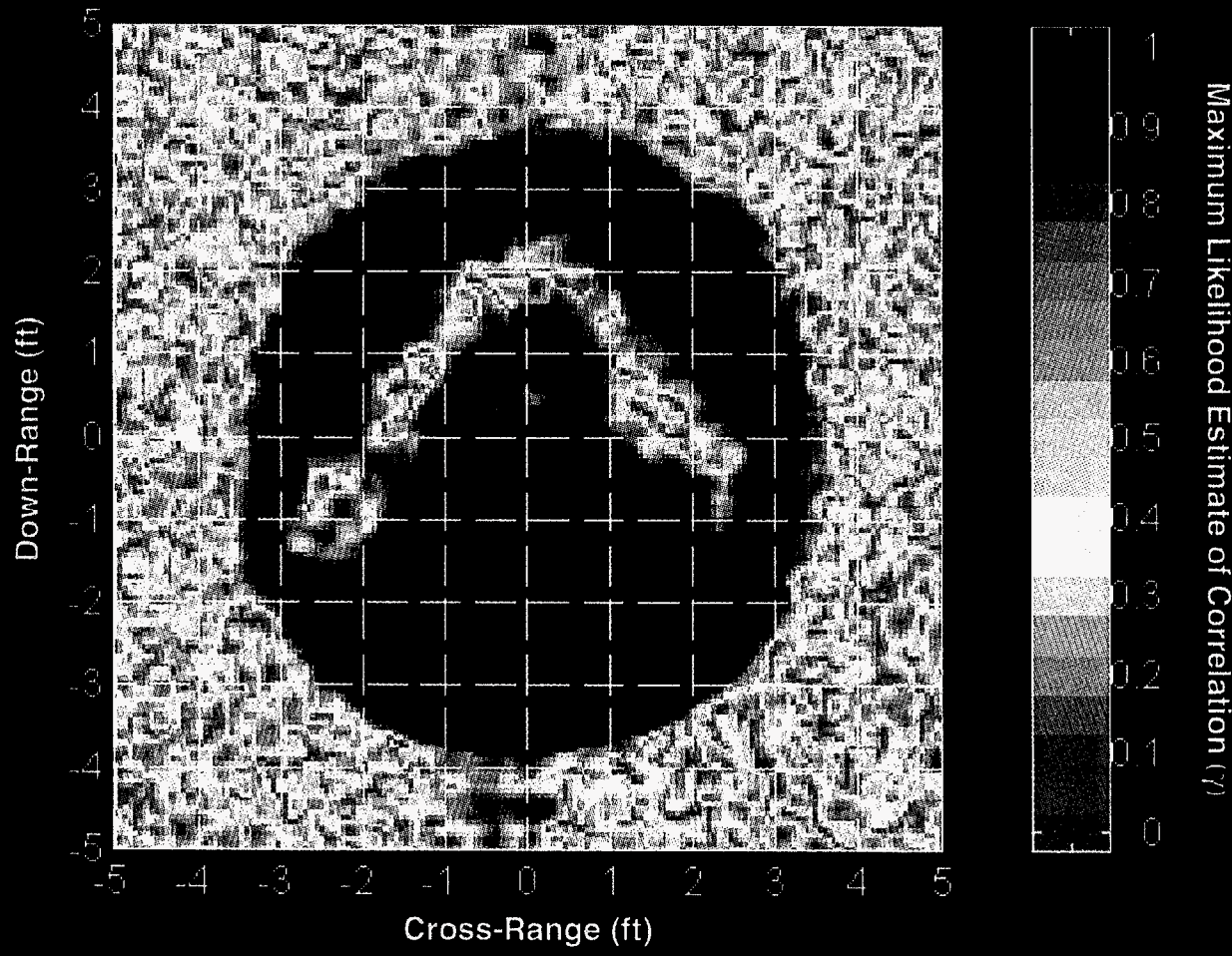

Figure B-3

Discrete Footsteps

(Sand)

Azimuth Rotation

- File: WK2H
- Chirp BW: 8 GHz
- Center Freq.: 12 GHz
- Pol.:HH
- X Weighting: Hamming
- Y Weighting: Hamming
- Image Resolution: 1.1 in.
- Processing Method: Correlation Algorithm
- Number of Samples: 5

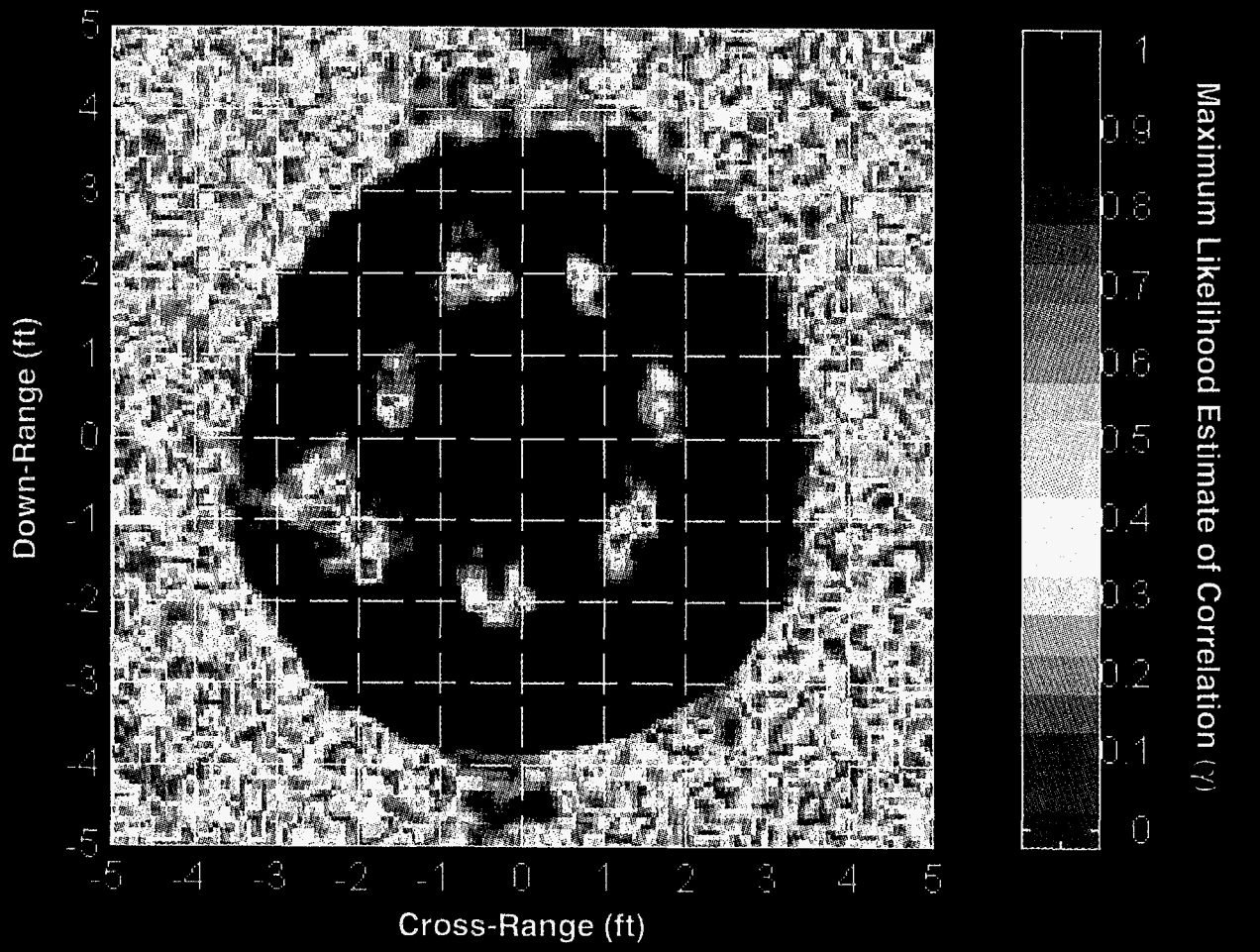

Figure B-4

Light Raking
(Sand)

Azimuth Rotation

- File: R1H
- Chirp BW: 8 GHz
- Center Freq.: 12 GHz
- Pol.:HH
- X Weighting: Hamming
- Y Weighting: Hamming
- Image Resolution: 1.1 in.
- Processing Method: Correlation Algorithm
- Number of Samples: 5

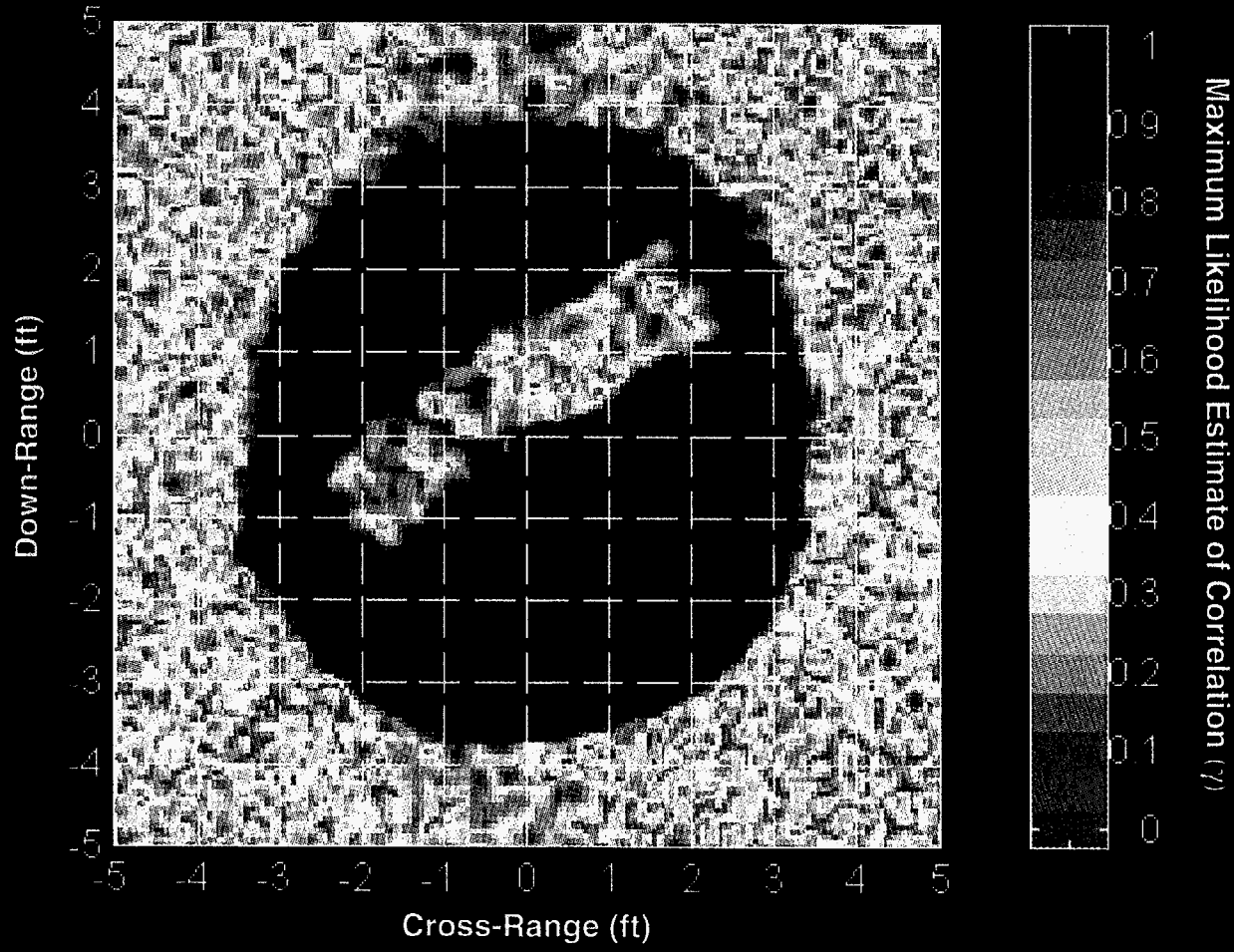

Figure B-5

Medium Raking
(Sand)

Azimuth Rotation

- File: R2H
- Chirp BW: 8 GHz
- Center Freq.: 12 GHz
- Pol.:HH
- X Weighting: Hamming
- Y Weighting: Hamming
- Image Resolution: 1.1 in.
- Processing Method: Correlation Algorithm
- Number of Samples: 5

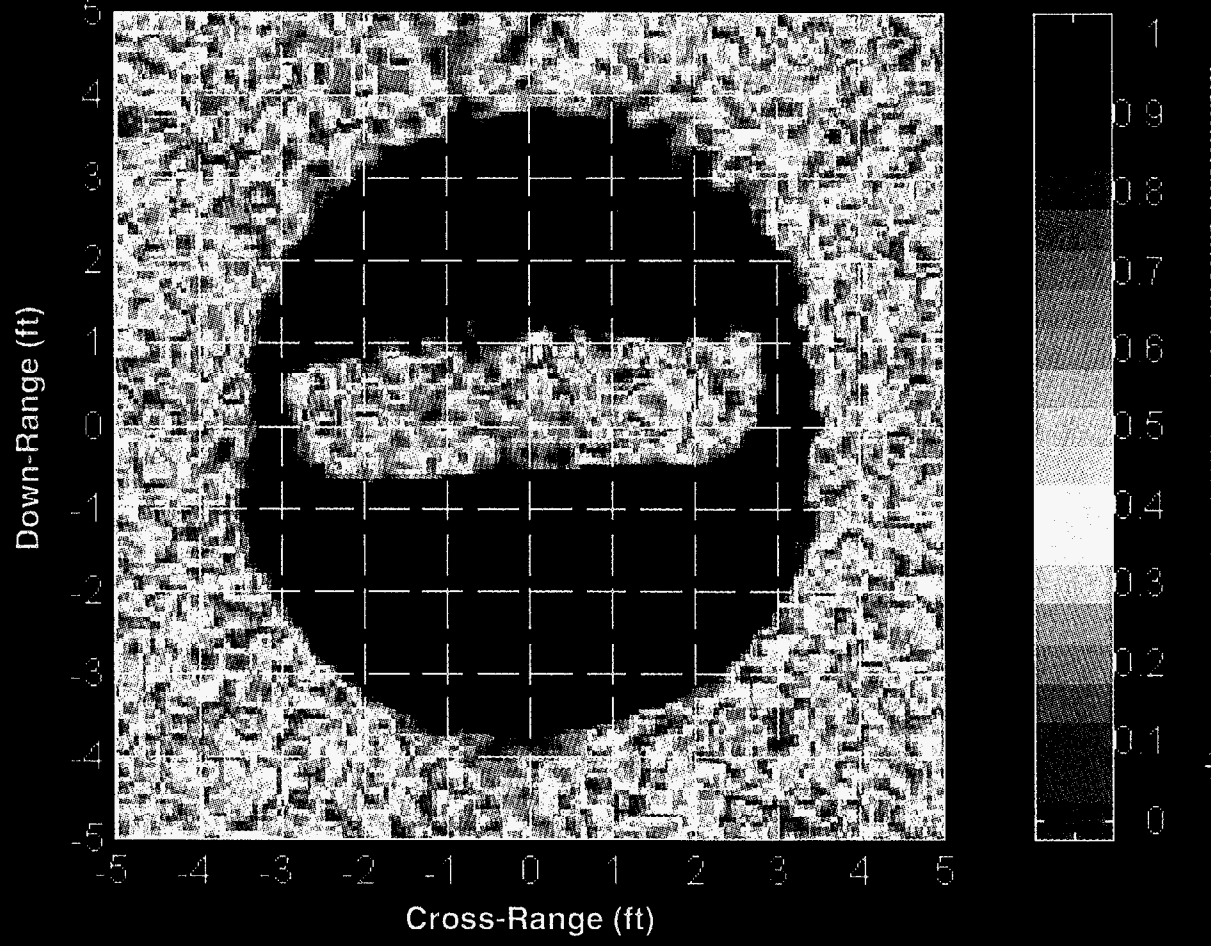

Figure B-6

Heavy Raking
(Sand)

Azimuth Rotation

- File: R3H
- Chirp BW: 8 GHz
- Center Freq.: 12 GHz
- Pol.:HH
- X Weighting: Hamming
- Y Weighting: Hamming
- Image Resolution: 1.1 in.
- Processing Method: Correlation Algorithm
- Number of Samples: 5

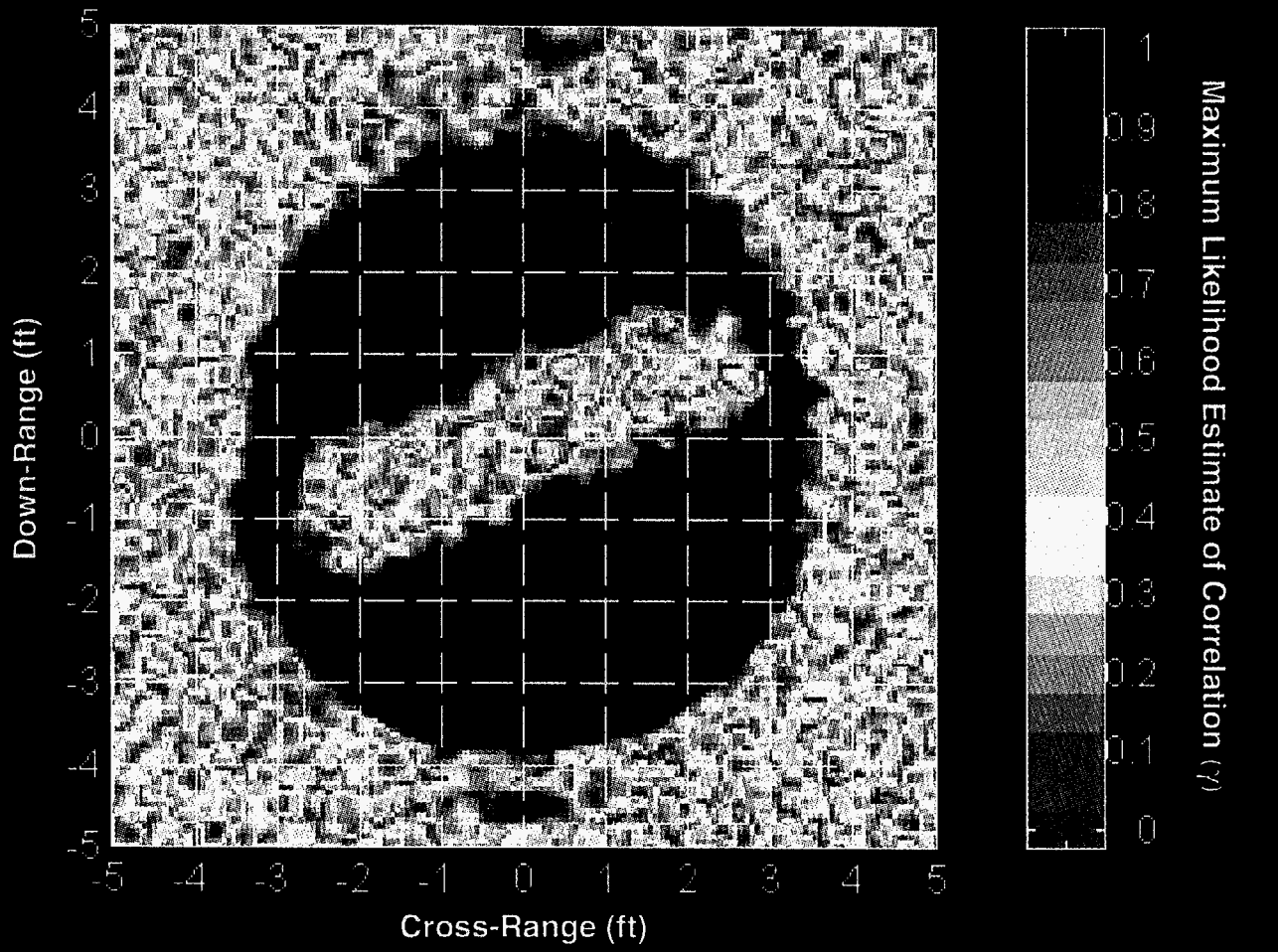

Figure B-7

Incremental Sand Removal

Azimuth Rotation

- File: REM5H
- Chirp BW: 8 GHz
- Center Freq.: 12 GHz
- Pol.:HH
- X Weighting: Hamming
- Y Weighting: Hamming
- Image Resolution: 1.1 in.
- Processing Method: Correlation Algorithm
- Number of Samples: 5

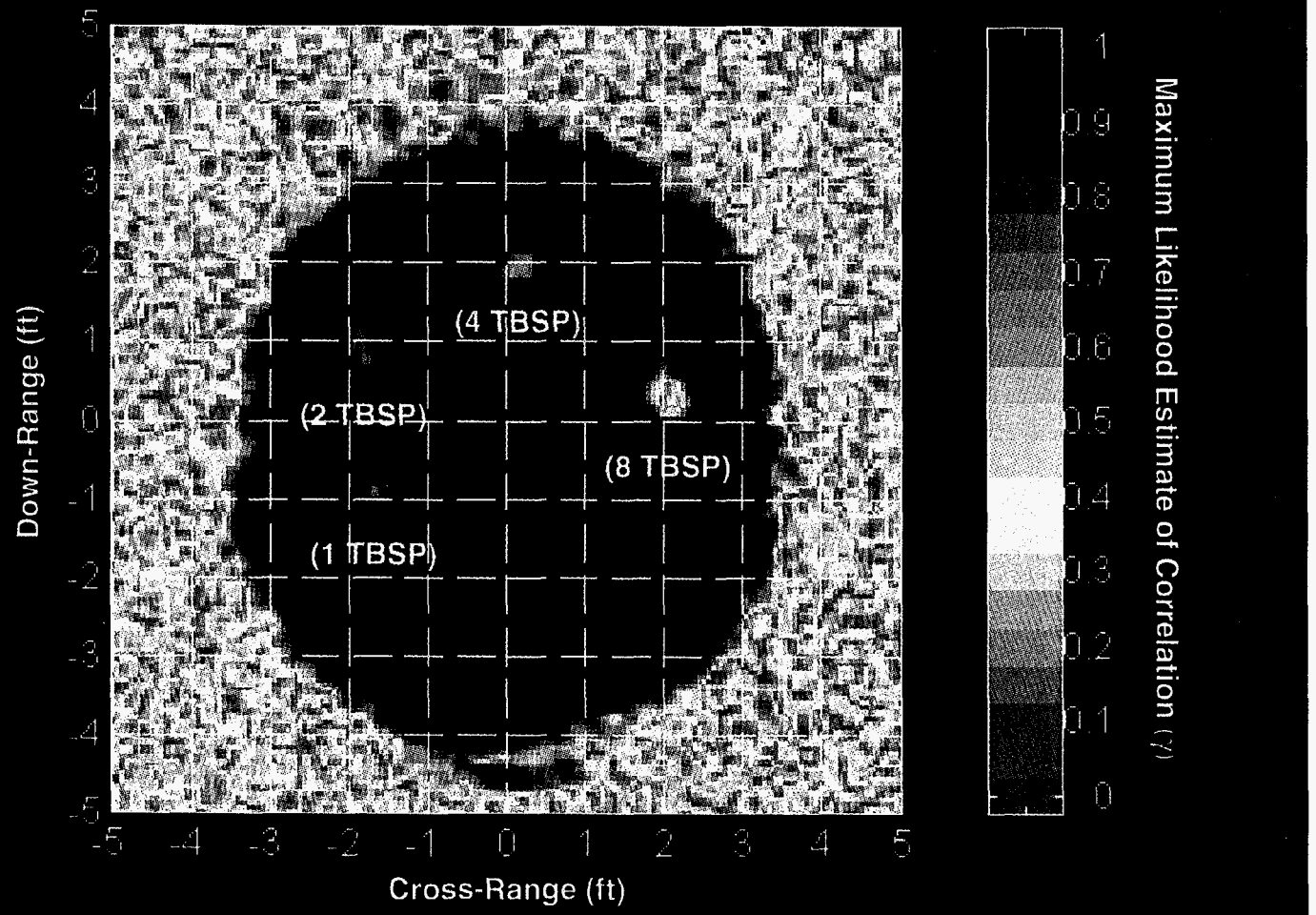

Figure B-8

Tire Tracks

(Sand)

Azimuth Rotation

- File: M1H
- Chirp BW: 8 GHz
- Center Freq.: 12 GHz
- Pol.:HH
- X Weighting: Hamming
- Y Weighting: Hamming
- Image Resolution: 1.1 in.
- Processing Method: Correlation Algorithm
- Number of Samples: 5

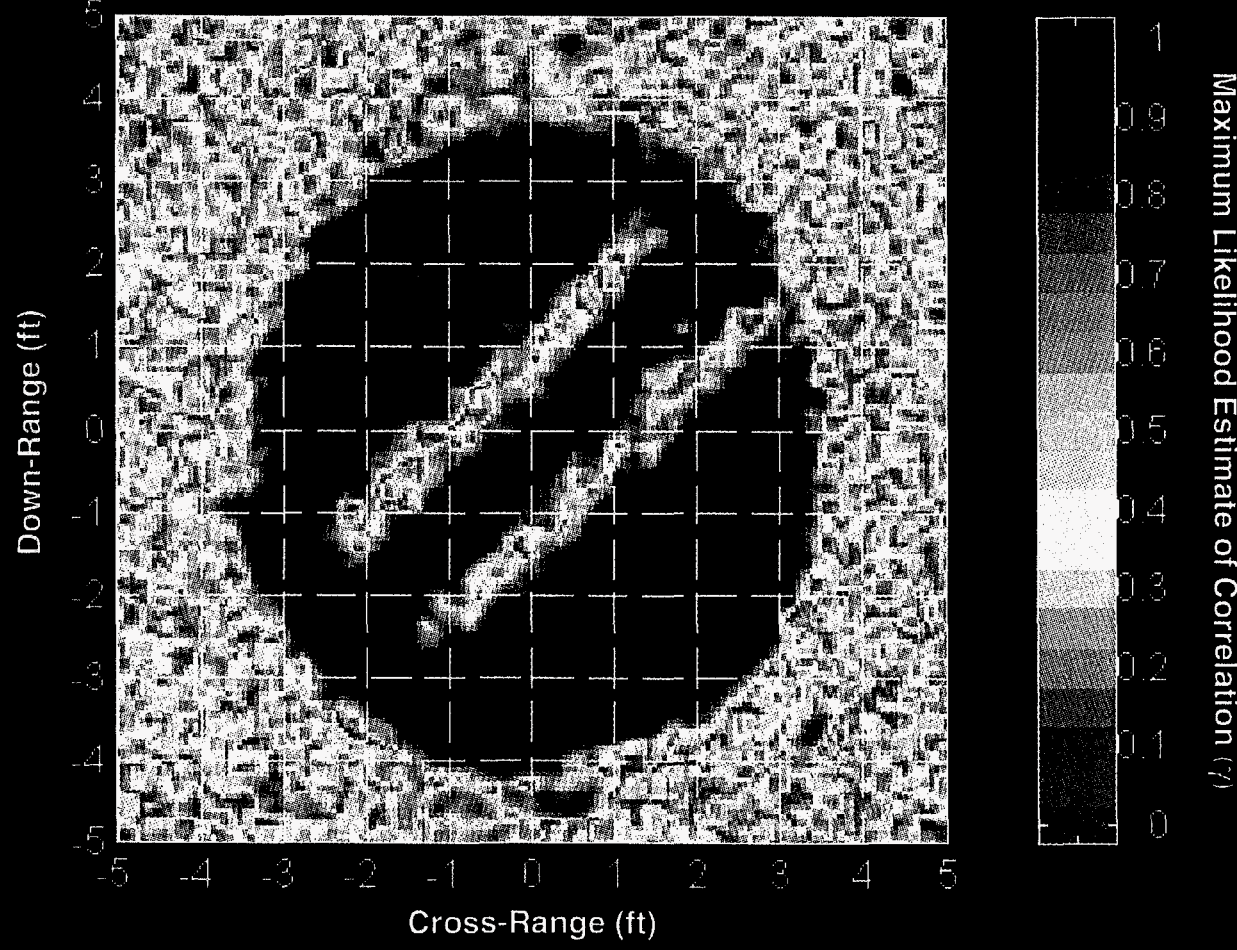

Figure B-9

Tire Tracks

--Wet (t=0 hrs)

(Sand)

Azimuth Rotation

- File: M2H
- Chirp BW: 8 GHz
- Center Freq.: 12 GHz
- Pol.:HH
- X Weighting: Hamming
- Y Weighting: Hamming
- Image Resolution: 1.1 in.
- Processing Method: Correlation Algorithm
- Number of Samples: 5

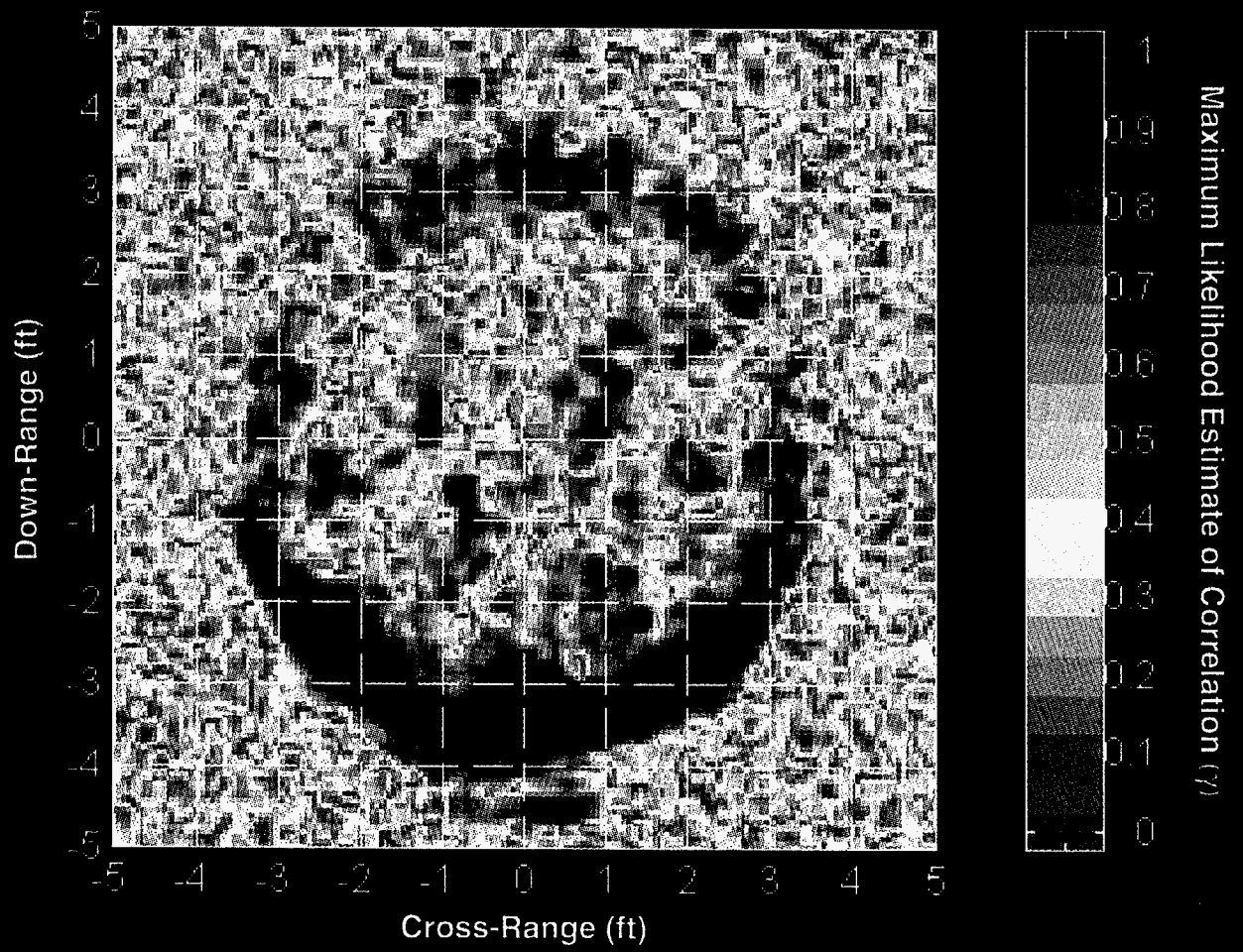

Figure B-10

Tire Tracks

--Wet (t=20 hrs)

(Sand)

Azimuth Rotation

- File: M4H
- Chirp BW: 8 GHz
- Center Freq.: 12 GHz
- Pol.:HH
- X Weighting: Hamming
- Y Weighting: Hamming
- Image Resolution: 1.1 in.
- Processing Method: Correlation Algorithm
- Number of Samples: 5

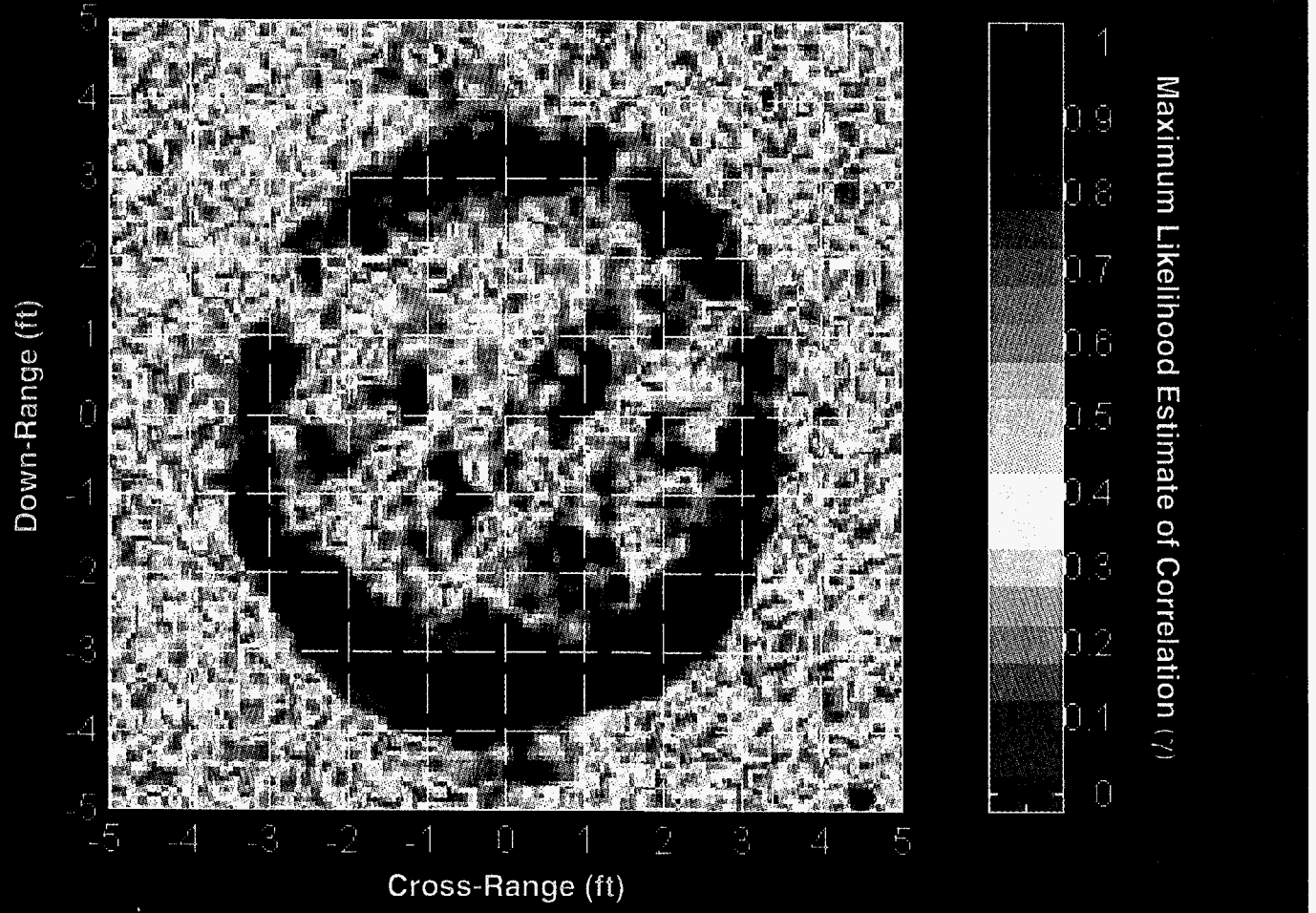

Figure B-11

Tire Tracks

--Wet (t=48 hrs)

(Sand)

Azimuth Rotation

- File: M6H
- Chirp BW: 8 GHz
- Center Freq.: 12 GHz
- Pol.:HH
- X Weighting: Hamming
- Y Weighting: Hamming
- Image Resolution: 1.1 in.
- Processing Method: Correlation Algorithm
- Number of Samples: 5

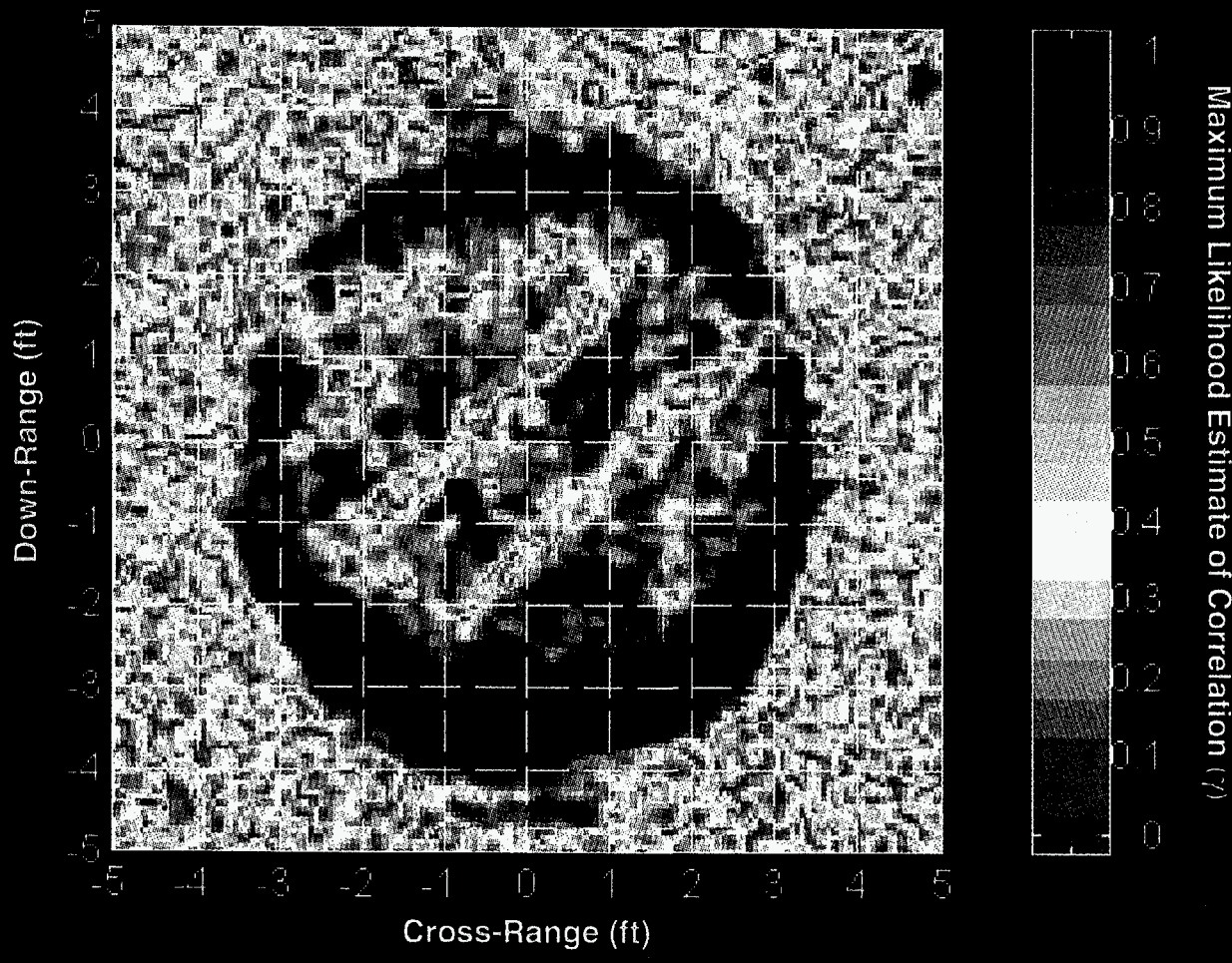

Figure B-12

Tire Tracks

--Wet (t=71 hrs)

(Sand)

Azimuth Rotation

- File: M9H
- Chirp BW: 8 GHz
- Center Freq.: 12 GHz
- Pol.:HH
- X Weighting: Hamming
- Y Weighting: Hamming
- Image Resolution: 1.1 in.
- Processing Method: Correlation Algorithm
- Number of Samples: 5

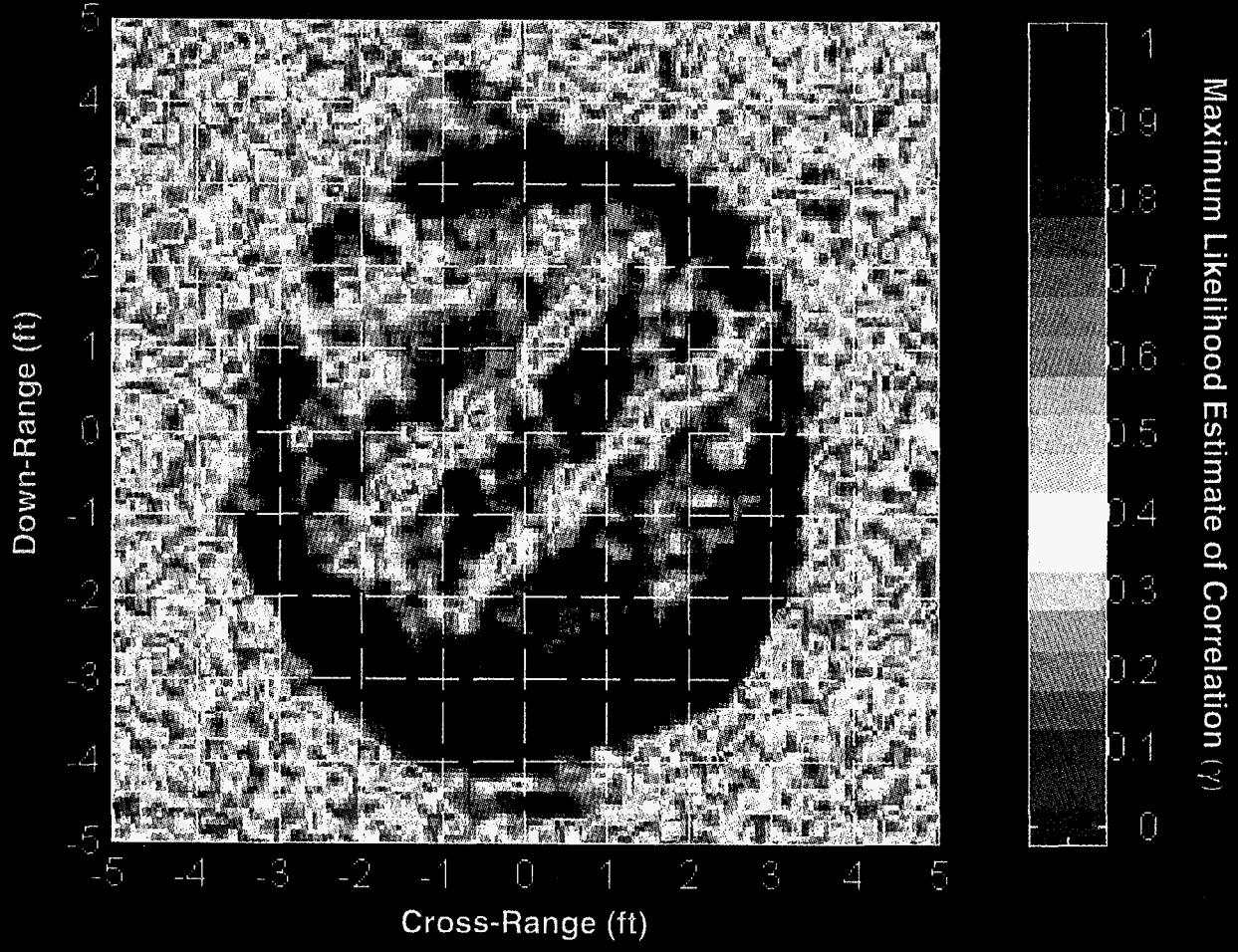

Figure B-13

APPENDIX C

ISAR Measurement Simulation

A numerical simulation has been performed in order to gain a level of understanding as to how well the correlation functions predicted by (11) can be expected to fit data in which the processed images have resolution cell sizes on the order of a wavelength, and which encompass a relatively small number of discrete scatterers. This was accomplished by simulating an ISAR measurement of nine discrete point scatterers located within a resolution cell and spaced as was shown in Figure 3(b). The theory and methodology of this simulation exercise follow below.

The measured complex signal resulting from the electromagnetic energy backscattered from n point scatterers to a radar can be expressed as [12]

$$A = \sum_{i=1}^{n} a_i e^{j\phi_i} , \tag{C-1}$$

where a_i is the backscattered amplitude of the i^{th} scatterer, and ϕ_i is the phase accumulated along the two-way path from the radar to the scatterer, and is written as

$$\phi_i = 2kR_i = \frac{4\pi}{\lambda} R_i \ . \tag{C-2}$$

At the compact range measurement facility, inverse synthetic aperture radar techniques are used to process the measured complex backscattered data in order to facilitate distinguishability of target features that are spatially separated. Inverse synthetic aperture radar (ISAR) is a technique that is used to produce high resolution images of targets in two dimensions. ISAR utilizes a frequency varying waveform (swept frequency "chirped" waveform, FMCW, stepped frequency waveform, etc.) to achieve high resolution in the down-range dimension of the image, and the rotation motion of a target past a stationary radar to achieve high cross-range resolution [28]. It is well known that data equivalent to that obtained by a circular spotlight-mode SAR can be achieved through proper ISAR processing [2]. The basis for achieving high resolution with an ISAR setup is explained below.

The highest range resolution that can be achieved by a radar transmitting a waveform having a rectangular bandwidth B is given by [28]

$$\Delta r = \frac{c}{2B} , \tag{C-3}$$

where c = velocity of propagation of the radar signal (speed of light). A stepped-frequency waveform employing n frequency steps of size Δf_s can therefore achieve a down-range resolution of

$$\Delta r_d = \frac{c}{2n\Delta f_s} \,. \tag{C-4}$$

The ISAR cross-range resolution is dependent upon the doppler frequency shift associated with a target that is rotating relative to the radar line-of-sight. The derivation of cross-range resolution given here parallels that given in [17] and [28]. It may be recalled that the doppler frequency shift for an object having a radial velocity of v_r relative to a stationary radar is given by [17], [28]

$$f_{doppler} = \frac{2v_r}{\lambda}, \tag{C-5}$$

where λ is the wavelength of the transmitted signal in the propagation medium.

Consider the case of a single point scatterer located at a distance r from the center of a rotating platform as shown in Figure C1, and assume that the radar line-of-sight is in the rotational plane of the scatterer and that the radar and platform have no translational motion relative to one another. The platform is rotating at a constant angular rate of ω radians per second on an axis perpendicular to the radar line of sight (that is, the axis is into the page in Figure C1).

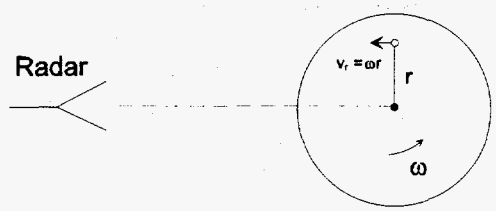

Figure C1. Single point scatterer in the far-field of an illuminating radar, located at a distance r from the center of a rotating platform.

The instantaneous radial velocity of the point scatterer toward the radar is then given by

$$v_r = \omega r, \tag{C-6}$$

and the doppler frequency shift associated with the point scatterer is therefore given as

$$f_{doppler} = \frac{2\omega r}{\lambda} \,. \tag{C-7}$$

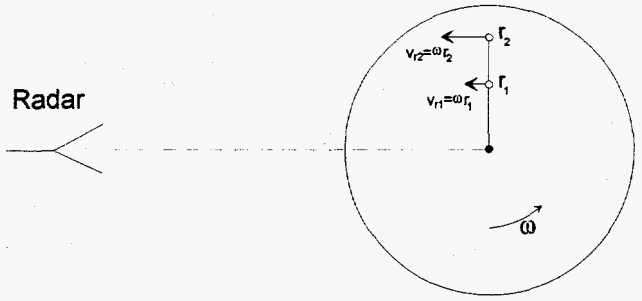

Figure C2. Two point scatterers located within the same down-range resolution cell of a radar, located at distances r_1 and r_2 from the center of a rotating platform.

Consider next the case of two point scatterers located within the same down-range resolution cell, as shown in Figure C2, but having differing radial distances r_1 and r_2 from the center of the rotating platform. With all other assumptions of the operational scenario remaining as described above (radar line-of-sight in rotational plane of point scatterers, no translational motion, etc.), the difference in the doppler frequencies ($\Delta f_d = f_{doppler_2} - f_{doppler_1}$) between the two point scatterers can be written as

$$\Delta f_d = \frac{2\omega}{\lambda}(r_2 - r_1) = \frac{2\omega}{\lambda}\Delta r \,. \tag{C-8}$$

The achievable cross-range resolution in the down-range resolution cell is thus given by

$$\Delta r_c = \frac{\lambda}{2\omega}\Delta f_d \,. \tag{C-9}$$

Realizing that the doppler resolution is inversely proportional to the coherent integration time (t_{int}) of an ISAR measurement [28], such that

$$\Delta f_d \approx \frac{1}{t_{\text{int}}}, \tag{C-10}$$

and that the point scatterers rotate through an angle Φ during the time t_{int}, then the cross-range resolution can finally be written as

$$\Delta r_c = \frac{\lambda}{2\omega t_{\text{int}}} = \frac{\lambda}{2\Phi}. \tag{C-11}$$

Two Fourier transforms are required to obtain a two-dimensional down-range and cross-range ISAR image. This is understood by first noting that the backscattered signal from a target in the frequency domain obtained with a stepped-frequency waveform must be transformed into the time domain in order to obtain a down-range profile. Similarly, for a

sequence of range profiles acquired in order to obtain cross-range resolution of the target, the time-domain data in each range-resolution bin must be transformed into the frequency domain in order to obtain the doppler information for the target [28].

There are of course other considerations which are important when performing or simulating ISAR measurements, such as choosing the radar parameters appropriately to avoid ambiguous sampling of the target backscattered response in range and cross range (which would result in aliased target returns in the final image), etc., but for clarity of discussion, these issues will not be addressed here.

Having reviewed the theory for forming a two-dimensional ISAR image, the methodology for performing a simulation becomes apparent. That is, the discrete scatterers are each assigned an initial range R_{i0} from the radar to their position on the rotating platform along the radar line of sight, as well as a radial distance r_i from the center of the rotating platform to the center of the point scatterer. The vector sum of the backscattered energy from each of the individual scatterers is then computed according to (C-1) at each of n frequencies (the frequency steps being of size Δf_s) in order to achieve down-range resolution in the final image of (C-4). For this simulation, the backscattered amplitude (a_i) for all point scatterers was chosen to be unity. The value of the range parameter to be used in determining the phase of each backscattered signal is given by

$$R_i = R_{i0} + \omega t r_i \ , \tag{C-12}$$

where t is the amount of time that has transpired between the initiation of the measurement and the current radar pulse, with the time step between each pulse being equal to the inverse of the pulse repetition frequency ($\Delta t = 1/PRF$).

From (C-11) it can be seen that the cross-range resolution will be equivalent to the down-range resolution if the angular rate of rotation of the platform is chosen to be

$$\omega = \frac{\lambda}{2\Delta r_d t_{\text{int}}}, \tag{C-13}$$

where the effective integration time (t_{int}) is given by

$$t_{\text{int}} = n \times M \times \frac{1}{PRF}, \tag{C-14}$$

in which n = number of frequency steps and M = number of stepped frequency waveforms processed.

The pertinent parameters that were chosen for this simulation are given in Table C1.

TABLE C1. Simulation Parameters

Parameter	Specified Value
f_0	1.28 GHz
n	64
Δf_s	8.0 MHz
PRF	10.0 kHz
M	64
ω	1.22 rad/s
Δr_d	0.293 m
Δr_c	0.293 m

Intentionally Left Blank

DISTRIBUTION:

1	MS	0509	W. David Williams, 2300
1		0533	W. H. Schaedla, 2343
1		0533	S. E. Allen, 2343
1		0533	B. C. Brock, 2343
1		0533	J. H. Littlejohn, 2343 (Contractor)
8		0533	K. W. Sorensen, 2343
1		0533	D. H. Zittel, 2343
1		0537	R. M. Axline, 2344
1		0537	D. L. Bickel, 2344
1		0537	W. H. Hensley, 2344
1		0529	A. W. Doerry, 2345
1		0529	B. C. Walker, 2345
10		0570	B. F. Johnson, 5900
1		0572	C. V. Jakowatz, 5912
1		9018	Central Technical Files, 8523-2
5		0899	Technical Library, 4414
2		0619	Review and Approval Desk, 12630 For DOE/OSTI